EMPLOYING MODERN STATISTICS TO EXPLORE THE UNIVERSE WITH TYPE IA SUPERNOVAE

by

Anja Weyant

B.S. in Physics, Carnegie Mellon University, 2008

Submitted to the Graduate Faculty of

the Kenneth P. Dietrich School of Arts and Sciences in partial fulfillment

of the requirements for the degree of

Doctor of Philosophy

University of Pittsburgh

2014

UNIVERSITY OF PITTSBURGH

DIETRICH SCHOOL OF ARTS AND SCIENCES

This dissertation was presented

by

Anja Weyant

It was defended on

April 22th 2014

and approved by

William Michael Wood-Vasey, PhD, Assistant Professor

Jeffrey Newman, PhD, Associate Professor

Paul Shepard, PhD, Professor

Larry Wasserman, PhD, Professor

Andrew Zentner, PhD, Associate Professor

Dissertation Director: William Michael Wood-Vasey, PhD, Assistant Professor

EMPLOYING MODERN STATISTICS TO EXPLORE THE UNIVERSE WITH TYPE IA SUPERNOVAE

Anja Weyant, PhD

University of Pittsburgh, 2014

The Large Synoptic Survey Telescope (LSST) anticipates observing hundreds of thousands of well-measured Type Ia supernovae (SNe Ia). These stellar remnant explosions are exceptional in that they have a standardizeable light curve which allows for an accurate measurement of their luminosity. The standard nature of SNe Ia allow us to measure relative distances in the Universe with better than 6% precision in distance. With distance estimates in hand to large sets of galaxies through Type Ia Supernova (SN Ia) measurements, we can measure the expansion history of the Universe or create flow models of how galaxies (matter) near the Milky Way are moving.

In this new regime of large datasets, weaknesses and limitations of the current techniques for estimating cosmological parameters and modeling local flows are becoming apparent. As statistical errors are reduced systematic uncertainties ranging from calibration to survey design and cadence to host galaxy contamination are dominating the error budget and limiting our ability to make improvements on cosmological measurements. Similarly, recent comparisons of flow models reveal systematic inconsistencies between different approaches.

For my dissertation I have employed modern statistical methods to improve flow models in the local Universe by accounting for the non-uniform distribution of data across the sky and demonstrated how Approximate Bayesian Computation can tackle complicated likelihood functions in supernova cosmology. I also present the first results of a new near-infrared SN Ia survey called "SweetSpot" whose focus is on improving our ability to standardize the total luminosity of SNe Ia.

TABLE OF CONTENTS

LIST OF TABLES

LIST OF FIGURES

PREFACE

I would like to express my sincere gratitude to my supervisor, Prof. W. Michael Wood-Vasey, for supporting my Ph.D study. I am grateful for the freedom that my supervisor gave me in pursuing this research. I greatly appreciate his knowledge and guidance and I would like to thank him for his motivation, patience, and especially, his time. Additionally, I would like to thank my thesis committee: Andrew Zentner, Jeffrey Newman, Larry Wasserman and Paul Shepard, for their friendly advice and encouragement.

I am deeply grateful to David Turnshek and Sandhya Rao for the REU opportunity that led me to the University of Pittsburgh. I wish to thank them for their friendship and kindness during my undergraduate and graduate careers. I also thank Richard Holman for his advice and friendship during my entire academic career and for often giving me perspective.

To the entire Department of Physics and Astronomy, especially the staff, I am thankful for the support that has allowed me to produce and complete my thesis. I would especially like to thank Leyla Hirshfeld who has expedited my graduate student existence. I am also grateful to the staff, scientists, and observing support at KPNO and thank them for providing me with a wonderful observing experience.

A special thanks is due to Ken Vroman and Robert McClure. Without their enthusiasm in high school it is unlikely that I would have pursued physics and astronomy.

Finally, I would like to thank my parents, Tina and Jeffrey Weyant and my siblings: Jens, Grace, Zachary, Rachel, Samantha, and Lars Weyant, for their unconditional love and support. I thank my grandparents, Werner and Ute Philipp, for providing a retreat from academics. I am grateful to my son, Leif Neill, for keeping me on my toes. Most importantly, I wish to thank my best friend and husband, Duff Neill, whose love and encouragement has been critical to the completion of this work. To my entire family, I dedicate this thesis.

1.0 INTRODUCTION

Only 5% of all the mass and energy in the Universe is in the form of normal matter which can be explained by basic physics. "Dark matter," which makes up 25% of the matter-energy content, is responsible for the structure and motion of galaxies we observe. Observations of Type Ia Supernovae (SNe Ia) imply that dark matter and normal matter alone do not make up the entire content of the universe. The remaining 70% is composed of "dark energy," which acts like a repulsive gravitational force and is responsible for the current observed accelerated expansion of the Universe.

Consider a galaxy's spectrum with an absorption line whose measured wavelength on Earth is λ_{e}. The actual measurement at Earth of this absorption line λ_{o} is usually not the same. It is shifted according to the galaxies motion relative to us. We quantify this shift according to the redshift

$$z = (\lambda_{\mathrm{o}} - \lambda_{\mathrm{e}})/\lambda_{\mathrm{e}}. \tag{1.1}$$

In 1929, Edwin Hubble plotted the motions of galaxies relative to Earth as a function of distance. He observed that galaxies are receding from us at a rate proportional to their distance. We now observe that the rate at which galaxies are moving away from each other is greater today than it was in the past. To explain this accelerated expansion, we need an energy that permeates all of space and acts in opposition to gravity, driving galaxies away from each other. We call this energy dark energy.

1.1 MEASURING PROPERTIES OF THE UNIVERSE

A Hubble diagram plotting a measure of distance as a function of redshift reveals that galaxies in the Universe are receding from Earth at a rate approximately proportional to their distance from Earth. Measuring the redshift encodes a galaxy's motion relative to Earth and can be done easily and accurately from a spectrum. Distances in the Universe are much harder to measure.

Suppose we have an object of known total luminosity. The inverse square law describes how the observed brightness of a source is related to its distance given the luminosity. It is often convenient to recast the inverse square law in terms of magnitudes such that a change in 5 magnitudes corresponds to a factor of 100 in brightness. Thus, the measured brightness of a source in magnitudes at distance D_L is

$$m = M + 5\log_{10}(D_L/10\text{pc}). \tag{1.2}$$

where the absolute magnitude M is the energy flux of the source observed at a distance of 10 parsecs. It is a measure of the object's luminosity.

If we know M for an object, we simply measure m and we can determine the luminosity distance D_L. Such objects are called standard candles. If we can determine what fundamental cosmological parameters control the luminosity distance, we can use a Hubble diagram to infer properties of our Universe.

1.1.1 The Luminosity Distance

To understand more deeply the dynamics of the Universe we must first learn how to calculate distances in an expanding universe. Consider an homogeneous, isotropic, and flat universe such that the space-time separation between two events according to special relativity is given by

$$ds^2 = -c^2dt^2 + a^2(t)[dr^2 + r^2(d\theta^2 + sin^2\theta d\phi^2)] \tag{1.3}$$

where t is the cosmological proper time (the time measured by an observer who sees the universe expanding around him), (r, θ, ϕ) are the comoving coordinates of a point in space such that if the expansion were perfectly homogeneous and isotropic they remain constant in time, and where the scale factor $a(t)$ describes how distances expand and contract over time. Ultimately we would like to write the scale factor in terms of fundamental properties of the Universe. c is the speed of light and will be set to one onward.

We can find a relationship between scale factor and time by considering two pulses of light. One pulse of light is emitted at time t_e and is observed after traveling a null geodesic at time t_o. We can determine the distance the photon has traveled according to

$$\begin{aligned} ds^2 &= -dt^2 + a^2(t)dr^2 = 0 && (1.4)\\ dt^2 &= a^2(t)dr^2 && (1.5)\\ r &= \int_{t_e}^{t_o} \frac{dt}{a(t)}. && (1.6) \end{aligned}$$

A second pulse of light is emitted at time $t_e + \delta t_e$ and observed at time $t_o + \delta t_o$ which travels the same comoving distance such that

$$r = \int_{t_e+\delta t_e}^{t_o+\delta t_o} \frac{dt}{a(t)}. \tag{1.7}$$

These equations can be combined to show

$$\int_{t_e}^{t_e+\delta t_e} \frac{dt}{a(t)} = \int_{t_o}^{t_o+\delta t_o} \frac{dt}{a(t)}. \tag{1.8}$$

This means that the integral of $dt/a(t)$ is the same between the emitted pulses and observed pulses of light. If we look at the first order perturbation such that in the time between the two pulses of light the universe has not expanded by any appreciable amount we find

$$\frac{\delta t_o}{a(t_o)} = \frac{\delta t_e}{a(t_e)} \tag{1.9}$$

If the time between the two pulses of light define the period of the wave then we can rewrite the above equation in terms of wavelength to find

$$\frac{\lambda_o}{a(t_o)} = \frac{\lambda_e}{a(t_e)} \tag{1.10}$$

which can be rewritten in terms of redshift as follows

$$1 + z = \frac{a(t_o)}{a(t_e)}. \tag{1.11}$$

The redshift captures how much the Universe has expanded in the time light left a distant galaxy and traveled to us.

The proper distance is the length of the spatial geodesic between two points when the scale factor is fixed. For example, the proper distance between an observer and a galaxy in a flat universe would be found by integrating over the radial comoving coordinate at fixed time

$$d_p = a(t) \int_0^r dr = a(t)r \tag{1.12}$$

as the angle (θ, ϕ) are constant. The inverse square law for a static universe would then be the familiar

$$F = \frac{L_{\text{emit}}}{4\pi d_p^2}. \tag{1.13}$$

where F is the flux and L_{emit} is the luminosity emitted at the source.

To generalize the inverse square law for an expanding universe consider the energy per unit time moving through a comoving spherical shell with radius r. The area of this shell today would be $4\pi a^2(t_0)r^2$. We first note that the energy emitted from a photon at the source goes down by a factor of $1 + z$ due to the expansion. Additionally photons will travel farther on a comoving grid at early times than at later times because the physical distance in smaller. Therefore the number of photons crossing a shell for a fixed time interval will be smaller today than at emission by a factor of $1 + z$. We can rewrite the inverse square law for an expanding universe as

$$F = \frac{L_{\text{emit}}}{4\pi a^2(t_0)r^2(1+z)^2.} \tag{1.14}$$

To keep the same form for the inverse square law as for a static universe we define the luminosity distance for a flat universe to be

$$d_L \equiv a(t_0)r(1+z). \tag{1.15}$$

Thus to calculate the luminosity distance requires calculating Equation 1.6, the null geodesic traveled by a photon.

It is customary to rewrite Equation 1.6 in terms of redshift using Equation 1.11. We also define

$$H \equiv \frac{\dot{a}}{a} \tag{1.16}$$

where the dot indicates time derivative. Equation 1.6 can now be recast as follows

$$\begin{aligned} r &= \int_{a(t_e)}^{a(t_0)} \frac{da}{\dot{a}a} && (1.17)\\ &= \int_{a(t_e)}^{a(t_0)} \frac{da}{a^2 H(a)} && (1.18)\\ &= \frac{1}{a(t_0)} \int_0^z \frac{dz}{H(z)} && (1.19) \end{aligned}$$

We must first integrate Equation 1.19 before we can calculate the luminosity distance.

1.1.2 Friedmann Equation

Our goal is to understand how the scale factor $a(t)$ evolves with time and determine the fundamental parameters which control the luminosity distance. To do this we examine two forms of energy conservation: the Friedmann equation and the first law of thermodynamics.

The Friedmann equation in the Newtonian approximation states that the total gravitational potential energy and kinetic energy of expansion remains constant. We start with

$$\begin{aligned} \ddot{r} &= \frac{GM}{r^2} && (1.20)\\ &= \frac{4\pi}{3} G\rho r && (1.21) \end{aligned}$$

for a uniform density ρ. We can integrate once to get

$$\dot{r}^2 = \frac{8\pi G\rho r^2}{3}. \tag{1.22}$$

Rewriting in terms of the scale factor we find

$$\left(\frac{\dot{r}}{r}\right)^2 = \left(\frac{\dot{a}}{a}\right)^2 = \frac{8\pi G\rho}{3}. \tag{1.23}$$

This is the Friedmann equation in a flat universe. We would like to integrate this equation to find out how the scale factor evolves as a function of the different densities of "stuff" that make up our universe.

1.1.3 Fluid Equation

The first law of thermodynamics tells us that the heat flow into or out of a region is equal to the change in internal energy E and the pressure P multiplied by the change in volume V of the region or:

$$\dot{Q} = \dot{E} + P\dot{V} \tag{1.24}$$

If the universe is composed of a homogeneous fluid then

$$\dot{E} = -P\dot{V}. \tag{1.25}$$

If we consider a sphere expanding with the universe of comoving radius r_s then the volume of the sphere is

$$V(t) = \frac{4\pi}{3} r_s^3 a(t)^3 \tag{1.26}$$

and the energy of the sphere is

$$E(t) = V(t)\rho(t) \tag{1.27}$$

Taking the time derivative of Equation 1.27 and substituting in the rate of change of the sphere's volume we find

$$\begin{aligned} E &= \rho V & (1.28)\\ \dot{E} &= \dot{\rho}V + \rho\dot{V} & (1.29)\\ &= V\left(\dot{\rho} + 3\frac{\dot{a}}{a}\rho\right). & (1.30) \end{aligned}$$

Combining Equation 1.25, Equation 1.30, and the time derivative of Equation 1.26 we find

$$\dot{\rho} + 3\frac{\dot{a}}{a}(\rho + P) = 0. \tag{1.31}$$

This is the fluid equation.

1.1.4 Equation of State

If we assume an equation of state for "the stuff" in the universe of the form

$$P = w\rho \tag{1.32}$$

where w is constant, we can eliminate the pressure term in the fluid equation. This would give us a relationship for how the density evolves with scale factor which then allows us to integrate Equation 1.23. Substituting the equation of state into the fluid equation and integrating yields

$$\rho_w = \rho_{0,w} a^{-3(1+w)} \tag{1.33}$$

where the energy density of the w component at present day is $\rho_{0,w}$.

The w component of the Universe can be divided into non-relativistic matter, radiation, and vacuum energy. For non-relativistic matter, $w = 0$ so that $\rho_M \propto a^{-3}$. This is because we can write the energy density as $\rho_M = nE$ where n is the number density of particles and E is the mean energy. As the universe expands, the number density drops by a^{-3}. For relativistic particles, $w = 1/3$ which yields $\rho_R \propto a^{-4}$. The energy for relativistic particles is inversely proportional to wavelength and thus inversely proportional to the scale factor. This in addition to the drop in number density with scale factor yields a^{-4}. For vacuum energy (Λ), $w = -1$ such that the density is constant and does not change with scale factor.

We can now rewrite the Friedmann equation for a flat universe in terms of these three components

$$H^2 = \frac{8\pi G}{3}\left(\rho_M + \rho_R + \rho_\Lambda\right) \tag{1.34}$$

$$H^2 = \frac{8\pi G}{3}\left(\rho_{0,M} a^{-3} + \rho_{0,R} a^{-4} + \rho_{0,\Lambda}\right) \tag{1.35}$$

At this point is it useful to define the critical density as

$$\rho_{\text{crit}} \equiv \frac{3H_0^2}{8\pi G} \tag{1.36}$$

We can now scale each density as $\Omega_w = \rho_{0,w}/\rho_{\text{crit}}$ and rewrite the Friedmann equation to yield

$$H^2 = H_0^2\left(\Omega_M a^{-3} + \Omega_R a^{-4} + \Omega_\Lambda\right). \tag{1.37}$$

1.1.5 Luminosity Distance and the Matter-Energy Content of the Universe

We are now equipped to write out the luminosity distance in terms of the matter-energy content of the Universe. Using Equation 1.19 and Equation 1.37, the luminosity distance today described by a flat ΛCDM universe described by an FRW metric is given by

$$d_L = \frac{1+z}{H_0} \int_0^z \frac{dz}{(\Omega_M (1+z)^3 + \Omega_\Lambda)^{1/2}}. \tag{1.38}$$

where we have assumed that the contribution from relativistic matter today is negligible and that the scale factor today is one. This equation tells us that if we know the luminosity distance to a set of objects and we know their redshift, we can learn something about Ω_m, Ω_Λ and H_0. SNe Ia constitute such a set.

The standard candle nature of SNe Ia make them useful for measuring cosmological parameters (see e.g. Riess et al. (1998); Perlmutter et al. (1999). They have a standardizeable luminosity such that relative distances can be calculated accurately. By measuring the apparent magnitude, m, of a Type Ia Supernova (SN Ia) we can calculate its luminosity distance according to Eq 1.2. As we have no direct measure of the luminosity of a SN Ia, we must rely on the distance ladder which is anchored nearby with masers and Cepheid variables to calibrate the absolute magnitude of SNe Ia (Riess et al., 2009).

In Figure 1.1.5 is a Hubble diagram from Conley et al. (2011) which was created from the most recent supernova data sets; it is the brightness of the supernova corrected for light curve shape as a function of redshift. The line fitted to the data is the best fit cosmology assuming a flat universe and constant dark energy equation of state. Ω_M and the dark energy equation of state parameter w are the free parameters in this fit. In the bottom panel are the residuals from the best fit line. In Figure 1.1.5 are the constraints placed on w and Ω_M including all statistical and systematic uncertainties for this sample of SNe Ia. These results show that for a flat universe and constant dark energy equation of state parameter,$\Omega_M \simeq 0.25 (\Omega_\Lambda = 0.75)$ which indicates that most of the energy in the Universe is in the form of dark energy and that $w = -1$, which indicates that the Universe is accelerating in its expansion.

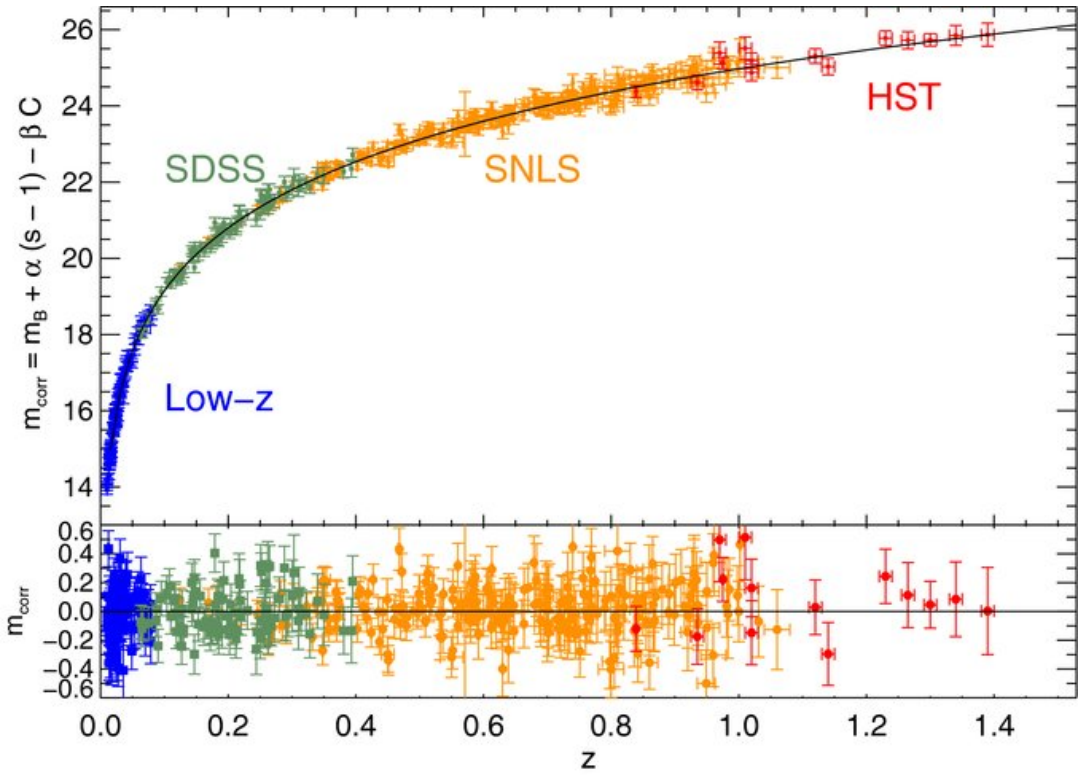

Figure 1 Supernova brightness corrected for light curve shape as a function of redshift (Hubble diagram) using a recent compilation of SNe Ia from Conley et al. (2011). The best fit cosmology as a function of constant equation of state parameter w and Ω_M for a flat universe is plotted as the solid line. Residuals with respect to this line are plotted in the bottom panel. © AAS. Reproduced with permission. http://dx.doi.org/10.1088/0067-0049/192/1/1

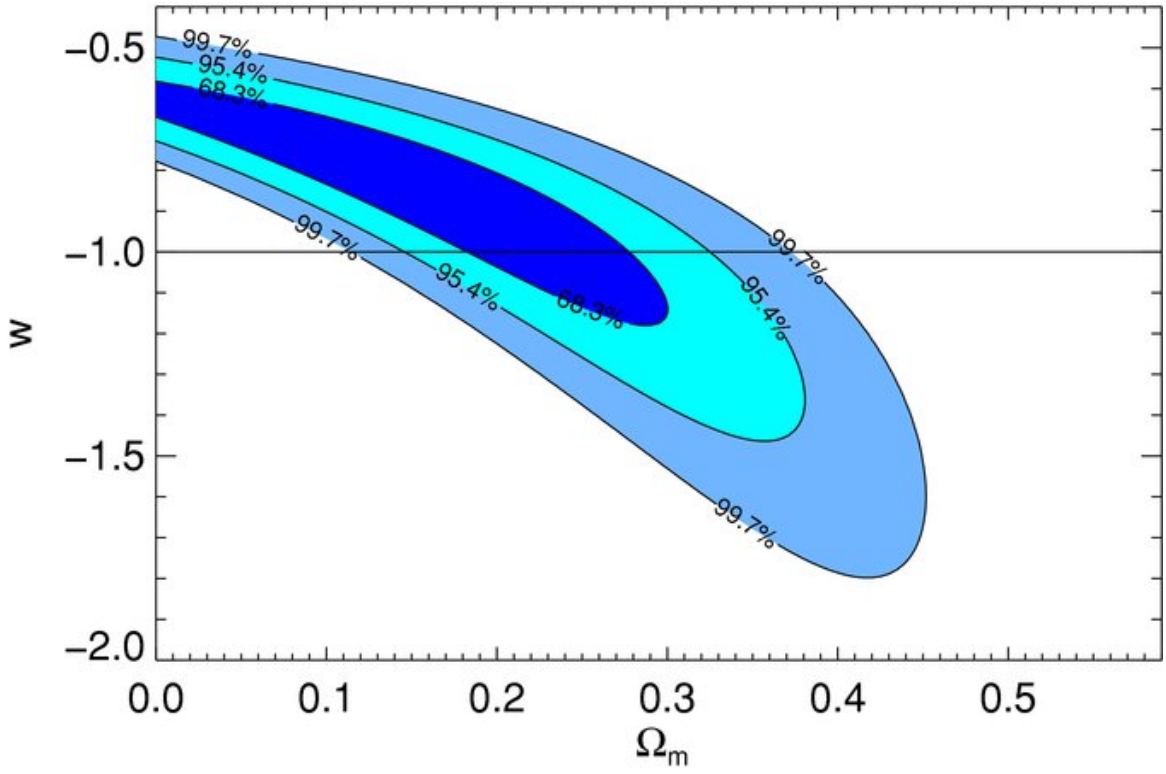

Figure 2 Cosmological constraints from Conley et al. (2011) including statistical and systematic uncertainty. The sample used in this analysis favors a universe dominated by dark energy which is accelerating in its expansion. © AAS. Reproduced with permission. http://dx.doi.org/10.1088/0067-0049/192/1/1

1.2 THE LOCAL PECULIAR VELOCITY FIELD

Accurate distance estimates to large sets of galaxies through SN Ia measurements allow us to model the local peculiar velocity field. We know that dark energy acts only on large scales. This means that local motions, like the Earth traveling around the Sun, are still governed by gravity. Gravity will be the dominate force that acts on large objects which are close together or bound. Galaxies which are gravitationally bound will collide in spite of dark energy. This will depend on how much matter - dark matter in particular - is in these galaxies.

Measuring the rate of expansion - the growing separation between galaxies - is difficult in areas of space where objects are heavily influenced by gravity. This causes "peculiar motions" which counteract the motions caused by the expansion of the Universe. Peculiar motions are larger in areas with more mass, like clusters of galaxies, which consequently contain more dark matter. By modeling these peculiar motions in the nearby Universe, we can limit gravitational effects on our understanding of dark energy and on derived cosmological parameters (Cooray & Caldwell, 2006; Hui & Greene, 2006; Gordon et al., 2007; Neill et al., 2007; Davis et al., 2010b).

More precisely, on smaller physical scales large scale structure induces peculiar velocities that create large fluctuations in redshift. Recall that the redshift encodes the total motion of the source relative to Earth. We are therefore in a regime where a sizable component of the redshift is due to peculiar motion. This limits the cosmological utility of SN Ia as the redshift is assumed to be from cosmic expansion. Averaging over many SNe Ia reduces scatter caused by random motions but not those caused by coherent large scale motions. Recent work has shown significant peculiar velocity effects on cosmological parameters out to $z < 0.1$ (Cooray & Caldwell, 2006; Hui & Greene, 2006); where peculiar velocities contaminate the Hubble diagram in the nearby redshift regime which adds uncertainty to derived cosmological parameters.

The total velocity (peculiar velocity plus velocity due to cosmic expansion) of an object can be measured from the redshift. With an accurate distance we can calculate the velocity of a galaxy due to the expansion of the universe. The peculiar velocity of an object given

the redshift z and cosmological distance d is

$$U = H_0 d_l(z) - H_0 d \tag{1.39}$$

where H_0 is the Hubble parameter and $H_0 d_l(z)$ is the recessional velocity described by

$$H_0\, d_l(z) = (1+z) \int_0^z \left[\Omega_M (1+z')^3 + \Omega_\Lambda\right]^{-1/2} dz'. \tag{1.40}$$

Redshifts to host galaxies of SN Ia can be measured accurately with an error $\sigma_z \sim 0.001$. Thus the accuracy of a peculiar velocity measurement depends on the distance uncertainty.

One can model the peculiar velocity field once the position and peculiar velocity for a set of objects is known. The peculiar velocity of an object is influenced by matter on all scales. Modeling the flow field is therefore a direct probe of the distribution of dark matter. Calculating the dipole moment of the peculiar velocity field, or bulk flow, is an example of a measurement which helps us investigate the density fluctuations on large scales. One expects these bulk motions to converge to zero with increasing volume in the rest frame of the CMB with the rate of convergence depending on the amplitude of the matter perturbations (Zaroubi, 2002). This fact motivates accurate modeling of the local peculiar velocity field.

1.3 TYPE IA SUPERNOVAE AS STANDARD CANDLES

Supernovae are divided into two classes according to the deficiency (Type I) and presence (Type II) of hydrogen. The Type Ia subclass exhibits strong Si II absorption in its early-time spectra and blended emission lines of iron-group elements in the late-time spectra (Filippenko, 1997). As a group they display nearly uniform spectra and light curves. Figure 3 shows a typical quasi-bolometric light curve and spectral evolution (Figure 3 from Howell (2011)). SNe Ia rise in brightness and peak 15-20 days after the initial explosion. Over the next month they decline in brightness by about 3 magnitudes and continue declining at a rate of about one magnitude per month. Initially the spectra show only absorption lines probing the outer layers of the supernova. As the supernova expands the photosphere

(light emitting region) recedes and spectra probe the inner regions of the ejecta. Around the time of maximum the spectrum shows emission at the rest wavelength and blueshifted absorption i.e. P-Cygni profiles. Around one month after peak brightness when the ejecta starts to become optically thin, the spectra become dominated by emission features. Late time spectra feature emission lines from iron-peak elements which were created near the center of the explosion.

SNe Ia are found in young and old stellar populations. Spectral evolution analysis show a total ejecta mass near Chandrasekhar mass and that many Type Ia progenitors have the same mass (Mazzali et al., 2007). As a result, SNe Ia are believed to be the explosion of a carbon-oxygen white dwarf which has reached the Chandrasekhar mass limit by accreting mass from a companion (single degenerate scenario) or via the collision of two white dwarfs (double degenerate scenario). A white dwarf is the stellar remnant of a low to medium mass star (0.5-8 $M_{\odot}$) which was hot enough to fuse helium into carbon and oxygen in its core before expelling its outer material, creating a planetary nebula. The interior of the carbon and oxygen core remnant is supported by electron degeneracy pressure while the outer layers of non-degenerate matter radiate as a black body and slowly cool. The mass of a non-rotating white dwarf is limited to the Chandrasekhar mass ($\sim 1.4M_{\odot}$), the upper limit to the mass of an electron-degenerate object. For the white dwarf to become a Type Ia it must exceed this mass by accreting material from a companion or merging with another white dwarf such that the combined mass is greater than the Chandrasekhar mass. The increase in mass compresses the core thereby raising the temperature and the density. Eventually, electron degeneracy pressure is no longer enough to support the growing mass of the white dwarf and the core collapses producing a thermonuclear runaway creating a SN Ia.

It is generally accepted that the thermonuclear runaway of a carbon-oxygen white dwarf near the Chandrasekhar mass is responsible for the standard nature of Type Ia's. The products of helium burning, C^{12} and O^{16}, are efficiently combined into Ni^{56}. The light curve of a SN Ia - how the brightness rises and falls overtime - is powered by the radioactive decay of Ni^{56} into Co^{56} into Fe^{56}. Each decay process adds an exponential component to the light curve and drives the shape of the light curve after maximum light. The initial light curve of a SN Ia is shaped by the radiative diffusion of an expanding sphere of ejecta. A large ejecta

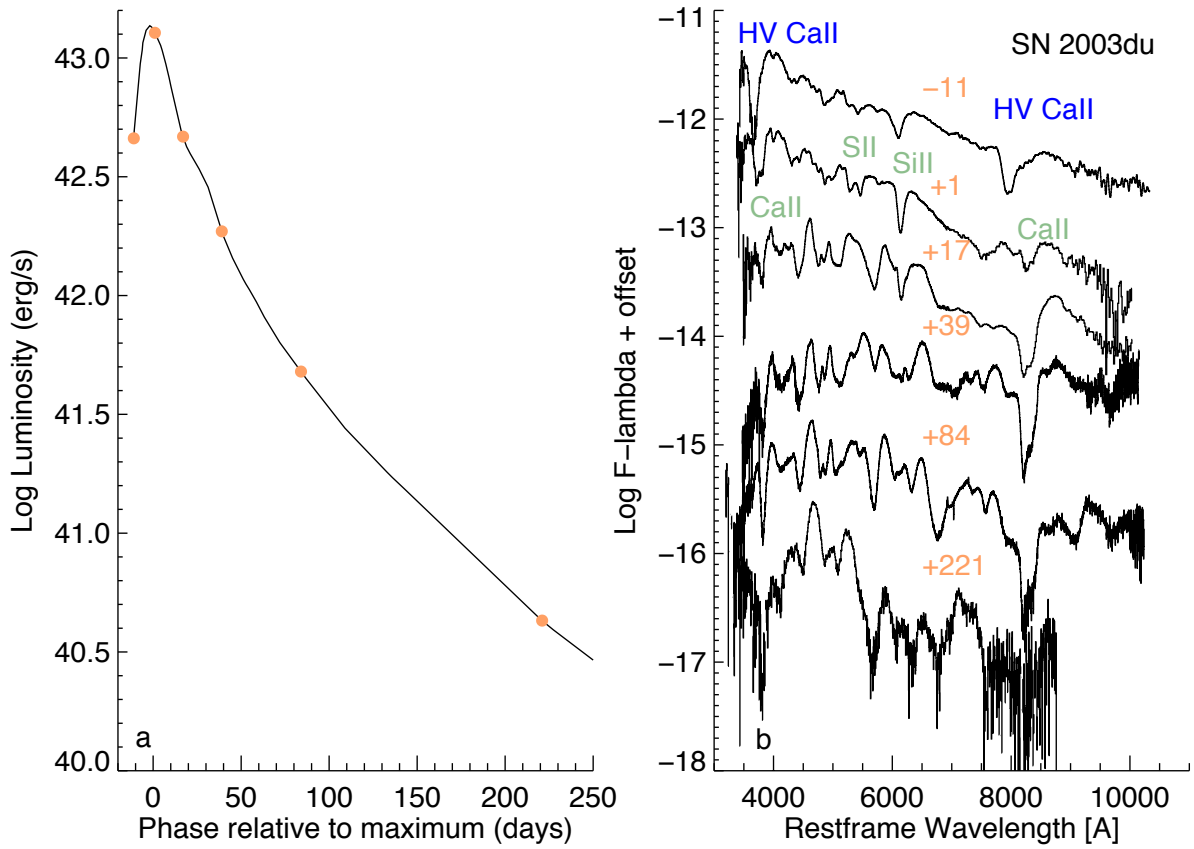

Figure 3 Quasi-bolometric light curve and spectra from 2003du. Panel a shows the log luminosity of the explosion as a function of time. The phase is shifted so that the time of maximum corresponds to 0 days. The SN Ia rises in brightness over 2 weeks and declines by 3 magnitudes over the first month after peak brightness. The late time light curve follows a steady decline of about 1 magnitude per month. Panel b shows spectra which were taken according to the orange points in panel a. The phase in days is also listed above each spectrum. Reprinted by permission from Macmillan Publishers Ltd: Nature Communications Howell (2011), http://dx.doi.org/10.1038/ncomms1344

mass corresponds to a longer radiative diffusion time and has the effect of smearing out the Ni^{56} peak. Understanding the interplay between the radiative diffusion and radioactive decay time scales of the SN Ia enable us to calibrate their luminosity and use them as cosmological distance indicators.

1.3.1 Progenitor Scenarios

It is generally accepted that Type Ia's must be the thermonuclear runaway of a carbon-oxygen white dwarf although it is unclear how the progenitor system reaches the Chandrasekhar mass and what process leads to its ignition and explosion. Two popular progenitor mechanisms are the single-degenerate scenario in which the white dwarf accretes mass from a non-degenerate companion (Whelan & Iben, 1973) star and the double-degenerate scenario which involves the merger of two white dwarfs (Webbink, 1984).

In the single degenerate model a white dwarf accretes mass from a secondary companion star. One possible mechanism for accretion is via Roche lobe overflow. The Roche lobe is the region of space around the companion star for which material is bound to that star. Once the star expands beyond its Roche lobe material can be accreted onto the white dwarf. Mass transfer can occur via Roche lobe overflow when the companion stars is a main sequence star (van den Heuvel et al., 1992), a slightly evolved subgiant (Han & Podsiadlowski, 2004) or a helium star (Tutukov & Yungelson, 1996) and has a orbital period less than several days. Mass transfer can also occur when the companion is a low mass red giant with a long orbital period extending from tens to hundreds of days (Li & van den Heuvel, 1997). In this situation a strong wind is employed to stabilize the mass transfer rate (Hachisu et al., 1996; Li & van den Heuvel, 1997).

The goal in these models is to grow the white dwarf in mass with stable nuclear burning on the surface of the white dwarf of hydrogen into helium or through direct transfer of helium from the companion star (Nomoto, 1982). For each type of secondary companion a narrow range of accretion rates are allowable. It the accretion rates are too fast, the accretor can expand into a red-giant-like configuration and engulf the companion into a common envelope (Iben & Tutukov, 1984). If the material is accreted too slowly the hydrogen forms

a cold degenerate layer until it ignites and burns in a nova eruption on the surface of the white dwarf (Starrfield et al., 1972). It is expected that most of the accreted material is blown away in this process along with some of the original white dwarf material (Yaron et al., 2005). Uncertainty in the common envelope phase and uncertainty in the fraction of transferred mass retained by white dwarf lead to a wide range of white dwarf growth scenarios (Bours et al., 2013).

The double degenerate scenario features the merger of two white dwarfs through an accretion disk configuration or through a collisional one where two white dwarfs collide head on. In the first configuration the more-massive white dwarf tidally disrupts and accretes the lower-mass white dwarf (see e.g. Lorén-Aguilar et al. (2009)). Carbon and oxygen are efficiently transferred to the larger white dwarf eventually leading to carbon ignition in the core. It is possible that the efficient mass transfer could lead to off-center ignition and produce orientation effects (see e.g. Moll et al. (2013)) which would not reproduce the uniform behavior of SNe Ia. In the second configuration two white dwarfs collide in some dense stellar environment such as a globular cluster or galactic nuclei (Benz et al., 1989; Raskin et al., 2009). In this situation a shock-triggered thermonuclear explosion arises at the collision site (Rosswog et al., 2009) rather than carbon ignition in the core.

1.3.2 Observational tests of progenitor systems

Here I highlight some observational tests and techniques for testing different progenitor models. For a more complete discussion see Maoz et al. (2013).

1.3.2.1 Pre-explosion data Perhaps one of the clearest paths to determining what the progenitor system of a SN Ia is would be to observe one before it exploded. Unfortunately no clear progenitor system has been detected although upper limits on progenitor luminosities have been estimated from pre-explosion images (see e.g. Graur & Maoz (2012b,a); Maoz & Mannucci (2008); Nelemans et al. (2008)). The most exciting pre-explosion progenitor limits have come from the recent SN 2011fe in the nearby galaxy M101 (see Chomiuk (2013) for a review). Because of its close proximity it is the earliest discovery of a SN Ia to date (Nugent

et al., 2011). It also happens to be incredibly ordinary (Richmond & Smith, 2012) which makes it useful for addressing progenitor questions. The exploding star is likely a carbon-oxygen white dwarf (Nugent et al., 2011) and upper limits from pre-explosion images rule out luminous redgiants and most helium stars as the companion (Li et al., 2011b).

1.3.2.2 Event Rates Another test of progenitor models is to look for potential progenitor systems in local galaxies, measure their properties and numbers, see if that matches SN Ia rates and properties. For example, one possible progenitor system is a recurrent nova (Schaefer, 2010; Kato & Hachisu, 2012). A nova eruption is the result of a thermonuclear runaway event on the surface of a white dwarf as previously mentioned. The white dwarf accretes hydrogen (or other material) from a companion, unstable hydrogen shell burning sets in and the white dwarf becomes extremely bright as this envelope expands. Recurrent novae are those systems which have such an outburst with rates greater than once per century. There are 10 known galactic recurrent novae (Schaefer, 2010). It is believed that the white dwarf must be near the Chandrasekhar mass for these systems to attain such a nova frequency. A large white dwarf mass indicates high surface gravity such that less material must be accreted to attain a thermonuclear runaway. High accretion rates would also lead to a short recurrence timescale. A large white dwarf mass and high accretion rate make these systems excellent SN Ia progenitor candidates although there is some evidence that recurrent novae are systems for which the white dwarf actually loses mass with time (Patterson et al., 2013).

Based on the frequency of occurrence of recurrent novae in local galaxies it it unlikely that they make up all SNe Ia (della Valle & Livio, 1996). Schaefer (2010) estimate that $\sim$ 100 classified novae are actually recurrent novae and an analysis of the Galactic spatial distribution suggest that a large fraction are missed bumping the galactic number to about 300. However to achieve a Galactic supernova rate of once per 200 years over 3300 systems are needed (Maoz et al., 2013). Therefore recurrent novae cannot make up all, if any, SNe Ia.

A similar prescription can be applied to test the double-degenerate scenario. First search the Galactic neighborhood for white dwarf binaries with periods short enough to allow merger through gravitational decay within a reasonable time (a Hubble time) and derive a Galactic

white dwarf merger rate. This merger rate should then match the Galactic supernova rate if they are indeed the progenitors of most SNe Ia.

The ESO SN Ia Progenitor Survey (SPY) project aims at finding merging double degenerate systems (Geier et al., 2010; Nelemans et al., 2005). They have found ~ 100 binary candidates and several which are expected to merge within a Hubble time. A statistical interpretation of these numbers in terms of selection effects and survey inefficiencies has yet to be published. Nevertheless Toonen et al. (2012) use binary population synthesis code techniques to estimate properties of observed white dwarf binaries and find reasonable agreement with a compilation of known binaries from the literature. Further, they derive a Galactic white dwarf merger rate which is agreement with estimates of the SN Ia rate for Milky Way type galaxies of about 2 per century (Li et al., 2011a).

Similar to matching progenitor rates and SN Ia rates, one can examine SN Ia rates and the progenitor dependence on environment and time. Different progenitor systems evolve at different timescales which affect the SN Ia rate. One measure of the progenitors environmental impact of the SN Ia rate is the delay-time distribution (DTD) which quantifies how much time has passed between an outburst of star formation and the SN Ia event. It is the distribution of times between star formation and SN Ia explosion. Measuring the DTD is a major goal of SN Ia rate measurements (see Maoz & Mannucci (2012) for a review).

1.3.2.3 Remnants Examining the aftermath of a SN Ia explosion provides insight into the progenitor system. To test the single degenerate scenario, one can search for the surviving companion in SN Ia remnants. This star is expected to have unusual velocity, temperature, or luminosity and could be detected from large proper or radial motions (Marietta et al., 2000; Canal et al., 2001; Pan et al., 2013). The Tycho SN 1572 remnant is an SN Ia remnant in the local neighborhood of the Milky Way (Rest et al., 2008) and is ideal for companion star searches. Unfortunately results based on radial velocities, proper motions, and rotation velocities for a surviving companion star in Tycho's supernova remnant are in disagreement (Ruiz-Lapuente et al., 2004; Fuhrmann, 2005; Ihara et al., 2007; Kerzendorf et al., 2009).

It is also expected that the companion star loses mass during the explosion and consequently must have an overextended envelope. As a result, the companion becomes signifi-

cantly more luminous. SNR 0509-67.5 in the Large Magellanic Cloud also appears to be a SN Ia (Badenes et al., 2008) but deep imaging with the Hubble Space Telescope sets the limit to the companion star which corresponds to a late-K type main sequence star of 0.5 solar masses (Schaefer & Pagnotta, 2012). This essentially rules out the single degenerate scenario for this remnant. The lack of a leftover luminous companion star in other nearby supernova remnants has provided additional evidence against the single degenerate scenario (Shappee et al., 2013).

One can also construct hydrodynamical models of SN Ia events to try and reproduce remnants thought to be Ia's. Different initial conditions will produce different geometries, dynamics, X-ray spectrum, etc. (Kosenko et al., 2011; Patnaude et al., 2012). For example, Badenes et al. (2007) model the X-ray emission in seven remnants. They search for large wind-blown cavities in the inter-stellar medium which are expected from rapidly accreting white dwarfs in the wind-regulated accretion picture (Hachisu et al., 1996). They find that the observations do not support this scenario and the growth of white dwarfs must proceed another way.

1.3.2.4 Observed Event Properties Finally, one can use the observed properties of the SN Ia itself to understand its progenitor system. For example, spectra from the event contain many clues to understanding the progenitor. In some single degenerate scenarios, hydrogen is accreted onto the white dwarf from a companion star. One could therefore search for hydrogen emission in the early time spectra (Marietta et al., 2000; Mattila et al., 2005). Polarization measurements reveal clues about the symmetry of an event. Spectropolarization measurements are especially useful for addressing the progenitor problem as most progenitor systems have an inherent asymmetry e.g. an accretion disk, rotational flattening, off-center ignition, merger (see Wang & Wheeler (2008) for a review). Intervening absorption lines give clues to the local environment of the SN Ia. For example, blueshifted time-varying Na I D absorption lines may indicate circumstellar material local to the SN Ia (Maguire et al., 2013). Shocks from the explosion eject hitting the companion star may be observable in early time data and are another test of the single degenerate scenario (Kasen, 2010).

One can also use a modeling approach to reproduce observed spectra and light curves.

The chemical and velocity structure of the ejecta is revealed as the supernova expands and the photosphere recedes. This can be used to differentiate between progenitor models. Overall good agreement can be found between data and models but there are yet many shortcomings in the details (Blondin et al., 2011; Röpke et al., 2012; Kasen et al., 2009).

1.3.3 Standardizing SN Ia Light Curves

SN Ia light curves display a color-luminosity and stretch-luminosity relationship. Intrinsically faint supernovae are redder and have faster declining light curves (Phillips, 1993; Riess et al., 1996). Nevertheless one can achieve 10-15% scatter in peak luminosity, better than 6% precision in distance, after corrections for light curve shape and color (see e.g. Jha et al. (2007a)).

The goal of most light curve fitters is to standardize the shape of the light curve through employment of the observed stretch- and color-luminosity relationships so that an accurate distance can be measured. In one parameterization of the light curve the distance modulus for a SN Ia can be written as

$$\mu_B = m_B - M - 5\log(\frac{H_0}{65 \text{ km s}^{-1}\text{Mpc}^{-1}}) + \alpha(s-1) - \beta c \tag{1.41}$$

where m_B is the peak B-band apparent magnitude, M is the absolute magnitude of the supernova, s is the stretch correction, α encodes the fact that fainter supernovae have faster declining light curves, c is the color correction and β is the slope of the color-luminosity relationship. H_0, M, α, and β, are fixed quantities which are often measured from a training set and other data. m_B, s, and c are measured for each individual light curve.

When fitting a light curve one must correct for the fact that redder supernovae are fainter. This is in part a result of the intrinsic color-luminosity relation but also a result of reddening and extinction due to dust. MLCS2k2 (Jha et al., 2007a) attempts to make this separation and perform corrections for each. SALT2 (Guy et al., 2007) and SifTO (Conley & Sullivan, 2011) adopt the approach that the data are not yet good enough to make this separation and make an empirical reddening correction.

One can separate the effects of intrinsic reddening and reddening due to dust with near-infrared (NIR) observations, where dust becomes transparent. SNe Ia show reduced scatter

in NIR *before* light curve shape and color corrections (Wood-Vasey et al., 2008a). So in addition to being less affected by dust, SNe Ia appear to have more standard peak magnitudes in the NIR.

This is supported in recent theoretical work by Kasen (2006). They generate synthetic light curves using time-dependent multi-group radiative transfer calculations. They are able to reproduce a peculiar feature of near-infrared light curves, a secondary maximum, and find reasonable agreement with actual SN Ia light curves. The secondary maximum is claimed to be a result of the ionization evolution of iron group elements in the ejecta. The temperature of the ejecta decreases with radius and as a result, the transition between the double and single ionized states in the iron/cobalt gas, which occurs at a temperature around 7000K, is a thin shell of material. Initially this shell is at the outer edge of the ejecta. As the supernova cools, this shell or ionization front moves inward. The sudden re-brightening of the SN Ia is thought to be a result of when this front hits the iron-rich core of the ejecta. The iron-rich gas becomes phosphorescent and is very effective at redistributing UV/blue radiation to infrared wavelengths. Importantly, their models also confirm that SNe Ia are excellent standard candles in the NIR.

Unfortunately, NIR observations are difficult to take from the ground due to significant absorption and emission from water vapor in the atmosphere. This is compounded by the fact that as supernovae are observed at higher redshift the region of the spectrum viewed through a given filter changes. To create a rest-frame near-infrared Hubble diagram would therefore require observing high redshift supernovae at even longer wavelengths from the ground which is very challenging. As a result efforts from ground based NIR SN Ia searches like the Carnegie Supernova Project (Stritzinger et al., 2011; Contreras et al., 2010; Burns et al., 2011; Folatelli et al., 2010) and PAIRITEL (Wood-Vasey et al., 2008a) are focused on calibrating and standardizing nearby SN Ia NIR luminosities for potential future space based missions.

1.4 CURRENT LIMITATIONS OF SN IA DATA SETS

With distances estimates in hand to larges sets of galaxies through SN Ia measurements, we can measure the expansion history of the Universe or create models of how galaxies (matter) near the Milky Way are moving. SN Ia samples sizes are around several thousand when we combine results from searches like the Carnegie Supernova Project (Contreras et al., 2010; Stritzinger et al., 2011), the Center for Astrophysics Supernova Group (Hicken et al., 2009b, 2012), the Supernova Legacy Survey (Guy et al., 2010; Astier et al., 2006; Conley et al., 2011), the Sloan Digital Sky Survey-II Supernova Survey (Lampeitl et al., 2010; Sako et al., 2014), the ESSENCE Survey (Wood-Vasey et al., 2007; Miknaitis et al., 2007), the Lick Observatory Supernova Search (Ganeshalingam et al., 2010). and from individual efforts with the Hubble Space Telescope (Riess et al., 2004, 2007; Knop et al., 2003; Amanullah et al., 2010). Additional current and near-future surveys such as the Palomar Transient Factory[1] (Law et al., 2009), the Panoramic Survey Telescope and Rapid Response System (Pan-STARRS)[2], SkyMapper[3], and the Dark Energy Survey[4] will increase the sample by another order of magnitude and the Large Synoptic Survey Telescope (LSST) anticipates observing hundreds of thousands of well-measured SNe Ia (LSST Science Collaborations et al., 2009).

In this new era of SN Ia cosmology, weaknesses and limitations of our current approach to estimating cosmological parameters are becoming apparent. Traditionally when making cosmological inference with SNe Ia one calculates the χ^2 statistic (Conley et al., 2011; Kessler et al., 2009a; Wood-Vasey et al., 2007; Astier et al., 2006; Riess et al., 2004). One assumes that each measured distance modulus has a probability distribution function (PDF) described by a Gaussian with standard deviation σ. A model for the distance modulus is assumed which is a function of various cosmological and light curve parameters e.g. $\mu_{\rm model} = \mu_{\rm model}(\Omega_M, \Omega_\Lambda, w, z, \alpha, \beta)$. The likelihood for a single observation i is

$$p(\mu_i, z_i|\Omega_M, \Omega_\Lambda, w, \alpha, \beta) \propto \exp\left[-\frac{(\mu_i - \mu_{\rm model}(z_i, \Omega_M, \Omega_\Lambda, w, \alpha, \beta))^2}{2\sigma_i^2}\right]. \quad (1.42)$$

[1] http://www.astro.caltech.edu/ptf/
[2] http://pan-starrs.ifa.hawaii.edu/public/
[3] http://www.mso.anu.edu.au/skymapper/
[4] http://www.darkenergysurvey.org/

If the distance observations are independent after calibration such that there are no correlated uncertainties, the likelihood for each observation can be multiplied together. We can then derive the χ^2 statistic by taking the logarithm

$$-2\ln\left(p(\mu, z|\Omega_M, \Omega_\Lambda, w, \alpha, \beta)\right) = K + \sum_{i=1}^{N} \frac{(\mu_i - \mu_{\rm model}(z_i, \Omega_M, \Omega_\Lambda, w, \alpha, \beta))^2}{\sigma_i^2} \tag{1.43}$$

where K is an unimportant constant. Typically one must assume independent data with normally distributed uncertainties to use this form of the χ^2 statistic. Unfortunately there are significant systematic uncertainties including errors from calibration, survey design and cadence, host galaxy subtraction and intrinsic dust, population evolution, gravitational lensing, and peculiar velocities. All of these uncertainties contribute to a probability model which simply cannot be accurately described by a multivariate normal distribution.

Likewise, large numbers of SNe Ia allow one to model the local peculiar velocity field but also reveal systematic inconsistencies between different methods. While SNe Ia are ideal candidates to measure flow fields with only recently have there been enough data to perform these measurements. Comparisons between different galaxy and SN Ia surveys and techniques of modeling the field show results that are highly correlated and in agreement (Zaroubi, 2002; Hudson, 2003; Hudson et al., 2004; Radburn-Smith et al., 2004a; Pike & Hudson, 2005; Sarkar et al., 2007; Watkins & Feldman, 2007). However, when the data sets from different surveys are combined (namely Feldman et al. (2010), but Watkins et al. (2009) and Ma et al. (2010) also combine data sets) they are in disagreement with Nusser & Davis (2011). Errors in distance measurements are only part of the problem. The non-uniform sampling of objects across the sky due to the Galactic disk (affecting $\sim$40% of the sky) aggravate the systematic errors (Zaroubi, 2002). Such systematic errors cause inconsistencies among the different models. Fortunately the amount of SN Ia data continues to grow and modeling can be done with better precision allowing for investigation of the systematic errors that limit our measurements.

With the future influx of SN Ia data, statistical errors will be reduced but an understanding of systematic errors is required to make improvements on cosmological measurements (Albrecht et al., 2006a) and flow models.

1.5 DISSERTATION OVERVIEW

For my dissertation I have utilized the unique properties of SNe Ia coupled with modern statistics to address a variety of problems in astrophysics. These include improving flow models in the local Universe and demonstrating how Approximate Bayesian Computation (ABC) can tackle complicated likelihood functions in supernova cosmology. I also present the first results of a new near-infrared SN Ia survey called "SweetSpot."

The standard nature of SNe Ia and our ability to derive accurate distances to them make them ideal for developing peculiar velocity models. The motions of individual galaxies are perturbed from the overall smooth Hubble expansion due to Inhomogeneities in the matter distribution of our universe. From an accurate measurement of these motions, generally referred to as peculiar velocities or redshift space distortions, we can directly probe the dark matter distribution, the bias parameter β which specifies how galaxies follow the total underlying matter distribution, and improve cosmological measurements by reducing scatter in the Hubble Diagram at low redshift. Accurate distances, which result from accurate peculiar velocity models, are also important for studies of galaxy evolution – particularly at the low mass end where objects are only accessible in the very local universe. How well we model the local peculiar velocity field depends on how well we derive redshift-independent distances to objects and the sky and redshift coverage of the measurements we obtain. SNe Ia have a standardizeable luminosity from which we can derive redshift independent distances to with $\sim 6\%$ uncertainty making them ideal candidates to model local flows with. We have used the latest sample of SNe Ia to develop a method of modeling the local peculiar velocity field which accounts for the non-uniform distribution of objects across the sky. This work is presented in Chapter 2.

Cosmological inference becomes increasingly difficult when complex data-generating processes cannot be modeled by simple probability distributions. With the ever- increasing size of data sets in cosmology, there is increasing burden placed on adequate modeling; systematic errors in the model will dominate where previously these were swamped by statistical errors. For example, Gaussian distributions are an insufficient representation for errors in quantities like photometric redshifts. Likewise, it can be difficult to quantify analytically the

distribution of errors that are introduced in complex fitting codes. Without a simple form for these distributions, it becomes difficult to accurately construct a likelihood function for the data as a function of parameters of interest. ABC provides a means of probing the posterior distribution when direct calculation of a sufficiently accurate likelihood is intractable. ABC allows one to bypass direct calculation of the likelihood but instead relies upon the ability to simulate the forward process that generated the data. These simulations can naturally incorporate priors placed on nuisance parameters, and hence these can be marginalized in a natural way. I will present and discuss ABC methods in the context of supernova cosmology in Chapter 3

Recent work has suggested that SNe Ia are superior distance indicators in the NIR, with more standard peak JHKs magnitudes and relative insensitivity to reddening (Meikle, 2000; Krisciunas et al., 2004a, 2007). As a result, unlike optical SNe Ia, which are standardizeable candles, NIR SNe Ia appear to be truly standard candles at the $\sim 0.15 - 0.2$ mag level ($\sim 7-9\%$ in distance) (Krisciunas et al., 2004a; Wood-Vasey et al., 2008a; Folatelli et al., 2010). However the NIR observations to date have been limited by the power of the PAIRITEL and Swope telescopes to $cz < 10,000$ km s^1 where distance measurements are sensitive to peculiar velocity uncertainties, adding noise to the determination of the intrinsic dispersion of SNe Ia in the NIR. We have been awarded 7 nights during the 2011B semester to take observations of SNe Ia out to $z = 0.1$ where we are less sensitive to the effects of peculiar velocities.

Our focus is on improving our ability to standardize the SN Ia's total luminosity. We want to examine the intrinsic colors of the event at different times. We want to see if there is any correlation between the supernova event and the galaxy it resides in. We want to study dust in other galaxies and how that affects the brightness of the event. And most importantly, we want to provide a well-calibrated sample that will act as a stepping stone for more distant, space-based surveys. I will discuss our observations, data reduction, and the science we have and hope to accomplish with our observations in Chapter 4.

2.0 AN UNBIASED METHOD OF MODELING THE LOCAL PECULIAR VELOCITY FIELD WITH TYPE IA SUPERNOVAE

We apply statistically rigorous methods of non-parametric risk estimation to the problem of inferring the local peculiar velocity field from nearby SNe Ia. We use two non-parametric methods - Weighted Least Squares (WLS) and Coefficient Unbiased (CU) - both of which employ spherical harmonics to model the field and use the estimated risk to determine at which multipole to truncate the series. We show that if the data are not drawn from a uniform distribution or if there is power beyond the maximum multipole in the regression, a bias is introduced on the coefficients using WLS. CU estimates the coefficients without this bias by including the sampling density making the coefficients more accurate but not necessarily modeling the velocity field more accurately. After applying non-parametric risk estimation to SN Ia data, we find that there are not enough data at this time to measure power beyond the dipole. The WLS Local Group bulk flow is moving at 538 ± 86 km s^{-1} towards $(l, b) = (258^\circ \pm 10^\circ, 36^\circ \pm 11^\circ)$ and the CU bulk flow is moving at 446 ± 101 km s^{-1} towards $(l, b) = (273^\circ \pm 11^\circ, 46^\circ \pm 8^\circ)$. We find that the magnitude and direction of these measurements are in agreement with each other and previous results in the literature.

2.1 INTRODUCTION

Inhomogeneities in the matter distribution of our universe perturb the motions of individual galaxies from the overall smooth Hubble expansion. These motions, called peculiar velocities, result from gravitational interactions with the spectrum of fluctuations in the matter-density and are therefore a direct probe of the distribution of dark matter. The peculiar velocity of

an object is influenced by matter on all scales and modeling the peculiar velocity field allows one to probe scales larger than the sample. Calculating the dipole moment of the peculiar velocity field, or bulk flow, is an example of a measurement which helps us investigate the density fluctuations on large scales. Fluctuations in density on many Mpc scales are well described by linear physics and can be used to probe the mass power spectrum while fluctuations on small scales become highly non-linear and difficult to model.

From an accurate measurement of the local peculiar velocity field we can infer the properties of the dark matter distribution. On scales $\sim$ 10 Mpc and greater we can use linear perturbation theory to estimate the bias free mass power spectrum directly from

$$U(\mathbf{r}) = \frac{H_0 \Omega_m^{0.6}}{4\pi} \int d^3\mathbf{r}' \frac{\delta_m(\mathbf{r}')(\mathbf{r}' - \mathbf{r})}{\mid \mathbf{r}' - \mathbf{r} \mid^3} \tag{2.1}$$

where $\delta_m(\mathbf{r})$ is the density contrast defined by $(\rho - \bar{\rho})/(\bar{\rho})$, $\bar{\rho}$ is the average density, and Ω_m is the matter density parameter (Peebles, 1993). In the past, measurements of the matter power spectrum using galaxy peculiar velocity catalogs consistently produced power spectra with large amplitudes (Zaroubi et al., 1997; Freudling et al., 1999; Zaroubi et al., 2001). A renewed interest in bulk flow measurements has recently produced power spectra with lower amplitudes, which is often characterized by σ_8, which are consistent with the *Wilkinson Microwave Anisotropy Probe* (Park & Park, 2006; Feldman & Watkins, 2008; Abate & Erdoğdu, 2009; Song et al., 2010; Lavaux et al., 2010) and some which challenge the ΛCDM cosmology (Kashlinsky et al., 2008; Watkins et al., 2009; Feldman et al., 2010; Macaulay et al., 2010).

Peculiar velocity measurements also enable one to measure the matter distribution independent of redshift surveys. This allows for comparison between the galaxy power spectrum and matter power spectrum to probe the bias parameter β which specifies how galaxies follow the total underlying matter distribution (Pike & Hudson, 2005; Park & Park, 2006; Davis et al., 2010a). In addition to measuring β, this comparison can also be used to test the validity of the treatment of bias as a linear scaling (Abate et al., 2008).

By accurately measuring the local velocity field, it is possible to limit its effects on derived cosmological parameters (Cooray & Caldwell, 2006; Hui & Greene, 2006; Gordon et al., 2007; Neill et al., 2007; Davis et al., 2010b). The basic cosmological utility of SNe Ia comes

from comparing an inferred luminosity distance with a measured redshift. This redshift is assumed to be from cosmic expansion. However, on smaller physical scales where large scale structure induces peculiar velocities that create large fluctuations in redshift, this measured redshift becomes a combination of cosmic expansion and local bulk motion and thus of limited utility in inferring cosmological parameters from the corresponding luminosity distance. While traditionally this troublesome regime has been viewed to extend out to $z < 0.05$, recent work has shown significant effects out to $z < 0.1$ (Cooray & Caldwell, 2006; Hui & Greene, 2006). Hence peculiar velocities from SNe Ia add scatter to the Hubble diagram in the nearby redshift regime which adds uncertainty to derived cosmological parameters, including the dark energy equation-of-state parameter. In an ongoing effort to probe the nature of dark energy, surveys such as the CfA Supernova Group[1] (Hicken et al., 2009b), SNLS[2] (Astier et al., 2006), Pan-STARRS[3], ESSENCE[4] (Miknaitis et al., 2007), Carnegie Supernova Project (CSP) [5] (Hamuy et al., 2006; Folatelli et al., 2010), the Lick Observatory Supernova Search KAIT/LOSS (Filippenko et al., 2001; Leaman et al., 2010), Nearby SN Factory[6] (Aldering et al., 2002), SkyMapper[7] (Murphy et al., 2009), Palomar Transient Factory[8] (Law et al., 2009) hope to obtain tighter constraints on cosmological parameters. With the future influx of SN Ia data, statistical errors will be reduced but an understanding of systematic errors is required to make improvements on cosmological measurements (Albrecht et al., 2006a). Averaging over many SN Ia reduces scatter caused by random motions but not those caused by coherent large scale motions. One expects these bulk motions to converge to zero with increasing volume in the rest frame of the cosmic microwave background (CMB) with the rate of convergence depending on the amplitude of the matter perturbations. This fact motivates determining both the monopole and dipole component of the local peculiar velocity field (Zaroubi, 2002).

To model the local peculiar velocity field or flow field requires a measure of an object's

[1] http://www.cfa.harvard.edu/supernova/SNgroup.html
[2] http://cfht.hawaii.edu/SNLS/
[3] http://pan-starrs.ifa.hawaii.edu/public/
[4] http://www.ctio.noao.edu/essence/
[5] http://csp1.lco.cl/~cspuser1/PUB/CSP.html
[6] http://snfactory.lbl.gov/
[7] http://www.mso.anu.edu.au/skymapper/
[8] http://www.astro.caltech.edu/ptf/

peculiar velocity and its position on the sky. The peculiar velocity of an object, such as a galaxy or SN Ia, given the redshift z and cosmological distance d is

$$U = H_0 d_l(z) - H_0 d \tag{2.2}$$

where H_0 is the Hubble parameter and $H_0 d_l(z)$ is the recessional velocity described by

$$H_0\, d_l(z) = c(1+z) \int_0^z \left[\Omega_M (1+z')^3 + \Omega_\Lambda\right]^{-1/2} dz'. \tag{2.3}$$

Redshifts to galaxies can be measured accurately with an error $\sigma_z \sim 0.001$. Therefore, the accuracy of a measure of an object's peculiar velocity rests on how well we can determine its distance.

A variety of techniques exist to determine d. Distances to spiral galaxies can be measured through the Tully-Fisher (TF) relation (Tully & Fisher, 1977) which finds a power law relationship between the luminosity and rotational velocity. This method has been one of the most successful in generating large peculiar velocity catalogs. The SFI++ data set (Masters et al., 2006; Springob et al., 2007) for example, is one of the largest homogeneously derived peculiar velocity catalog using I-band TF distances to ~ 5000 galaxies with $\sim 15\%$ distance errors. This catalog builds on the Spiral Field I-band (SFI; Giovanelli et al. (1994, 1995); da Costa et al. (1996); Haynes et al. (1999b,a)), Spiral Cluster I-band (SCI; Giovanelli et al. (1997b,a)) and the Spiral Cluster I-band 2 (SC2; Dale et al. (1999a,c)) catalogs. The Two Micron All-Sky Survey (2MASS) Tully-Fisher (2MTF) survey (Masters et al., 2008) aims to measure TF distances to all bright spirals in 2MASS in the J, H, and K bands. The Kinematics of the Local Universe catalog (KLUN)[9] (Theureau, 1998), which is the only catalog to exceed SFI++ in number of galaxies, consists of B-band TF distances to 6600 galaxies. The velocity widths in this catalog are not homogeneously collected and measured adding to the errors. Additionally, the B-band TF relationship exhibits more scatter – which translates to larger distance errors – than the I, J, H, and K bands due to Galactic and internal extinction, making the SFI++ arguably the best galaxy peculiar velocity catalog currently available. Finally, with the Square Kilometer Array (SKA) (Dewdney et al., 2009) we expect TF catalogs to grow out to larger distances using less HI in the near future. Using

[9] http://klun.obs-nancay.fr/

TF derived peculiar velocities, measurements of the bulk flow and shear moments have been made (Giovanelli et al., 1998; Dale et al., 1999b; Courteau et al., 2000; Kudrya et al., 2003; Feldman & Watkins, 2008; Kudrya et al., 2009; Nusser & Davis, 2011) and cosmological parameters have been constrained (da Costa et al., 1998; Freudling et al., 1999; Borgani et al., 2000; Branchini et al., 2001; Pike & Hudson, 2005; Masters et al., 2006; Park & Park, 2006; Abate & Erdoğdu, 2009; Davis et al., 2010a).

Fundamental Plane (FP) distances (Djorgovski & Davis, 1987) which express the luminosity of an elliptical galaxy as a power law function of its radius and velocity dispersion also enable one to generate large peculiar velocity catalogs. Several smaller data sets utilize this distance indicator. The Streaming Motions of Abell Clusters (SMAC) project (Smith et al., 2000; Hudson et al., 2001; Smith et al., 2001) is an all-sky FP survey of 699 galaxies with $\sim 20\%$ distance errors. The EFAR project (Wegner et al., 1996; Colless et al., 2001) studied 736 elliptical galaxies in clusters in two regions on the sky to improve distance estimates to 85 clusters. Larger FP programs include the NOAO Fundamental Plane Survey (Smith et al., 2004) which will provide FP measurements to $\sim$4000 early-type galaxies and the 6 Degree Field Galaxy Survey (6dFGS) (Wakamatsu et al., 2003; Jones et al., 2009); a southern sky survey which, in combination with 2MASS, hopes to deliver more than 10,000 peculiar velocities using near infrared FP distances. The increase in the number of objects makes this catalog competitive even though individual distance errors are greater than TF errors. The $D_n - \sigma$ relation is a reduced parameter version of FP with typical errors of $\sim 25\%$ (Dressler et al., 1987b). The Early-type NEARby galaxies (ENEAR) (da Costa et al., 2000b; Bernardi et al., 2002) project measured galaxy distances based on $D_N - \sigma$ and FP to 1359 and 1107 galaxies and the Mark III Catalog of Galaxy Peculiar Velocities (Willick et al., 1995, 1996, 1997) contains 3300 galaxies with estimated distances from TF and $D_n - \sigma$. Global features of large-scale motions (Dressler et al., 1987a; Hudson et al., 1999; Dekel et al., 1999; da Costa et al., 2000a; Hudson et al., 2004; Colless et al., 2001) and derived parameters have been measured using these catalogs (Davis et al., 1996; Park, 2000; Rauzy & Hendry, 2000; Zaroubi et al., 2001; Nusser et al., 2001; Hoffman et al., 2001).

Other distance measurements to galaxies are more difficult to make or not as precise. Tonry et al. (2001) report distances to 300 early type galaxies using Surface Brightness

Fluctuations (SBF) whose observations were obtained over a period of $\sim$ 10 years. This method measures the luminosity fluctuations in each pixel of a high signal-to-noise CCD image of a galaxy where the amplitude of these fluctuations is inversely proportional to the distance. A $\sim$ 5% distance uncertainty can be obtained under the best observing conditions (Tonry et al., 2000) making SBF a useful method for $cz < 4000$ km/s. Although it is difficult to create a large catalog of objects, Blakeslee et al. (1999) used SBF distances to put constraints on H_0 and β. Tip of the Red Giant Branch (TRGB) (Madore & Freedman, 1995) and Cepheid distances are challenging to obtain as one must have resolved stars which limits observations to the local Universe.

SNe Ia are ideal candidates to measure peculiar velocities because they have a standardizable brightness and thus accurate distances can be calculated with less than 7% uncertainty (e.g. Jha et al., 2007b). Only recently through the efforts like the CfA Supernova Group, LOSS, and CSP have there been enough nearby SNe Ia ($\sim$ 400) to make measurements of bulk flows. Measurements of the monopole, dipole, and quadrupole have been made which find dipole results compatible with the CMB dipole (Colin et al., 2010; Haugbølle et al., 2007; Jha et al., 2007b; Giovanelli et al., 1998; Riess et al., 1995). Measurements of the monopole as a function of redshift have been used to test for a local void (Zehavi et al., 1998; Jha et al., 2007b). SN Ia peculiar velocity measurements have also been used to put constraints on power spectrum parameters (Radburn-Smith et al., 2004a; Watkins & Feldman, 2007). Hannestad et al. (2008) forecast the precision with which we will be able to probe σ_8 with future surveys like LSST. Following up on Cooray & Caldwell (2006); Hui & Greene (2006), Gordon et al. (2008) and Davis et al. (2010b) investigated the effects of correlated errors when neighboring SN Ia peculiar velocities are caused by the same variations in the density field. Not accounting for these correlations underestimates the uncertainty as each new SN Ia measurement is not independent. Recent investigations in using near-infrared measurements of SNe Ia to measure distances have shown promise for better standard candle behavior and the potential for more accurate and precise distances to galaxies in the local Universe (Krisciunas et al., 2004b; Wood-Vasey et al., 2008b; Mandel et al., 2009).

A wide range of methods have been developed to model the local peculiar velocity field. Nusser & Davis (1995) present a method for deriving a smooth estimate of the peculiar

velocity field by minimizing the scatter of a linear inverse Tully-Fisher relation η where the magnitude of each galaxy is corrected by a peculiar velocity. The peculiar velocity field is modeled in terms of a set of orthogonal functions and the model parameters are then found by maximizing the likelihood function for measuring a set of observed η. This method was applied to the Mark III (Davis et al., 1996) and SFI (da Costa et al., 1998) catalogs. Several other methods have been developed and tested on e.g., SFI and Mark III catalogs to estimate the mass power spectrum and compare peculiar velocities to galaxy redshift surveys which utilize or compliment rigorous maximum likelihood techniques (Willick & Strauss, 1998; Freudling et al., 1999; Zaroubi et al., 1999; Hoffman & Zaroubi, 2000; Zaroubi et al., 2001; Branchini et al., 2001). Non-parametric models (Branchini et al., 1999) and orthogonal functions (Nusser & Davis, 1994; Fisher et al., 1995) have been implemented to recover the velocity field from galaxies in redshift space. Smoothing methods (Dekel et al., 1999; Hoffman et al., 2001) have also been used to tackle large random errors and systematic errors associated with nonuniform and sparse sampling. More recently, Watkins et al. (2009) introduce a method for calculating bulk flow moments which are comparable between surveys by weighting the velocities to give an estimate of the bulk flow of an idealized survey. The variance of the difference between the estimate and the actual flow is minimized. Nusser & Davis (2011) present ACE (All Space Constrained Estimate), a three dimensional peculiar velocity field constrained to match TF measurements which is used to reconstruct the bulk flow.

Comparisons between different SN Ia and galaxy surveys and methods show that measurements of the local velocity field are highly correlated and in agreement (Zaroubi, 2002; Hudson, 2003; Hudson et al., 2004; Radburn-Smith et al., 2004a; Pike & Hudson, 2005; Sarkar et al., 2007; Watkins & Feldman, 2007). However, peculiar velocity data sets which have recently been combined (namely Feldman et al. (2010), but Watkins et al. (2009) and Ma et al. (2010) also combine data sets) are in disagreement with Nusser & Davis (2011). Errors in distance measurements and the non-uniform sampling of objects across the sky due to the Galactic disk ($\sim$40% of the sky) aggravate the systematic errors (Zaroubi, 2002). These systematic errors cause inconsistencies among the different models and must be dealt with in a statistically sound fashion. Since the field is at a point where rough agreement

exists between the different methods, and modeling can be done with better precision as the amount of data continues to increase, it is time to investigate the systematic errors that limit our measurements.

In this paper we present a statistical framework that can be used to properly extract the available flow field from observations of nearby SNe Ia, while avoiding the historical pitfalls of incomplete sampling and over-interpretation of the data. In particular, we emphasize the distinction between finding a best overall model fit to the data and finding the best unbiased value of a particular coefficient or set of coefficients of the model, e.g., the direction and strength of a dipole term due to our local motion. The first task is to provide a framework for modeling the peculiar velocity field which adequately accounts for sampling bias due to survey sky coverage, galactic foregrounds, etc. These methods are discussed in Section 2.2. We then introduce risk estimation as a means of determining where to truncate a series of basis functions when modeling the local peculiar velocity field, e.g., should we fit a function out to a quadrupole term. Risk estimation is a way of evaluating the quality of an estimate of the peculiar velocity field as a function of l moment, whose minimum determines the optimal balance of the bias and variance. These methods are outlined in Section 2.3. In Section 2.4 and Section 2.5 we apply these methods to a simulated data set and SN Ia data pulled from recent literature and discuss our results. We then apply our methods to simulated data modeled after the actual data and examine their performance as we alter the direction of the dipole in Section 2.6. In Section 2.7 we conclude and present suggestions for future work.

2.2 NON-PARAMETRIC ANALYSIS OF A SCALAR FIELD

A peculiar velocity field at a given redshift can be written as

$$U_n = f(x_n) + \epsilon_n \tag{2.4}$$

where U_n is the observed peculiar velocity at position $x_n = (\theta_n, \phi_n)$ on the sky, ϵ_n is the observation error, and f is our peculiar velocity field. Since we expect f to be a smoothly

varying function across the sky, it can be decomposed as

$$f(x) = \sum_{j=0}^{\infty} \beta_j \phi_j(x) \tag{2.5}$$

where ϕ_j, $[j = 0, 1, 2...]$ forms an orthonormal basis and β_j is given by

$$\beta_j = \int \phi_j(x) f(x) dx. \tag{2.6}$$

In this work we apply the real spherical harmonic basis as we are physically interested in a measurement of the dipole and follow a procedure similar to Haugbølle et al. (2007). The radial velocity field on a spherical shell of a given redshift can be expanded using spherical harmonics:

$$f = \sum_{l=0}^{\infty} \sum_{m=-l}^{l} a_{lm} Y_{lm} \tag{2.7}$$

$$= \sum_{l=0}^{\infty} \left\{ \sum_{m=1}^{l} (a_{l,-m} Y_{l,-m} + a_{lm} Y_{lm}) + a_{l0} Y_{l0} \right\}. \tag{2.8}$$

Using $a_{l,-m} = (-1)^m a^*_{lm}$ and $Y_{l,-m} = (-1)^m Y^*_{lm}$ the expansion for the real radial velocity can be rewritten as

$$f = \sum_{l=0}^{\infty} \left\{ \sum_{m=1}^{l} [2\Re(a_{lm} Y_{lm})] + a_{l0} Y_{l0} \right\} \tag{2.9}$$

$$= \sum_{l=0}^{\infty} \left\{ \sum_{m=1}^{l} [2\Re(a_{lm})\Re(Y_{lm}) - 2\Im(a_{lm})\Im(Y_{lm})] + a_{l0} Y_{l0} \right\}. \tag{2.10}$$

Our real orthonormal basis is then $[Y_{l0}, \sqrt{2}\Re(Y_{lm}), -\sqrt{2}\Im(Y_{lm}), m = 1, ..., l]$.

We have peculiar velocity measurements for a finite number of positions on the sky and therefore cannot fit an infinite set of smooth functions. We estimate f[10] by

$$\widehat{f}(x) = \sum_{j=0}^{J} \beta_j \phi_j(x) \tag{2.11}$$

where J is a tuning parameter, more precisely the l^{th} moment that we fit out to. By introducing a tuning parameter our methods are non-parametric; we do not a priori decide where to truncate the series of spherical harmonics but allow the data to determine the tuning parameter. Our task is now to estimate β and determine J.

[10]Following statistical practice we denote an estimated quantity with a hat.

2.2.1 Weighted Least Squares Estimator

Consider an ideal case where the 2D peculiar velocity field can be represented *exactly* as a finite sum of spherical harmonics, plenty of uniformly distributed data are sampled, and the true J is chosen as a result. The Gauss-Markov theorem (see, e.g., Hastie et al. 2009) tells us that the best linear unbiased estimator with minimum variance for a linear model in which the errors have expectation zero and are uncorrelated is the weighted least squares (WLS) estimator. If we define Y_J as the $N \times J$ matrix

$$Y_J = \begin{bmatrix} \phi_0(x_1) & \phi_1(x_1) & \cdots & \phi_J(x_1) \\ \phi_0(x_2) & \phi_1(x_2) & \cdots & \phi_J(x_2) \\ \vdots & \vdots & \cdots & \cdots \\ \phi_0(x_N) & \phi_1(x_N) & \cdots & \phi_J(x_N) \end{bmatrix} \tag{2.12}$$

and the column vectors $\beta_J = (\beta_0, ..., \beta_J)$, $U = (U_1, ..., U_N)$ and $\epsilon = (\epsilon_1, ..., \epsilon_N)$ we can then write

$$U = Y_J \beta_J + \epsilon. \tag{2.13}$$

The WLS estimator, $\widehat{\beta_J}$, that minimizes the residual sums of squares is

$$\widehat{\beta}_J = (Y_J^T W Y_J)^{-1} Y_J^T W U \tag{2.14}$$

where the diagonal elements of W are equal to one over the variance and the off-diagonal elements are zero.

Any estimate for $\widehat{f}$ which truncates an infinite series of functions will produce the same overall bias on the peculiar velocity field, namely

$$f - \langle \widehat{f} \rangle = \sum_{j=J+1}^{\infty} \beta_j \phi_j \tag{2.15}$$

where "$\langle\ \rangle$" denotes the ensemble expectation value. However, in the case we are considering there is no power at multipoles beyond $j = J$ so this bias will go to zero.

The estimates of the coefficients $\widehat{\beta}_J$ are also unbiased if the correct tuning parameter is chosen. If Y_∞ and β_∞ are defined over the range $[J+1, \infty)$ then the bias on $\widehat{\beta}_J$ (Appendix A.1)

$$\beta_J - \langle \widehat{\beta}_J \rangle = \left\langle (Y_J^T W Y_J)^{-1} Y_J^T W (Y_\infty \beta_\infty) \right\rangle \tag{2.16}$$

is a function of all the β's beyond the tuning parameter, i.e., the lower-order modes are contaminated by power at higher l's. For this case there is no power at multipoles beyond $j = J$, $\beta_\infty = 0$ and our coefficients are unbiased.

2.2.2 Coefficient Unbiased Estimator

If our data are not well-sampled, i.e., not drawn from a uniform distribution, or if spherical harmonics are not a good representation of the true velocity field then it is possible that there will be power beyond the best tuning parameter. This does not indicate a failure in determining the tuning parameter via risk (see Section 2.3) but is a consequence of the data.

Ideally we would like to obtain the unbiased coefficients because we tie physical meaning to the monopole and dipole. Suppose our data set x is sampled according to a sampling density $h(x)$ which quantifies how likely one is to sample a point at a given position on the sky, then

$$\begin{aligned}
\left\langle \frac{U\phi_j(x)}{h(x)} \right\rangle &= \left\langle \frac{(f(x)+\epsilon)\phi_j(x)}{h(x)} \right\rangle && (2.17)\\
&= \left\langle \frac{f(x)\phi_j(x)}{h(x)} \right\rangle && (2.18)\\
&= \int \frac{f(x)\phi_j(x)}{h(x)} h(x)dx && (2.19)\\
&= \beta_j. && (2.20)
\end{aligned}$$

A weighted unbiased estimate of β_j is therefore (see Appendix A.2)

$$\widehat{\beta}_j^* = \frac{\sum_{n=1}^{N} \frac{U_n\phi_j(x_n)}{h(x_n)\sigma_n^2}}{\sum_{n=1}^{N} \frac{1}{\sigma_n^2}} \tag{2.21}$$

where σ_n is the uncertainty on the peculiar velocity. We will call this our coefficient-unbiased (CU) estimate, $\widehat{\beta}_j^*$.

Although the CU estimate is unbiased, its accuracy depends on the sampling density. The sampling density in most cases is unknown and must be estimated from the data.

2.2.2.1 Estimating h(x) The sampling density is a normalized scalar field which can be modeled several ways. We outline the process using orthonormal basis functions and will continue to use the real spherical harmonic basis, ϕ. We decompose h as

$$h(x) = \sum_{i=0}^{\infty} \alpha_i \phi_i(x) \simeq \sum_{i=0}^{I} Z_i \phi_i(x) \tag{2.22}$$

where I is the tuning parameter. We estimate α_i by

$$Z_i = \frac{1}{N} \sum_{n=1}^{N} \phi_i(x_n) \tag{2.23}$$

since

$$\langle Z_i \rangle = \int \phi_i(x) h(x) dx = \alpha_i. \tag{2.24}$$

It is difficult to create a normalized positive scalar field using a truncated set of orthogonal functions. In practice there may be patches on the sky which have negative $\widehat{h}$. Since a negative sampling density has no physical meaning, we set all negative regions to zero, add a small constant offset component to the sampling density and renormalize. This will prevent division by zero when a data point lies in a negative $\widehat{h}$ region. This procedure adds a small bias but is a standard practice when using orthogonal functions and small data sets (see, e.g., Efromovich 1999).

Is a spherical harmonic decomposition of the sampling density appropriate? While using an orthogonal basis is desirable, the choice of spherical harmonics to model a patchy sampling density is clearly non-ideal. Smoothing the data with a Gaussian kernel or using a wavelet decomposition to model h would be a good alternative, especially when the distribution of data are sparse or if there are large empty regions of space. We merely present the formalism to determine h with orthonormal functions and encourage astronomers to use sampling density estimation with any basis set.

2.3 DETERMINING TUNING PARAMETER VIA RISK ESTIMATION

Recall that the tuning parameter determines at which l moment to truncate the series of spherical harmonics. We determine this value by minimizing the estimated risk. The risk is a way of evaluating the quality of a non-parametric estimator by balancing the bias and variance (Appendix A.3) which determines the complexity of the function we fit to the data. If the bias is large and the variance is small, the function will be too simple, under-fitting the data. This would be analogous to only using a monopole term when there is power at higher l. If the opposite is true, the data are over-fitted, similar to fitting many spherical harmonics in order to describe noisy data.

2.3.1 Risk Estimation for WLS

Recall the estimated peculiar velocity field

$$\widehat{f} = Y_J \widehat{\beta}_J \equiv LU \tag{2.25}$$

where we introduce the smoothing matrix L

$$L = Y_J (Y_J^T W Y_J)^{-1} Y_J^T W. \tag{2.26}$$

Note that the n^{th} row of the smoothing matrix is the effective kernel for estimating $f(x_n)$. The risk is the integrated mean squared error

$$R(J) = \left\langle \frac{1}{N} \sum_{n=1}^{N} (f(x_n) - \widehat{f}(x_n))^2 \right\rangle \tag{2.27}$$

and can be estimated by the leave-one-out cross-validation score

$$\widehat{R}(J) = \frac{1}{N} \sum_{n=1}^{N} (U_n - \widehat{f}_{(-n)}(x_n))^2 \tag{2.28}$$

where $\widehat{f}_{(-n)}$ is the estimated function obtained by leaving out the n^{th} data point (see, e.g., Wasserman 2006a). For a linear smoother in which $\widehat{f}$ can be written as a linear sum of functions, the estimated risk can be written in a less computationally expensive form

$$\widehat{R}(J) = \frac{1}{N}\sum_{n=1}^{N}\left(\frac{U_n - \widehat{f}(x_n)}{1 - L_{nn}}\right)^2 \tag{2.29}$$

where L_{nn} are the diagonal elements of the smoothing matrix.

There are a few important things to note. First, the risk gives the best tuning parameter to use in order to model the entire function, e.g., the peculiar velocity field over the entire sky for a given set of data. This is different than claiming the most accurate component of the field, e.g., the best measurement of the dipole. Secondly, the accuracy to which Equation 2.29 estimates the risk depends on the number of data points used and will be better estimated with larger data sets. Finally, the value of the estimated risk changes for different data sets. What is important for comparison are the relative values of the risk for different tuning parameters. Although not explored in this paper, one can also use the estimated risk to compare bases with which one could model the peculiar velocity field.

2.3.2 Risk Estimation for CU

We start by calculating the variance and bias on h. The variance on $\widehat{h}$ is the estimated variance on the coefficients Z_i given by

$$\widehat{\sigma}_i^2 = \frac{1}{N^2}\sum_{n=1}^{N}(\phi_i(x_n) - Z_i)^2. \tag{2.30}$$

The bias on h by definition is

$$h - \langle\widehat{h}\rangle = \sum_{i=I+1}^{\infty}\alpha_i\phi_i. \tag{2.31}$$

We can only calculate the bias out to the maximum number of independent basis functions, L, less than the number of data points. For spherical harmonics, this is given by

$$\sum_{l=0}^{L} 2l + 1 \leq N. \tag{2.32}$$

The risk of the estimator is then the variance plus the bias squared

$$\widehat{R}(I) = \sum_{i=0}^{I} \widehat{\sigma}_i^2 + \sum_{i=I+1}^{L} (Z_i^2 - \widehat{\sigma}_i^2)_+ \tag{2.33}$$

where we have used Equation 2.30 to replace the bias squared α_i^2 with $Z_i^2 - \widehat{\sigma}_i^2$ and $+$ denotes only the positive values.

Estimating the risk for CU is similar to WLS using Equation 2.29. $\widehat{f}(x_i)$ must now be calculated with the unbiased coefficients $\widehat{\beta}_j^*$ and the diagonal elements of the smoothing matrix L_{nn} (see Appendix A.4) are

$$L_{nn} = \frac{\displaystyle\sum_{j=0}^{J} \frac{\phi_j^2(x_n)}{\widehat{h}(x_n)\sigma_n^2}}{\displaystyle\sum_{n=1}^{N} \frac{1}{\sigma_n^2}}. \tag{2.34}$$

2.4 APPLICATION TO SIMULATED DATA

To compare WLS and CU we created a simulated data set with a non-uniform distribution and a known 2D peculiar velocity field. We discuss how the data set is created followed by an application of each regression method and a discussion comparing the methods.

2.4.1 Simulated Data

We built the data set with a non-uniform h using rejection sampling. To do this we start with a uniform distribution of points over the entire sky and evaluate a non-uniform sampling density at each point according to

$$h = NY_{20+} \tag{2.35}$$

where N is a normalization factor and $+$ indicates only positive values. This has the effect of "masking" a region of the sky. We then choose the 1000 most likely points given some random "accept" parameter. If the accept value is less then the sampling density value, that

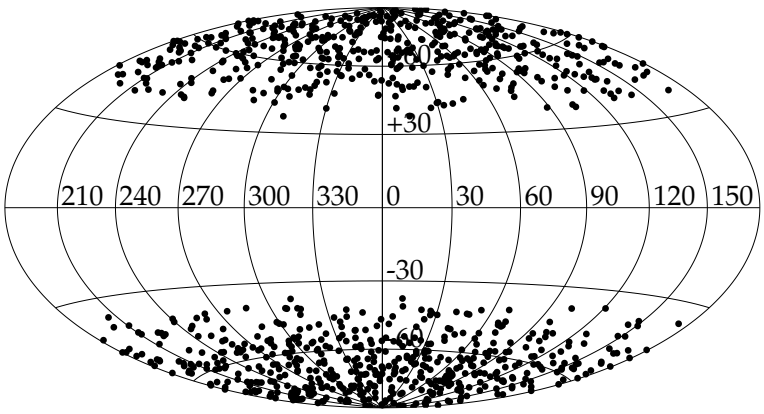

Figure 4 2D distribution of 1000 simulated data points. All plots are in galactic coordinates. The distribution was created from the sampling density $h = NY_{20+}$ where N is a normalization factor and $+$ indicates positive values. All negative values in the sampling density are set to zero. Although this h is not physical, the large empty galactic plane is ideal for testing the methods.

point is selected. A typical distribution of data points is shown in Figure 4. This pathological sampling density provides a useful demonstration of the methods.

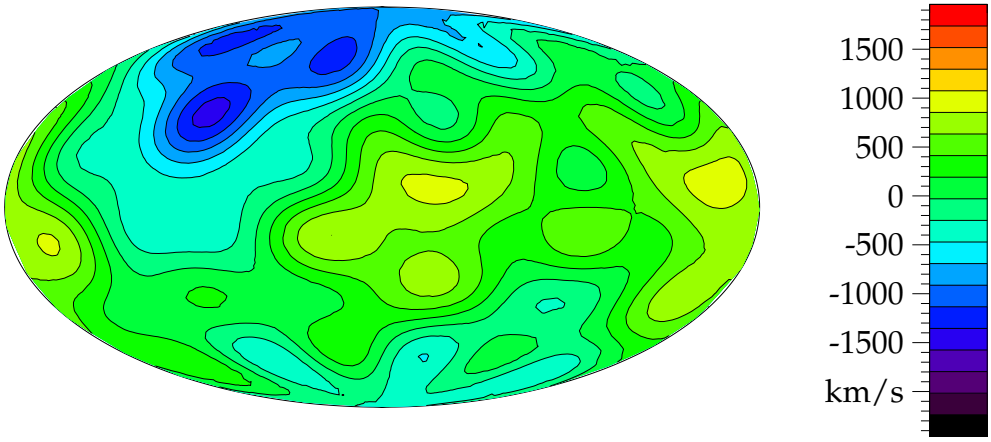

Figure 5 2D simulated peculiar velocity field in km/s, described by Equation 2.36.

The simulated real 2D peculiar velocity field is described by

$$\begin{aligned} V &= 180Y_{00} - 642Y_{10} - 1000Y_{20} + \Re(-38Y_{11} + 1061Y_{22} + 150Y_{86} + 300Y_{76}) \\ &\quad -\Im(1146Y_{11} + 849Y_{21} + 707Y_{83}) \end{aligned} \tag{2.36}$$

and is shown in Figure 5. We assign an error to each data point of 350 km s^{-1} and Gaussian scatter the peculiar velocity appropriately. This error includes the error on the measurement of the magnitude, σ_μ, the redshift error, σ_z, and a thermal component of $\sigma_v = 300$ km s^{-1} attributed to local motions of the SN Ia (Jha et al., 2007b).

2.4.2 Recovered Peculiar Velocity Field from WLS

To model the peculiar velocity field with non-parametric WLS methods we first determine the tuning parameter from the estimated risk. The risk is plotted in Figure 6 as the solid black line. In all estimated risk curves we determine the minimum by adding the error to the minimum risk and choosing the left-most l less than this value, i.e., we choose the simplest model within the errors. The minimum is at $l = 6$; as there is power beyond this multipole (see Equation 2.36), we know the coefficient estimator will be biased.

The results from WLS are in the left column in Figure 7. The effects of the bias are clearly evident. Artifacts appear in the galactic plane where we are not constrained by any data and are not accounted for by the standard deviation; it is not wide enough or deep enough. To determine if the power in the galactic plane is a consequence of a specific data set, we perform 100 different realizations of the data. If the artifacts are a function of a specific data set, we would expect after doing many realizations that the combined results, plotted on the right side in Figure 7, would recover the true velocity field or that the standard deviation would be large enough to account for any discrepancies. The plots in the right column demonstrate that this is not merely a result of one realization of the data, but a result of the underlying sampling density and power beyond the tuning parameter.

For comparison, we force the tuning parameter to be $l = 8$ and perform the same analysis in Figure 8. We confirm that there is no bias, even if the sampling density is non-uniform. WLS now recovers the entire velocity field well and has a standard deviation large enough

to account for any power fit in the galactic plane. By combining many realizations (right) we see the anomalous power in the galactic plane average out, doing a remarkable job of recovering the true velocity field.

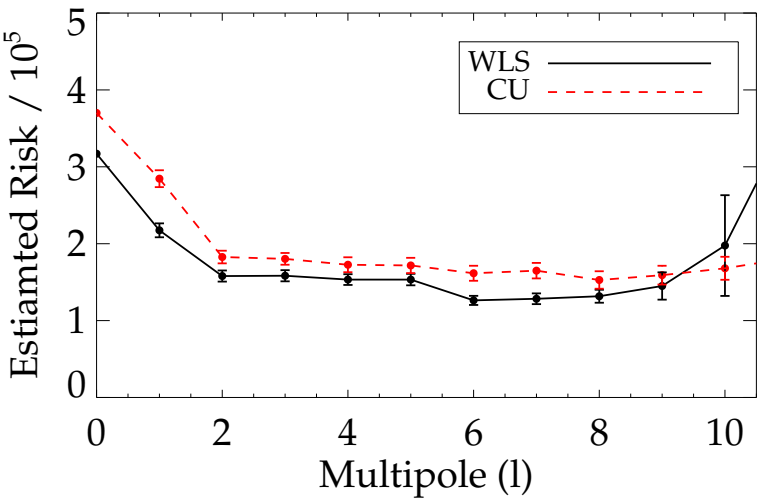

Figure 6 Estimated risk for WLS (black-solid) and CU (red-dashed). The estimated risk for a single l is the median value from a distribution of 1000 bootstraps. As l increases, the distribution becomes skewed and the estimated risk becomes unstable. We choose the median to be robust against outliers. This is crucial for CU as choosing many points with small sampling density in the bootstrap can make the risk very large. The error on the estimated risk is the interquartile range (IQR) divided by 1.35 such that at low l when the distribution is normal, the IQR reduces to the standard deviation. To determine the minimum l in all estimated risk curves we choose the simplest model by finding the minimum, adding the error to the minimum, and choosing the left-most l less than this value. The minima occur at $l = 6$ for WLS and $l = 8$ for CU. There is power beyond the tuning parameter for WLS and so there is a bias on the coefficients. However, the minimum risk is lower for WLS than CU indicating that our estimate of $f(x)$ is more accurate using WLS.

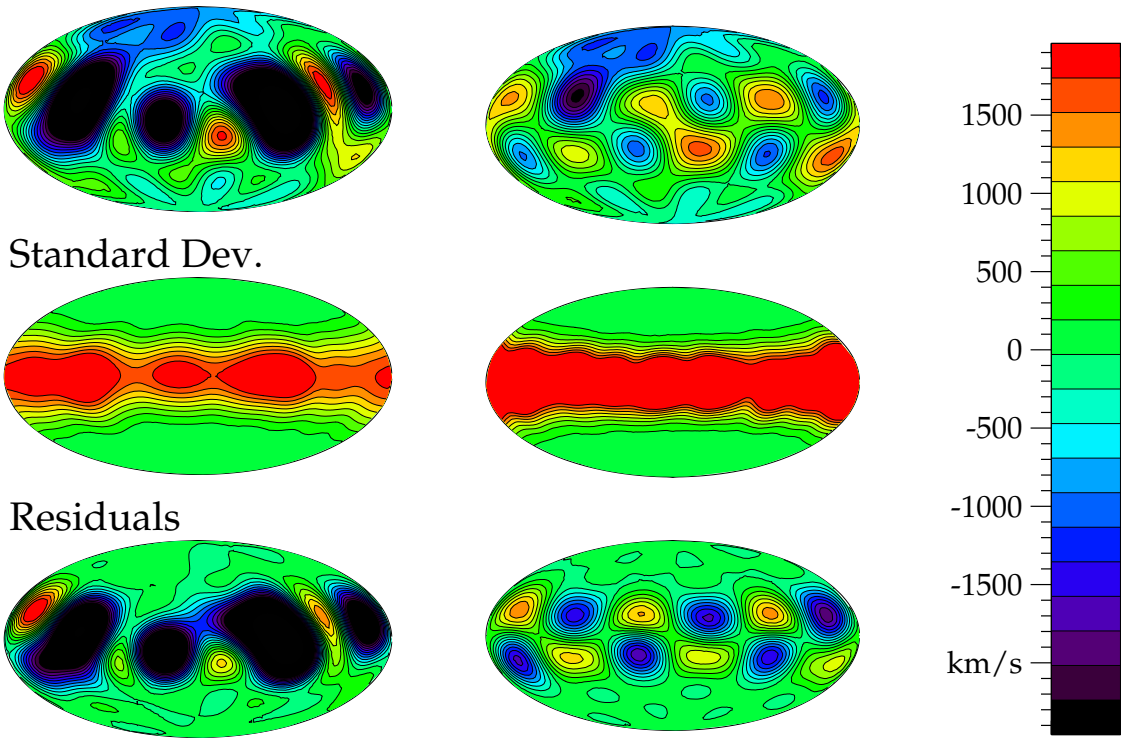

Figure 7 Recovered velocity field (top), standard deviation (middle), and residuals (bottom) in km s^{-1} for WLS for one realization of the data (left) and the combined results of 100 realizations of the data (right). The left plots were generated by bootstrapping a single data set 1000 times using the tuning parameter $J = 6$. We calculate the velocity for a set of 10,000 points distributed across the sky based on the derived a_{lm} coefficients for each bootstrap. These were averaged to create a contour plot of the peculiar velocity field (top) and standard deviation (middle). Finally, to create the residual plot, we took the difference between the averaged peculiar velocity at each point and the peculiar velocity calculated from Equation 2.36. We perform the same analysis but combine the results of 100 realizations of the data on the right. It is clear that the power in the galactic plane is not merely a function of one data set but a result of power beyond the tuning parameter and the underlying sampling density.

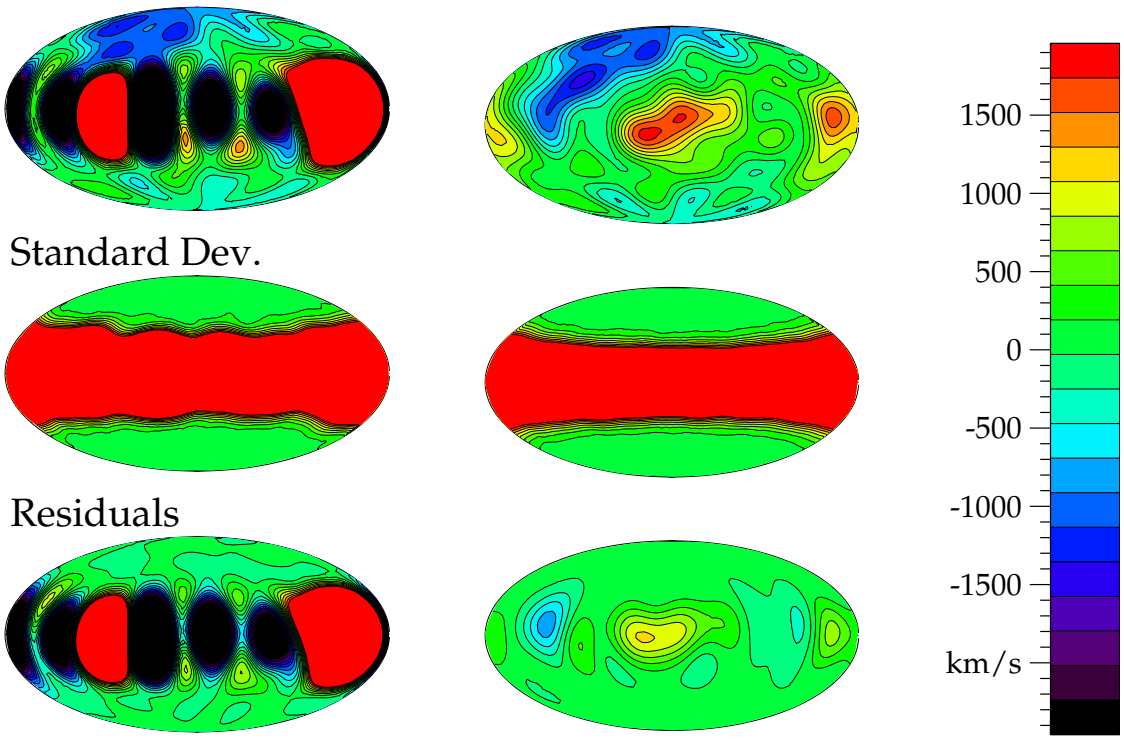

Figure 8 Results for WLS forcing the tuning parameter to be $J = 8$ created in an identical manner to the plots presented in Figure 7. We see that for one realization of the data the standard deviation is sufficient to account for all of the power in the galactic plane which is not real. The combined results from 100 realizations of the data (right) show the artifacts in the galactic plane do go away, confirming that they are due to the bias on the coefficients as a result of power beyond the tuning parameter in Figure 7.

2.4.3 Recovered Peculiar Velocity Field from CU

Removing the bias on the coefficients requires reconstructing the sampling density from the data. The estimated risk for the sampling density is shown in Figure 9 with a minimum at $l = 4$. Using this tuning parameter we reconstruct the sampling density according to §2.2.2.1. A contour plot of the sampling density is plotted in the top of Figure 10 with the data points overlaid as black circles. To investigate how well h is estimated, we combine the sampling density from 100 realizations of the data and calculate the mean (middle) and standard deviation (bottom) in Figure 10. The standard deviation is about a factor of 20

smaller than the sampling density and so the sampling density is well recovered using 1000 data points.

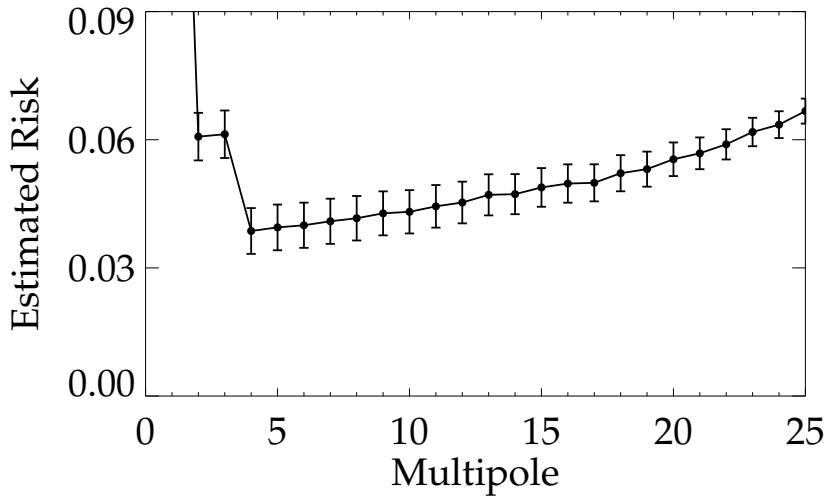

Figure 9 Estimated risk for the sampling density with a minimum at $l = 4$. It is difficult to estimate the mean and standard deviation of the risk for the sampling density via bootstrapping because duplicates and removing points will change the inherent distribution of the data. We therefore must use the entire data set to estimate the risk. This is in contrast to Figure 6, where we take the median of 1000 bootstrap resamples. The errors are estimated by dividing the data into two equal subsets, using one to calculate Z_i and the other to calculate the estimated risk. This is done 500 times. The estimated errors are then the standard deviation at each l scaled by $1/2$ due to the decrease in the number of points used to estimate the risk.

Having found the sampling density, we estimate the risk for CU as we did for WLS. These results are shown in Figure 6 (red-dashed) with a minimum at $l = 8$. Note that the estimated risk at $l = 6$ for WLS is lower than at $l = 8$ for CU. From this we expect WLS to be more accurate modeling $f(x)$ where we have data even though there is a bias on the coefficients.

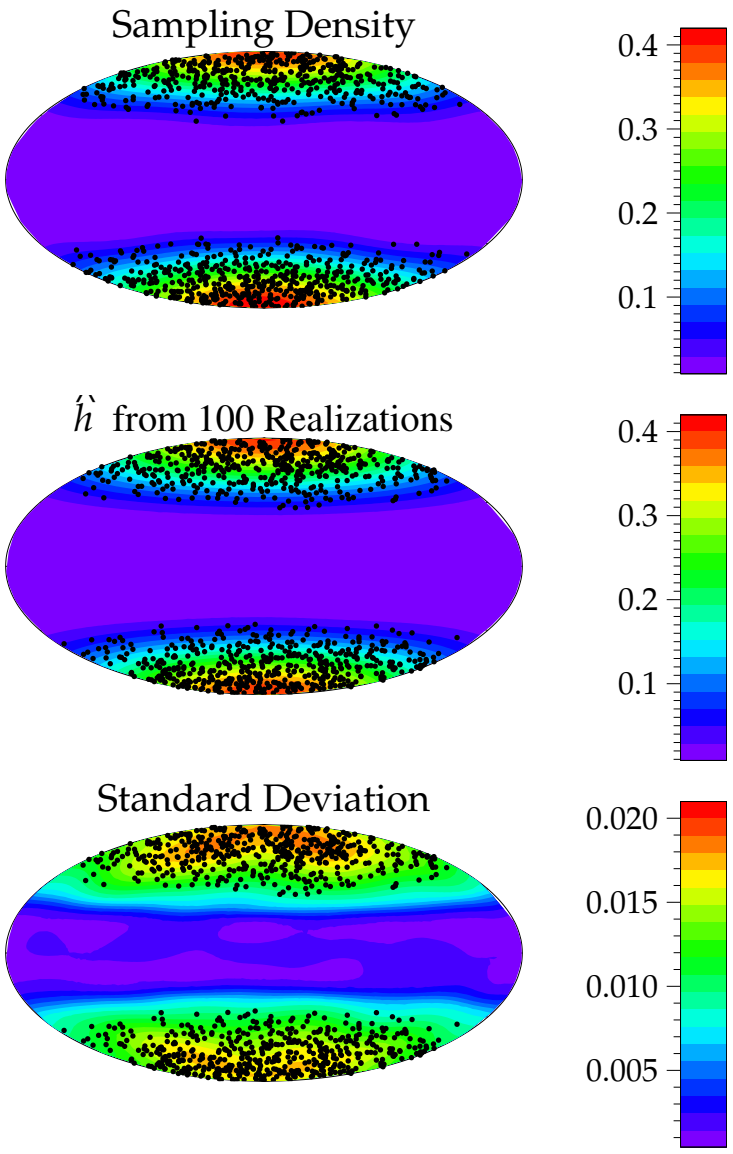

Figure 10 Typical recovered sampling density for one realization of the data using the tuning parameter $I = 4$ (top). Over-plotted are the simulated data points. To ensure a positive definite sampling density, we calculate h according to Equation 2.22, set all negative values to zero, add a small constant to the entire field, and then renormalize. The mean (middle) and standard deviation (bottom) of the sampling density are plotted for 100 different realizations. For each realization, the sampling density was calculated using the best tuning parameter for that data set. Over-plotted are the simulated data points from one realization. The standard deviation is roughly factor of 20 lower and so h is well estimated using 1000 data points.

The results for CU using $J = 8$ are plotted in Figure 11. CU does not allow power to be fit in regions where there are few data points by accounting for the underlying distribution of the data. The standard deviation also accounts for most of the discrepancies seen in the residual plot. We also find this method to be robust against the choice of tuning parameter. In Figure 12 we force the tuning parameter to be $J = 6$ and still do not see any artifacts in the galactic plane, although we have sacrificed some in overall accuracy. This is expected since the estimated risk is larger at $J = 6$.

In Figure 13 we show distributions of the residuals for each method using the tuning parameters $J_{\text{WLS}} = 6$ and $J_{\text{CU}} = 8$. On the top row are the residuals defined as the difference between the velocity obtained from the regression $\widehat{f}(x)$ and the velocity V given by Equation 2.36. These plots tell us how well the method is recovering the true underlying velocity field. On the bottom, the residuals are the difference between $\widehat{f}(x)$ and the velocity scattered values V_{scat}. These plots tell us how well the method is fitting simulated data. The narrower spread in WLS in the top plots tell us it is estimating the velocity field more accurately where we have sampled. We expect this result because the risk for WLS is lower than for CU. Both models are fitting the simulated data similarly and have comparable spreads in their distribution (bottom plots).

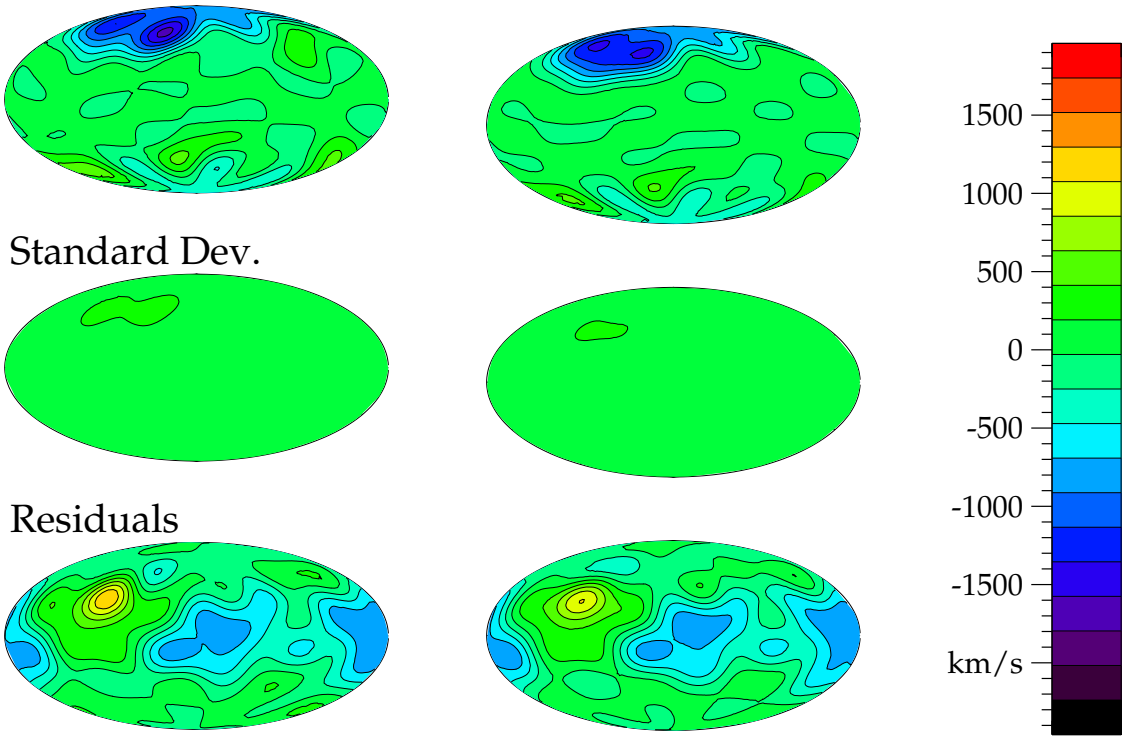

Figure 11 Recovered velocity field (top), standard deviation (middle), and residuals (bottom) in km s^{-1} for CU for one realization of the data (left) and the combined results of 100 realizations of the data (right). These were generated in an identical manner as those in Figure 7. By weighting by the sampling density, CU does not allow for any power in the galactic plane where there are no constraining data.

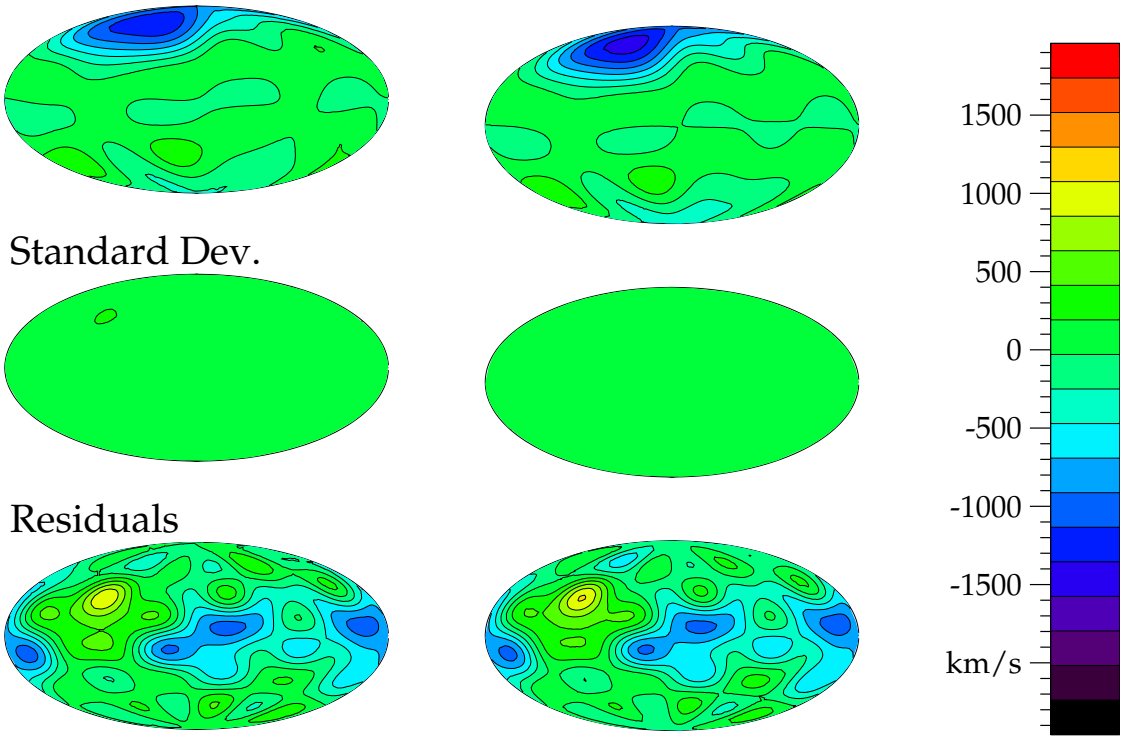

Figure 12 Results for CU forcing the tuning parameter to be $J = 6$. These were generated in an identical manner as those in Figure 8. The CU method is more robust to our choice of tuning parameter. There is power beyond $l = 6$ but it is not biasing our coefficients as it did for WLS (Figure 7).

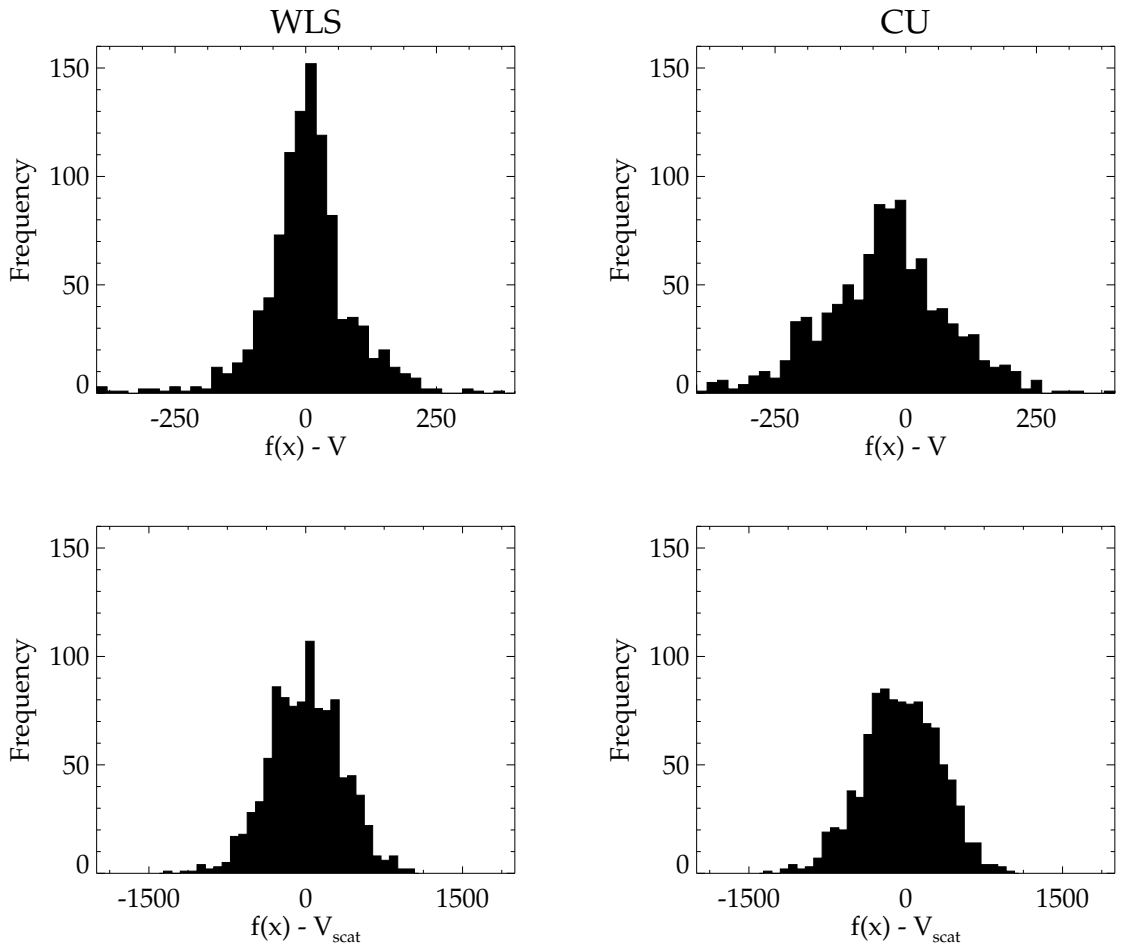

Figure 13 Distributions of the residuals for each method using the tuning parameters $J_{\text{WLS}} = 6$ and $J_{\text{CU}} = 8$. On the top row are the residuals calculated from the difference between the velocity obtained in the regression $\widehat{f}(x)$, and the velocity V given by Equation 2.36. On the bottom, the residuals are the difference between $\widehat{f}(x)$ and the velocity scattered values V_{scat}. The bottom plots show us how well our methods are fitting the data. The top plots show us how well we are recovering the true underlying peculiar velocity field where we have data. We see that WLS models the true velocity field better as evidenced by the narrower spread in the distribution but that both methods fit the "data" equally well.

2.5 APPLICATION TO OBSERVED SN IA DATA

With our framework established and tested, we now analyze SN Ia data. We introduce the data set, apply each regression method, and present a comparison of the two methods.

2.5.1 SN Ia Data

Our data consist of SNe Ia published in Hicken et al. (2009b) (hereafter H09a); Jha et al. (2007b); Hamuy et al. (1996); Riess et al. (1999) using the distance measurements published in Hicken et al. (2009a) (hereafter H09b). Not all of the SNe Ia published in H09a have distance measurements published in H09b. The rest were obtained from private communication with the author. We use their results from the Multicolor Light Curve Shape method (MLCS2k2) (Jha et al., 2007b) with an $R_V = 1.7$ extinction law. The positions of the SNe Ia are publicly available.[11] H09b provide the redshift and distance modulus μ with an assumed absolute magnitude of $M_V = -19.504$. The peculiar velocity, U, is calculated according to (see Jha et al. 2007b)

$$U = H_0\, d_l(z) - H_0\, d_{\rm SN} \tag{2.37}$$

where $H_0 d_l(z)$ and $H_0 d_{\rm SN}$ are given by

$$H_0\, d_l(z) = c(1+z) \int_0^z \left[\Omega_M (1+z')^3 + \Omega_\lambda\right]^{-1/2} dz'. \tag{2.38}$$

$$H_0\, d_{\rm SN} = 65 \left[10^{0.2(\mu - 25)}\right] \tag{2.39}$$

Here z is the redshift in the rest frame of the Local Group[12] and we assume that $\Omega_M = 0.3$, $\Omega_\lambda = 0.7$, and $H_0 = 65$ km s^{-1} Mpc^{-1}. Our results are independent of the value we choose for H_0 as there is a degeneracy between H_0 and M_V. The error on the peculiar velocity is the quadrature sum of the error on μ, a recommended error of 0.078 mag (see H09b), σ_z, and a peculiar velocity error of $\sigma_v = 300$ km s^{-1} attributed to local motions of the SN Ia which are on scales smaller than those probed in this analysis (Jha et al., 2007b).

[11] http://www.cfa.harvard.edu/iau/lists/Supernovae.html
[12] http://nedwww.ipac.caltech.edu/help/velc_help.html

We eliminate objects which could not be fit by MLCS2k2, whose first observation occurs more than 20 days past maximum B-band light, or which showed evidence for excessive host galaxy extinction ($A_V < 2$). We choose one redshift shell for our analysis due to the relatively small number of objects and consider the same velocity range adopted by Jha et al. 2007b of 1500 km s^{-1} $\leq H_0 d_{\rm SN} \leq$ 7500 km s^{-1}. One object, SN 2004ap, has a particularly large peculiar velocity of 2864 km s^{-1}. Further examination reveals that this supernova, when modeled with MLCS2k2 with $R_V = 3.1$, has its first observation at 20 days past maximum B-band light. To be conservative, we exclude this object. This leaves us with 112 SNe Ia whose peculiar velocity information is recorded in Table 1. In this table we include all SNe Ia with $H_0 d_{\rm SN} \leq 7500$ km s^{-1} for completeness.

In Figure 14 we plot the distribution of the data. One can clearly see the dipole with significant concentrations of negative peculiar velocities around $(l, b) = (260°, 40°)$ and positive peculiar velocities around $(l, b) = (100°, -40°)$. As we will explore in future figures this dipole structure is consistent with the dipole in the temperature anisotropy of the CMB.

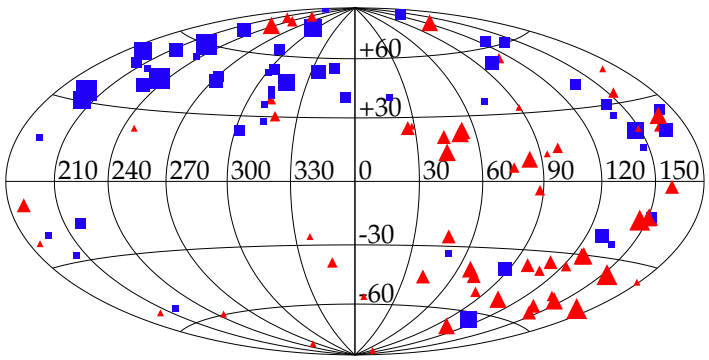

Figure 14 Sky distribution of 112 SNe Ia taken from Hicken et al. (2009b) in Galactic longitude and latitude. The velocity range considered is 1500 km s^{-1} $\leq H_0 d_{\rm SN} \leq$ 7500 km s^{-1} where $d_{\rm SN}$ is the luminosity distance. The color/shape of the points indicates positive (red-triangle) and negative (blue-square) peculiar velocities and the size corresponds to the magnitude of the peculiar velocity. From this figure one can clearly see a dipole signature between the upper-left and lower-right quadrants.

Table 1: SN Ia Data

Name	RA	Decl.[a]	z[b]	μ mag	A_V mag	U[c] km s^{-1}
1986G	13:25:36.51	-43:01:54.2	0.003	28.012±0.081	1.221±0.086	...
1990N	12:42:56.74	13:15:24.0	0.004	32.051±0.076	0.221±0.051	-793±557
1991bg	12:25:03.71	12:52:15.8	0.005	31.728±0.063	0.096±0.057	...
1991T	12:34:10.21	02:39:56.6	0.007	30.787±0.062	0.302±0.039	...
1992A	03:36:27.43	-34:57:31.5	0.006	31.540±0.072	0.014±0.014	...
1992ag	13:24:10.12	-23:52:39.3	0.026	35.213±0.118	0.312±0.081	224±612
1992al	20:45:56.49	-51:23:40.0	0.014	33.964±0.082	0.033±0.027	337±458
1992bc	03:05:17.28	-39:33:39.7	0.020	34.796±0.061	0.012±0.012	106±505
1992bo	01:21:58.44	-34:12:43.5	0.018	34.671±0.100	0.034±0.029	122±548
1993H	13:52:50.34	-30:42:23.3	0.025	35.078±0.102	0.029±0.026	353±556
1994ae	10:47:01.95	17:16:31.0	0.005	32.508±0.067	0.049±0.032	-872±541
1994D	12:34:02.45	07:42:04.7	0.003	30.916±0.068	0.009±0.009	...
1994M	12:31:08.61	00:36:19.9	0.024	35.228±0.104	0.080±0.055	-317±606
1994S	12:31:21.86	29:08:04.2	0.016	34.312±0.085	0.047±0.034	-190±491
1995ak	02:45:48.83	03:13:50.1	0.022	34.896±0.105	0.259±0.072	806±549
1995al	09:50:55.97	33:33:09.4	0.006	32.658±0.074	0.177±0.049	-748±542
1995bd	04:45:21.24	11:04:02.5	0.014	34.062±0.120	0.462±0.159	183±501
1995D	09:40:54.75	05:08:26.2	0.008	32.748±0.073	0.068±0.044	-513±439
1995E	07:51:56.75	73:00:34.6	0.012	33.888±0.092	1.460±0.064	-211±520
1996ai	13:10:58.13	37:03:35.4	0.004	31.605±0.083	3.134±0.056	...
1996bk	13:46:57.98	60:58:12.9	0.007	32.393±0.108	0.260±0.098	208±414
1996bo	01:48:22.80	11:31:15.8	0.016	34.305±0.096	0.626±0.071	674±492
1996X	13:18:01.13	-26:50:45.3	0.008	32.341±0.070	0.031±0.024	-80±359
1997bp	12:46:53.75	-11:38:33.2	0.009	32.923±0.068	0.479±0.048	-196±395

Continued on Next Page...

Table 1 – Continued

Name	RA	Decl.[a]	z[b]	μ mag	A_V mag	U[c] km s^{-1}
1997bq	10:17:05.33	73:23:02.1	0.009	33.483±0.102	0.380±0.055	-257±520
1997br	13:20:42.40	-22:02:12.3	0.008	32.467±0.067	0.549±0.054	-124±371
1997do	07:26:42.50	47:05:36.0	0.010	33.580±0.096	0.262±0.061	-263±496
1997dt	23:00:02.93	15:58:50.9	0.006	33.257±0.115	1.138±0.074	-445±702
1997E	06:47:38.10	74:29:51.0	0.013	34.102±0.090	0.085±0.051	-79±517
1997Y	12:45:31.40	54:44:17.0	0.017	34.550±0.096	0.096±0.050	-298±544
1998ab	12:48:47.24	41:55:28.3	0.028	35.268±0.088	0.268±0.047	1009±549
1998aq	11:56:26.00	55:07:38.8	0.004	31.909±0.054	0.011±0.011	-292±498
1998bp	17:54:50.71	18:19:49.3	0.010	33.175±0.065	0.025±0.020	545±412
1998bu	10:46:46.03	11:50:07.1	0.004	30.595±0.061	0.631±0.040	...
1998co	21:47:36.45	-13:10:42.3	0.017	34.476±0.119	0.123±0.087	548±543
1998de	00:48:06.88	27:37:28.5	0.016	34.464±0.063	0.142±0.061	225±519
1998dh	23:14:40.31	04:32:14.1	0.008	32.962±0.090	0.259±0.060	371±489
1998ec	06:53:06.11	50:02:22.1	0.020	34.468±0.084	0.041±0.036	1042±450
1998ef	01:03:26.87	32:14:12.4	0.017	34.095±0.104	0.068±0.050	1339±446
1998es	01:37:17.50	05:52:50.3	0.010	33.220±0.063	0.207±0.042	475±444
1998V	18:22:37.40	15:42:08.4	0.017	34.354±0.090	0.145±0.071	721±480
1999aa	08:27:42.03	21:29:14.8	0.015	34.426±0.052	0.025±0.021	-701±512
1999ac	16:07:15.01	07:58:20.4	0.010	33.320±0.068	0.244±0.042	-78±457
1999by	09:21:52.07	51:00:06.6	0.003	31.017±0.053	0.030±0.022	...
1999cl	12:31:56.01	14:25:35.3	0.009	30.945±0.079	2.198±0.066	...±...
1999cp	14:06:31.30	-05:26:49.0	0.010	33.441±0.108	0.057±0.045	-410±475
1999cw	00:20:01.46	-06:20:03.6	0.011	32.753±0.105	0.330±0.076	1599±322
1999da	17:35:22.96	60:48:49.3	0.013	33.926±0.067	0.066±0.049	136±488

Continued on Next Page...

Table 1 – Continued

Name	RA	Decl.[a]	z[b]	μ mag	A_V mag	U[c] km s^{-1}
1999dk	01:31:26.92	14:17:05.7	0.014	34.161±0.076	0.252±0.058	278±503
1999dq	02:33:59.68	20:58:30.4	0.014	33.705±0.062	0.299±0.051	893±411
1999ee	22:16:10.00	-36:50:39.7	0.011	33.571±0.058	0.643±0.041	130±476
1999ek	05:36:31.60	16:38:17.8	0.018	34.379±0.125	0.312±0.156	406±516
1999gd	08:38:24.61	25:45:33.1	0.019	34.970±0.102	0.842±0.066	-872±607
2000ca	13:35:22.98	-34:09:37.0	0.024	35.182±0.071	0.017±0.015	-98±537
2000cn	17:57:40.42	27:49:58.1	0.023	35.057±0.085	0.071±0.060	717±543
2000cx	01:24:46.15	09:30:30.9	0.007	32.554±0.067	0.006±0.005	446±444
2000dk	01:07:23.52	32:24:23.2	0.016	34.333±0.084	0.017±0.015	745±486
2000E	20:37:13.77	66:05:50.2	0.004	31.788±0.102	0.466±0.122	...
2000fa	07:15:29.88	23:25:42.4	0.022	34.987±0.104	0.287±0.056	-43±573
2001bf	18:01:33.99	26:15:02.3	0.015	34.059±0.086	0.170±0.068	737±452
2001bt	19:13:46.75	-59:17:22.8	0.014	34.025±0.089	0.426±0.063	158±468
2001cp	17:11:02.58	05:50:26.8	0.022	34.998±0.190	0.054±0.047	448±741
2001cz	12:47:30.17	-39:34:48.1	0.016	34.260±0.088	0.200±0.070	-237±475
2001el	03:44:30.57	-44:38:23.7	0.004	31.625±0.073	0.500±0.044	...
2001ep	04:57:00.26	-04:45:40.2	0.013	33.893±0.085	0.259±0.054	-67±478
2001fe	09:37:57.10	25:29:41.3	0.014	34.102±0.092	0.099±0.049	-349±490
2001fh	21:20:42.50	44:23:53.2	0.011	33.778±0.109	0.077±0.062	335±515
2001G	09:09:33.18	50:16:51.3	0.017	34.482±0.089	0.050±0.035	08±506
2001v	11:57:24.93	25:12:09.0	0.016	34.047±0.067	0.171±0.041	349±418
2002bo	10:18:06.51	21:49:41.7	0.005	32.185±0.077	0.908±0.050	-579±475
2002cd	20:23:34.42	58:20:47.4	0.010	33.605±0.110	1.026±0.132	04±544
2002cr	14:06:37.59	-05:26:21.9	0.010	33.458±0.085	0.122±0.063	-465±472

Continued on Next Page...

Table 1 – Continued

Name	RA	Decl.[a]	z[b]	μ mag	A_V mag	U[c] km s^{-1}
2002dj	13:13:00.34	-19:31:08.7	0.010	33.104±0.094	0.342±0.078	-93±401
2002do	19:56:12.88	40:26:10.8	0.015	34.340±0.110	0.034±0.034	336±539
2002dp	23:28:30.12	22:25:38.8	0.010	33.565±0.091	0.268±0.090	449±490
2002er	17:11:29.88	07:59:44.8	0.009	32.998±0.083	0.227±0.074	99±452
2002fk	03:22:05.71	-15:24:03.2	0.007	32.616±0.073	0.034±0.023	50±452
2002ha	20:47:18.58	00:18:45.6	0.013	34.013±0.086	0.042±0.032	450±490
2002he	08:19:58.83	62:49:13.2	0.025	35.250±0.131	0.031±0.026	317±662
2002hw	00:06:49.06	08:37:48.5	0.016	34.330±0.095	0.605±0.099	754±497
2002jy	01:21:16.27	40:29:55.3	0.020	35.188±0.079	0.103±0.056	-441±620
2002kf	06:37:15.31	49:51:10.2	0.020	34.978±0.089	0.030±0.025	-468±587
2003cg	10:14:15.97	03:28:02.5	0.005	31.745±0.085	2.209±0.053	...
2003du	14:34:35.80	59:20:03.8	0.007	33.041±0.062	0.032±0.022	-558±579
2003it	00:05:48.47	27:27:09.6	0.024	35.282±0.120	0.083±0.055	548±657
2003kf	06:04:35.42	-12:37:42.8	0.008	32.765±0.093	0.114±0.080	-267±447
2003W	09:46:49.48	16:02:37.6	0.021	34.867±0.077	0.330±0.050	-157±516
2004ap	10:05:43.81	10:16:17.1	0.025	34.093±0.174	0.375±0.088	...
2004bg	11:21:01.53	21:20:23.4	0.022	35.096±0.096	0.067±0.052	-553±588
2004fu	20:35:11.54	64:48:25.7	0.009	33.137±0.197	0.175±0.123	336±524
2005am	09:16:12.47	-16:18:16.0	0.009	32.556±0.097	0.037±0.033	161±337
2005cf	15:21:32.21	-07:24:47.5	0.007	32.582±0.079	0.208±0.070	-250±446
2005el	05:11:48.72	05:11:39.4	0.015	34.243±0.081	0.012±0.013	-156±501
2005hk	00:27:50.87	-01:11:52.5	0.012	34.505±0.070	0.810±0.044	-1093±672
2005kc	22:34:07.34	05:34:06.3	0.014	34.084±0.090	0.624±0.074	527±498
2005ke	03:35:04.35	-24:56:38.8	0.004	31.920±0.054	0.068±0.040	-194±500

Continued on Next Page...

Table 1 – Continued

Name	RA	Decl.[a]	z[b]	μ mag	A_V mag	U[c] km s^{-1}
2005ki	10:40:28.22	09:12:08.4	0.021	34.804±0.088	0.018±0.015	-138±519
2005ls	02:54:15.97	42:43:29.8	0.021	34.695±0.094	0.750±0.064	980±505
2005mz	03:19:49.88	41:30:18.6	0.017	34.298±0.087	0.266±0.089	796±468
2006ac	12:41:44.86	35:04:07.1	0.024	35.256±0.091	0.104±0.047	-360±599
2006ax	11:24:03.46	-12:17:29.2	0.018	34.594±0.067	0.038±0.029	-542±497
2006cm	21:20:17.46	-01:41:02.7	0.015	34.578±0.115	1.829±0.079	-199±607
2006cp	12:19:14.89	22:25:38.2	0.023	35.006±0.101	0.440±0.064	207±554
2006d	12:52:33.94	-09:46:30.8	0.010	33.027±0.089	0.076±0.042	-214±409
2006et	00:42:45.82	-23:33:30.4	0.021	35.065±0.112	0.328±0.074	172±614
2006eu	20:02:51.15	49:19:02.3	0.023	34.465±0.141	1.208±0.119	2423±492
2006h	03:26:01.49	40:41:42.5	0.014	34.259±0.084	0.287±0.125	-207±545
2006ke	05:52:37.38	66:49:00.5	0.017	34.984±0.128	1.006±0.203	-1068±698
2006kf	03:41:50.48	08:09:25.0	0.021	34.961±0.113	0.024±0.024	135±596
2006le	05:00:41.99	63:15:19.0	0.017	34.633±0.092	0.076±0.060	-03±545
2006lf	04:38:29.49	44:02:01.5	0.013	33.745±0.123	0.095±0.074	487±468
2006mp	17:12:00.20	46:33:20.8	0.023	35.259±0.104	0.166±0.068	-69±633
2006n	06:08:31.24	64:43:25.1	0.014	34.174±0.083	0.027±0.023	53±500
2006sr	00:03:35.02	23:11:46.2	0.023	35.280±0.098	0.085±0.053	305±624
2006td	01:58:15.76	36:20:57.7	0.015	34.464±0.136	0.171±0.079	-56±606
2006x	12:22:53.99	15:48:33.1	0.006	30.958±0.077	2.496±0.043	...
2007af	14:22:21.06	00:23:37.7	0.006	32.302±0.082	0.215±0.054	-303±433
2007au	07:11:46.11	49:51:13.4	0.020	34.624±0.081	0.049±0.039	667±479
2007bc	11:19:14.57	20:48:32.5	0.022	34.932±0.108	0.084±0.059	-64±564
2007bm	11:25:02.30	-09:47:53.8	0.007	32.382±0.101	0.975±0.073	-320±390

Continued on Next Page...

Table 1 – Continued

Name	RA	Decl.[a]	z[b]	μ mag	A_V mag	U[c] km s^{-1}
2007ca	13:31:05.81	-15:06:06.6	0.015	34.622±0.096	0.580±0.069	-1337±599
2007ci	11:45:45.85	19:46:13.9	0.019	34.290±0.090	0.074±0.063	690±434
2007cq	22:14:40.43	05:04:48.9	0.025	35.085±0.101	0.109±0.059	1399±558
2007s	10:00:31.26	04:24:26.2	0.014	34.222±0.074	0.833±0.054	-942±523
2008bf	12:04:02.90	20:14:42.6	0.025	35.174±0.078	0.102±0.049	271±535
2008L	03:17:16.65	41:22:57.6	0.019	34.392±0.193	0.036±0.033	1117±602

2.5.2 WLS and CU Regressions on SN Ia Data

The first step in estimating the field with CU is to calculate the sampling density. We follow the procedure described in §2.4.3 and plot the results in Figure 15. Choosing the simplest model gives us a tuning parameter of $I = 6$. The high l moment is necessary to describe the patchiness of the data distribution. The sampling density field is shown in Figure 16. While it should be unlikely that we sample many data points in regions with low sampling density, there are some regions of the sky where the sampling density is very low and we have a data point. This discrepancy, in combination with a relatively flat estimated risk function is an indication that there are likely better basis functions than spherical harmonics to use to estimate h. However, as discussed in §2.2.2.1 they will serve for the purposes of demonstrating our method.

[a]SN Ia RA and Dec [J2000] from http://www.cfa.harvard.edu/iau/lists/Supernovae.html

[b]Redshift in the rest frame of the Cosmic Microwave Background. We assume a redshift uncertainty of 0.001.

[c]Includes the error on μ, a recommended error of 0.078 mag (see H09), σ_z, and a peculiar velocity error of $\sigma_v = 300$ km s^{-1} due to local motions on scales smaller than those probed by this analysis.

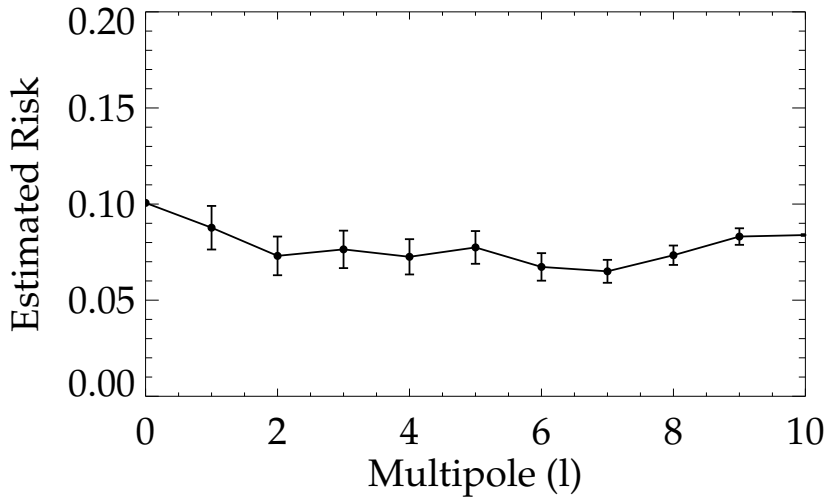

Figure 15 Estimated risk for sampling density with a minimum at $l = 6$ generated in a similar fashion to Figure 9. The high l moment results from the lumpiness in our sampling density.

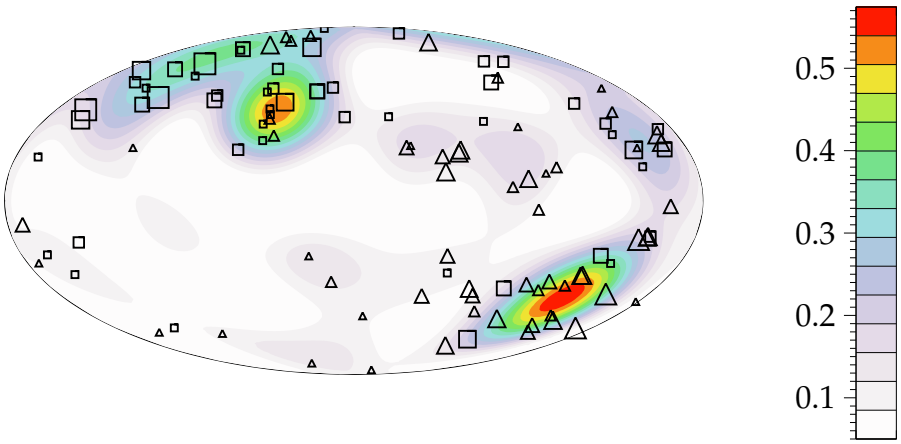

Figure 16 Recovered sampling density using $I = 6$ as the tuning parameter. After calculating h according to Equation 2.22, the negative values were set to zero, a small constant of 0.05 was added, and the sampling density was renormalized. Data points residing in low sampling density regions may be an indication that spherical harmonics are not the best way to decompose h. Same as Figure 2.5.1.

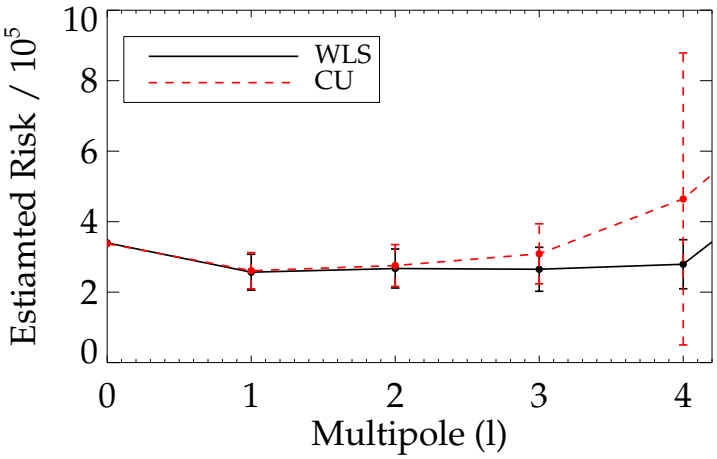

Figure 17 Estimated risk from the mean and standard deviation of 10,000 bootstraps as a function of l moment for WLS (solid-black) and CU (dashed-red) using 112 SNe Ia. We find the minimum to be at $l = 1$ for both methods, suggesting that the data are inadequate for detecting the quadrupole. We expect the velocity fields derived from CU and WLS to be consistent as indicated by the similar risk values.

Table 2. Summary of Results

WLS		CU	
Monopole	149±52 km s^{-1}	Monopole	98±45 km s^{-1}
Dipole	538±86 km s^{-1}	Dipole	446±101 km s^{-1}
Galactic l	258°±10°	Galactic l	273°±11°
Galactic b	36°±11°	Galactic b	46°±8°

The estimated risk for CU and WLS are plotted in Figure 17. We find the tuning parameter to be $J = 1$ for both methods and the risk values to be very similar. From this we expect that the two methods will be consistent and recover the velocity field with similar accuracy. The current SN Ia data are insufficient to detect power beyond the dipole. Using this tuning parameter we calculate the a_{lm} coefficients and the monopole and dipole terms from the following equations

$$\text{Monopole} = \frac{a_{00}}{\sqrt{4\pi}} \tag{2.40}$$

$$\text{Dipole} = \sqrt{\frac{3}{4\pi}}\sqrt{a_{10}^2 + \Re(a_{11})^2 + \Im(a_{11})^2} \tag{2.41}$$

$$\phi = -\arctan\left(\frac{\Im(a_{11})}{\Re(a_{11})}\right) \tag{2.42}$$

$$\theta = \arccos\left(\frac{a_{10}}{\sqrt{a_{10}^2 + \Re(a_{11})^2 + \Im(a_{11})^2}}\right) \tag{2.43}$$

These results are summarized in Table 2.

The velocity fields from WLS and CU are plotted in Figure 18. The magnitudes are comparable between the two methods, with WLS being slightly larger. The direction of the CU dipole points more toward a region of space which is well sampled. The WLS dipole is pulled toward a less sampled region which may be why the bulk flow measurement is larger in magnitude. This is explored more in §2.6.

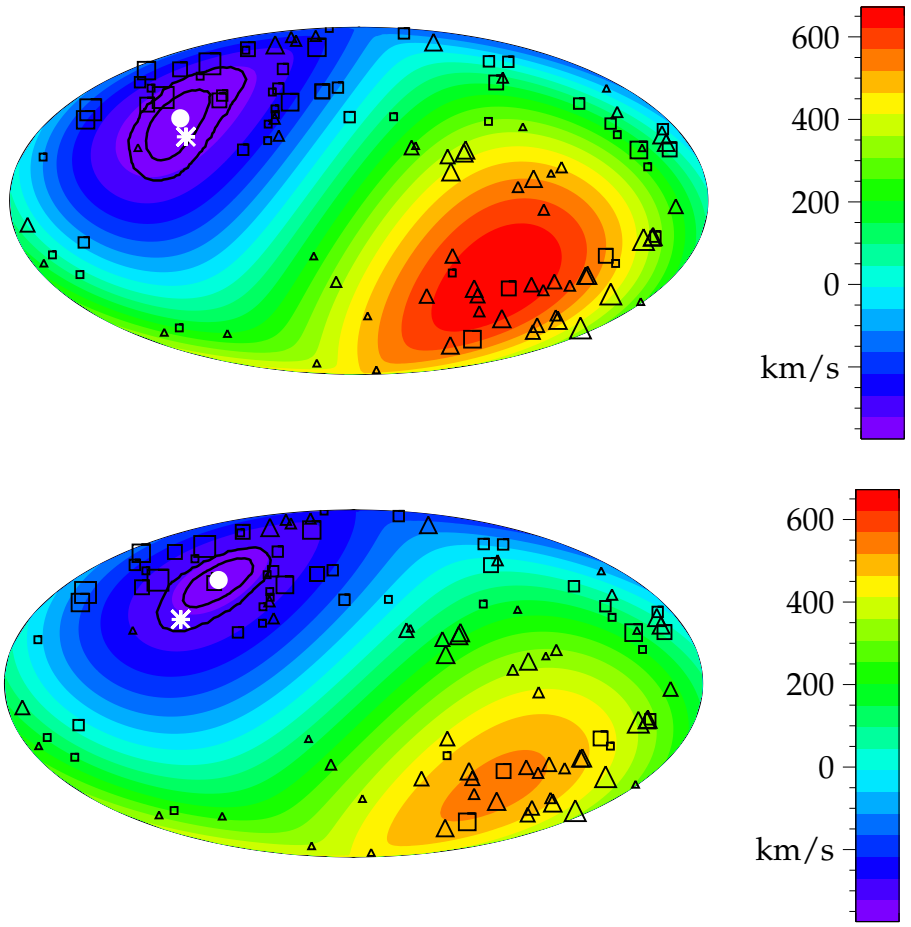

Figure 18 Peculiar velocity field for WLS (top) and CU (bottom) using the tuning parameter $J = 1$. The solid white circle marks the direction of the regression dipole, the white asterisk marks the CMB dipole in the rest frame of the Local Group, and the black triangles and squares mark the data points with positive and negative peculiar velocities. Contours are given to mark the 65% and 95% confidence bands of the direction of the dipole. The color scale indicates the peculiar velocity in km s^{-1}. We see that WLS and CU are in 95% agreement with the direction of the CMB dipole.

Table 3. Paired t-test results

a_{00}	a_{10}	$\Re(a_{11})$	$\Im(a_{11})$
1.50	0.23	1.72	1.66

To compare the CU and WLS bulk motions, we use a paired t-test. Because the coefficients were determined from the same set of data there is covariance between the parameters estimated from the two methods. Consider bootstrapping the data N times. For a single bootstrap let X be a coefficient from CU and Y be the same coefficient but derived from WLS. The paired t-statistic comes from the distribution of $X - Y$

$$t = \frac{\langle X - Y \rangle}{\sigma_{X-Y}} \tag{2.44}$$

where σ_{X-Y} is the standard deviation of the $X-Y$ distribution and $\langle X-Y \rangle$ is the mean. According to the central limit theorem, for large samples many test statistics are approximately normally distributed. For normally distributed data, $t < 1.96$ indicates that the values being compared are in 95% agreement. Performing a paired t-test on the measurements finds that the coefficients are in 95% agreement with the results summarized in Table 3. Because the risk values are so similar (Figure 17), we expect the methods to model the peculiar velocity field equally well and therefore expect the values to be statistically consistent.

To compare two independent measurements we perform a two-sample t-test, which gives us a statistical measure of how significant the difference between two numbers are. We first calculate the standardized test statistic $t = (x_1 - x_2)/\sqrt{\sigma_1^2 + \sigma_2^2}$, where x_1 and x_2 are the mean values of two measurements to be compared and σ_1 and σ_2 are the associated uncertainties. This statistic is suitable for comparing the CU or WLS bulk motion with the CMB dipole. We find the WLS Local Group bulk flow moving at 538 ± 86 km s^{-1} towards $(l, b) = (258^\circ \pm 10^\circ, 36^\circ \pm 11^\circ)$ which is consistent with the magnitude of the CMB dipole (635 km s^{-1}) and direction $(269^\circ, 28^\circ)$ with an agreement of $t_{\rm dip} = 1.12$, $t_l = 1.1$, and $t_b =$

Table 4. Summary of Dipole Results

Method	# SN Ia	Redshift Range CMB	Depth km s^{-1}	Magnitude km s^{-1}	Direction Galactic (l, b)
WLS	112	0.0043-0.028	4000	538 ± 86	$(258°, 36°) \pm (10°, 11°)$
CU	112	0.0043-0.028	4000	446 ± 101	$(273°, 46°) \pm (11°, 8°)$
Haugbølle et al. (2007)	74	0.0070-0.035	4500	$516 \pm {}^{57}_{79}$	$(248°, 51°) \pm ({}^{15°}_{20°}, {}^{15°}_{14°})$
Jha et al. (2007b)	69	0.0043-0.028	3800	541 ± 75	$(258°, 51°) \pm (18°, 12°)$

0.73. The CU bulk flow is moving at 446 ± 101 km s^{-1} towards $(l, b) = (273° \pm 11°, 46° \pm 8°)$. The CU bulk flow is in good agreement with the CMB dipole with $t_{\rm dip} = 1.88$, $t_l = 0.36$, and $t_b = 2.25$.

There is no strong evidence for a monopole component of the velocity field for either method. This merely demonstrates that we are using consistent values of M_V and H_0. For this analysis to be sensitive to a "Hubble bubble" (e.g., Jha et al., 2007b), we would look for a monopole signature as a function of redshift.

We can directly compare our results to those obtained in Jha et al. (2007b) using a two-sample t-test as our analysis covers the same depth and is in the same reference frame. They find a velocity of 541 ± 75 km s^{-1} toward a direction of $(l, b) = (258° \pm 18°, 51° \pm 12°)$. Our results for WLS and CU are compatible with Jha et al. (2007b) with $t < 1$ in magnitude and direction. We can also compare our results to those in Haugbølle et al. (2007) for their 4500 sample transformed to the Local Group rest frame. They find a velocity of 516 km s^{-1} toward $(l, b) = (248°, 51°)$. Their derived amplitude is slightly lower as their fit for the peculiar velocity field includes the quadrupole term. We note from the estimated risk curves, that it is not unreasonable to fit the quadrupole as the estimated risk is similar at $l = 1$ and $l = 2$. However, it is unclear if fitting the extra term improves the accuracy with which the field is modeled. Our results for CU and WLS agree with Haugbølle et al. (2007) with $t \leq 1$. Note that these t values may be slightly underestimated as a subset of SNe Ia are common between the two analyzes. A summary of dipole measurements is presented in Table 4.

2.6 DEPENDENCE OF CU AND WLS ON BULK FLOW DIRECTION

The WLS and CU analyses on real SN Ia data give dipole directions that follow the well-sampled region. This may raise suspicion that the CU method is following the sampling when determining the dipole. In this section we examine the behavior of our methods on simulated data as we vary the direction of the dipole.

We create simulated data sets from the sampling density derived from the actual data to verify the robustness of our analysis. We test two randomly chosen bulk flows which vary in magnitude and direction and sample 200 SNe Ia for each case. One dipole points toward a well-populated region of space and the other into a sparsely sampled region. A weak quadrupole is added such that the estimated risk gives a minimum at $l = 1$. There is power beyond the tuning parameter so we expect a bias to be introduced onto the coefficients for WLS. The velocity fields for the two cases are given by

$$\begin{aligned}
\text{Case 1} \ : \ V &= 400Y_{01} + 590\Re Y_{11} + 830\Im Y_{11} \\
&\quad -100Y_{20} + 200\Re Y_{21} + 250\Im Y_{21} - 175\Re Y_{22} + 140\Im Y_{22} \\
\text{Case 2} \ : \ V &= -642Y_{01} + -38\Re Y_{11} + 810\Im Y_{11} \\
&\quad -100Y_{20} + 200\Re Y_{21} + 250\Im Y_{21} - 175\Re Y_{22} + 140\Im Y_{22}
\end{aligned}$$

For Case 1 the true dipole points along a sparsely sampled direction (Figure 19). In the top row are the simulated velocity field and the dipole component of that field. On the bottom are the results for CU and WLS. In all plots the true direction of the dipole is shown as a white circle. As WLS is optimized to model the velocity field, it is no surprise that WLS overestimates the magnitude of the dipole (bottom left) to better model the simulated velocity field (top left). This behavior is very similar to what we saw in §2.4. WLS is aliasing power onto different scales to best model the field, sacrificing unbiased coefficients. If we compare the CU velocity field to the simulated velocity field we see that it is less accurate but that CU's estimate of the dipole is a more accurate measure of the true dipole (top right). Both methods are recovering the direction of the dipole at roughly the 2σ level, leading us to conclude that it is the magnitude of the dipole which is most variable between the methods for this case.

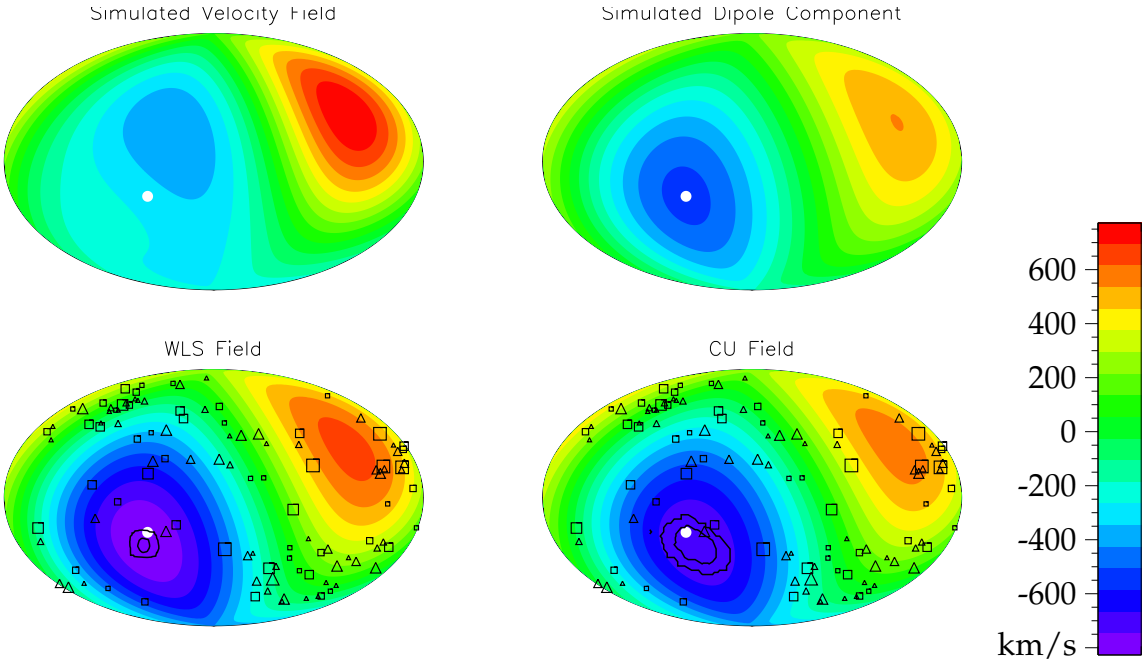

Figure 19 Simulated velocity field for Case 1 (top left), dipole component of that field (top right), WLS dipole result (bottom left) and CU dipole result (bottom right) for a typical simulation of 200 data points. Data points are overlaid as triangles (positive peculiar velocity) and squares (negative peculiar velocity). Error contours (68% and 95%) are marked as black lines. The 95% contour for CU and WLS enclose the direction of the true dipole, marked as a white circle. The WLS result is more representative of the actual field while CU has a more accurate dipole.

One may more easily see the difference in WLS and CU determined coefficients in Figure 20, where we plot the difference distributions (regression determined coefficients minus the true coefficients) for 770 simulations of 200 data points. Ideally these distributions would be centered at zero with a narrow spread. The distance the mean of the distribution is from zero is an indication of the bias. The spread is an indication of the error. We see that WLS is more biased than CU but the uncertainty in CU is much larger.

In Case 2 the true dipole points along a region of space which is densely sampled (Figure 21). In the bottom left plot we see the direction of the dipole for WLS is pulled down toward a region of space which is less sampled. Since the true direction of the dipole is well constrained by data, to more accurately model the flow field WLS must alter the direction

Table 5. Probability of the 95% confidence interval containing the truth

	a_{00}	a_{10}	$\Re(a_{11})$	$\Im(a_{11})$
Case 1				
WLS	0.50	0.88	0.86	0.88
CU	0.93	0.90	0.89	0.92
Case 2				
WLS	0.49	0.88	0.86	0.88
CU	0.93	0.94	0.94	0.91

of the dipole toward a less sampled region. This is necessary as WLS is trying to account for power which is really part of the quadrupole with the dipole term. As a result, WLS misses the true direction of the dipole at the 95% confidence level. This may be similar to what we see in Figure 18 where the WLS dipole points more along the galactic plane when compared to CU. CU is less sensitive to this affect as it is optimized to find unbiased coefficients. Correspondingly, CU encloses the true direction of the dipole at the 95% confidence level. In Figure 22 we plot the difference distributions as we did for Case 1. It is clear that the WLS coefficients are more biased than CU but that the uncertainty in CU is much larger.

We can explicitly check the bias of the methods using the simulated data of Section 2.6. The important calculation is the probability that the 95% confidence interval for a given simulation includes the true value. For an accurately determined confidence interval, this should happen 95% of the time. We start with one simulated data set and perform 1000 bootstrap resamples. This gives us distributions of the coefficients from which we can determine the confidence intervals. We then determine if the true values falls within this interval. After doing this for all of the simulations from §2.6, we can measure how often the true value falls within the confidence interval. These probabilities are summarized in Table 5.

CU is more accurate in its estimate of the 95% confidence interval for both cases. The lower probabilities for WLS are a result of the bias in the method. By construction, the WLS confidence intervals are centered about the regression-determined coefficients. If the coefficients are biased, the WLS intervals are shifted and the true value will lie outside this interval more often than expected.

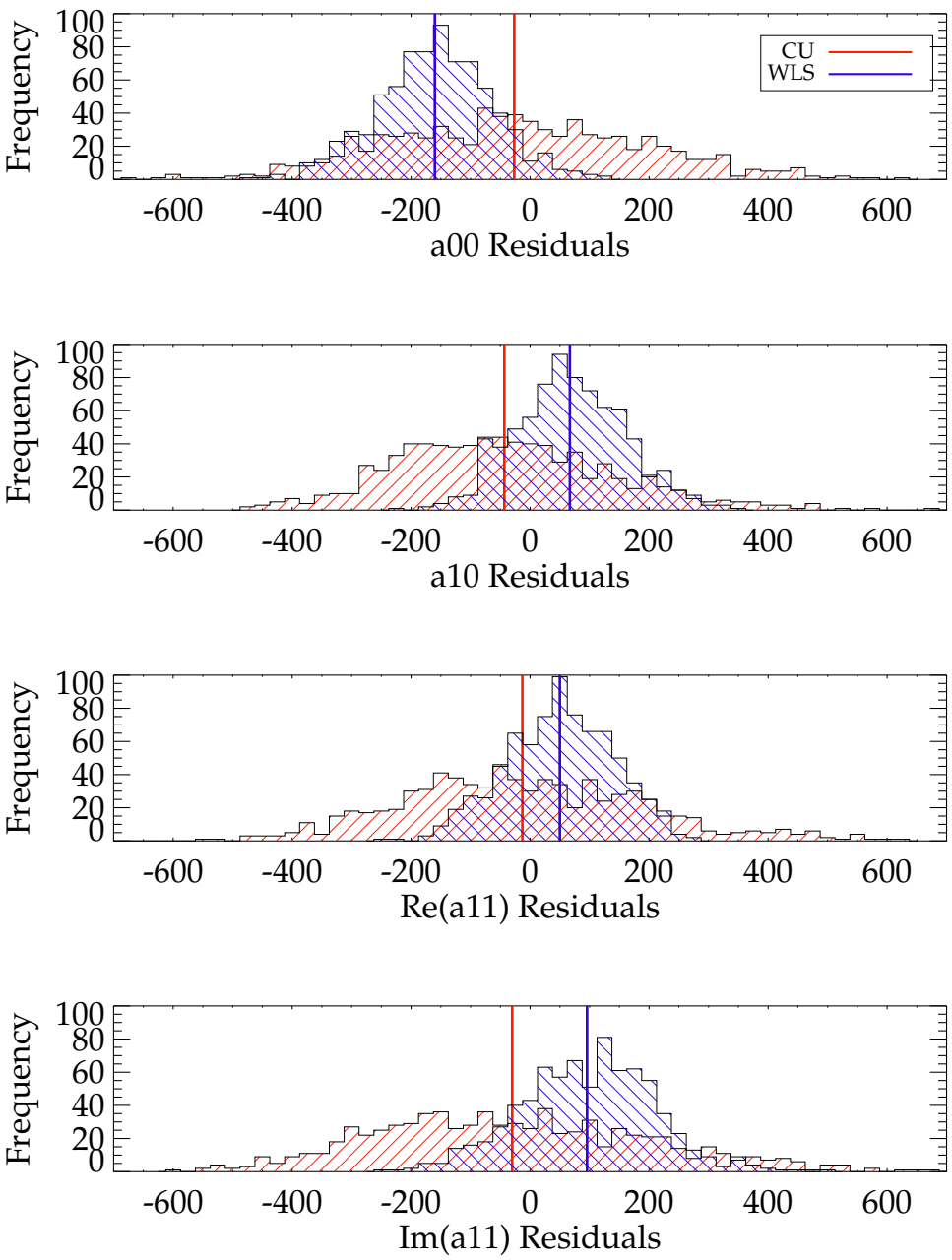

Figure 20 Distribution of CU (WLS) coefficients minus the true values for Case 1 in red (blue) for 770 simulated data sets. The vertical lines indicate the mean of the distribution. The distance the mean is from zero is an indication of the bias. The spread in the distributions indicates the uncertainty. WLS is more biased than CU but CU has larger uncertainties.

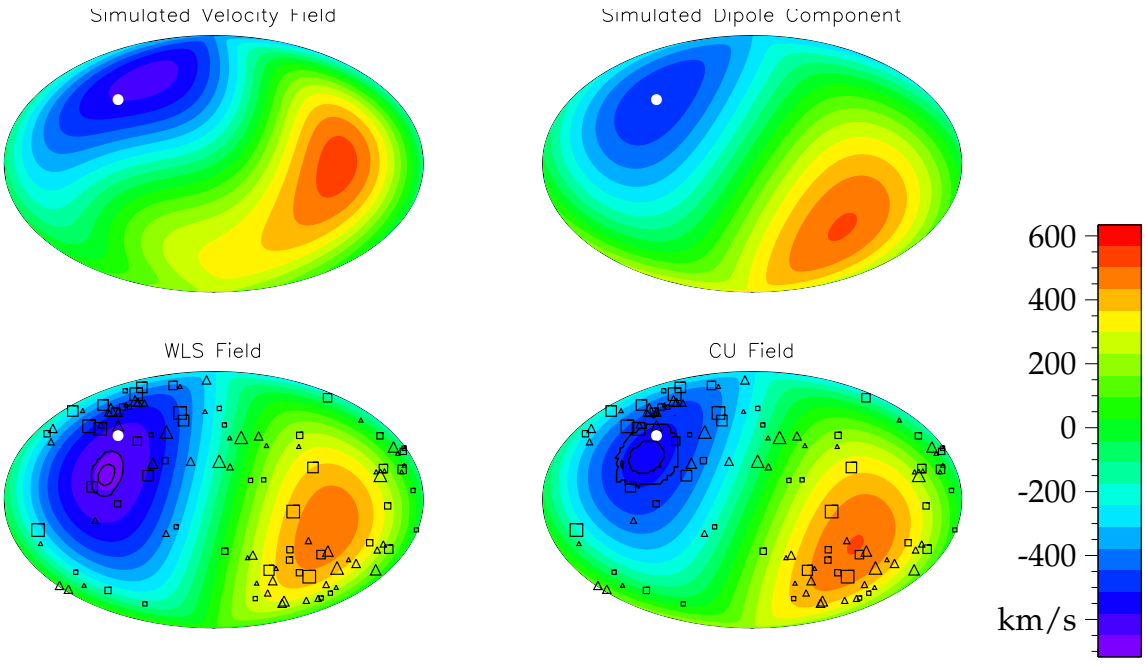

Figure 21 Simulated velocity field for Case 2 (top left), dipole component of that field (top right), WLS dipole result (bottom left) and CU dipole result (bottom right) for a typical simulation. Data points are overlaid as triangles (positive peculiar velocity) and squares (negative peculiar velocity). In this scenario, the 95% contour for WLS, marked in black, completely misses the direction of the true dipole, marked as the white circle. The WLS dipole is pulled toward a region of space less sampled.

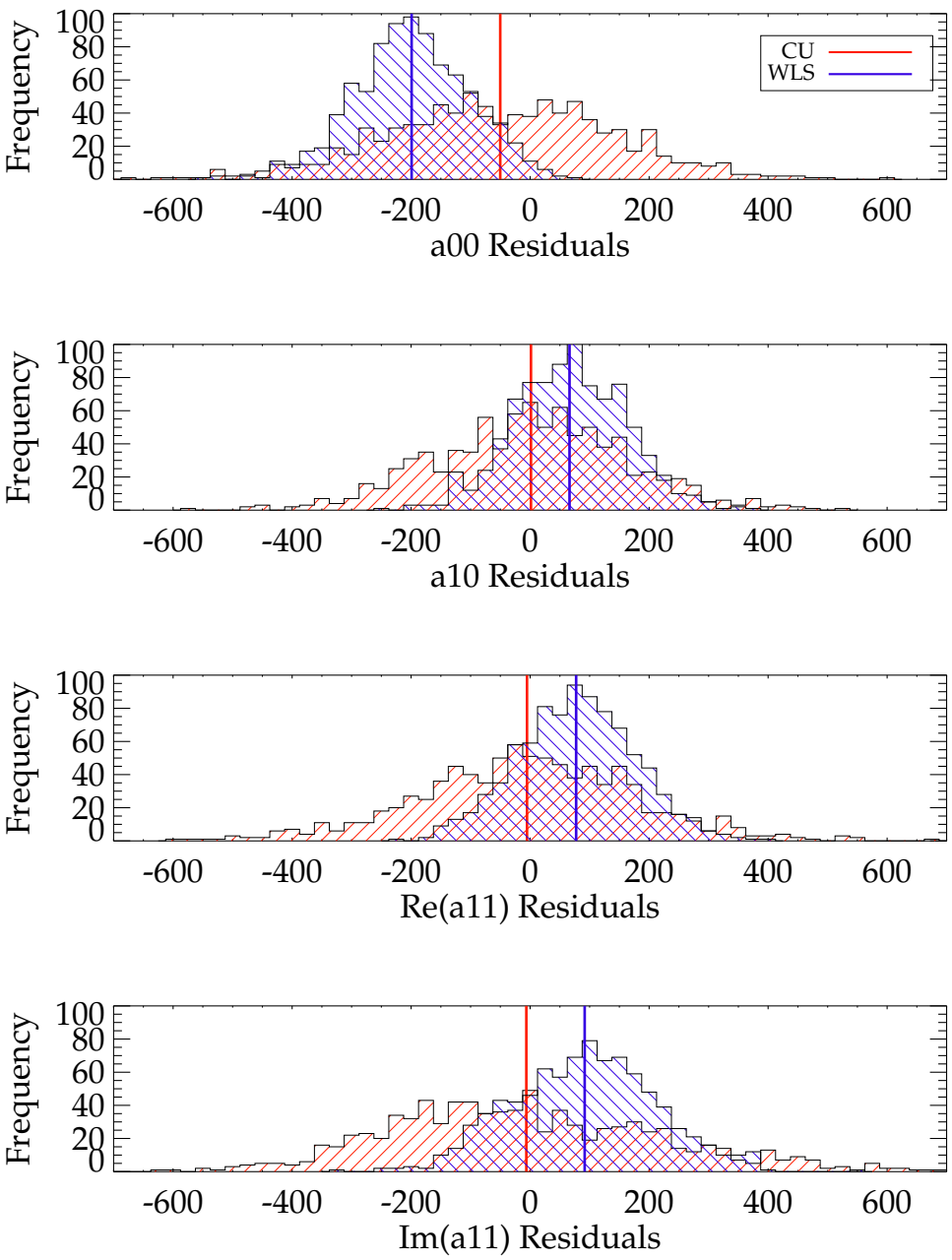

Figure 22 Distribution of CU (WLS) coefficients minus the true values for Case 2 in red (blue) for 874 simulated data sets. The vertical lines indicate the mean of the distribution. WLS is consistently more biased than CU

2.7 CONCLUSION

In this work, we applied statistically rigorous methods of non-parametric risk estimation to the problem of inferring the local peculiar velocity field from nearby SNe Ia. We use two non-parametric methods - WLS and CU - both of which employ spherical harmonics to model the field and use the risk to determine at which multipole to truncate the series. The minimum of the estimated risk will tell one the maximum multipole to use in order to achieve the best combination of variance and bias. The risk also conveys which method models the data most accurately.

WLS estimates the coefficients of the spherical harmonics via weighted least squares. We show that if the data are not drawn from a uniform distribution and if there is power beyond the maximum multipole in the regression, WLS fitting introduces a bias on the coefficients. CU estimates the coefficients without this bias, thereby modeling the field over the entire sky more realistically but sacrificing in accuracy. Therefore, if one believes there is power beyond the tuning parameter or the data are not uniform, CU may be more appropriate when estimating the dipole, but WLS may describe the data more accurately.

After applying non-parametric risk estimation to our sample we find that there are not enough data at this time to measure power beyond the dipole. There is also no significant evidence of a monopole term for either WLS or CU, indicating that we are using consistent values of H_0 and M_V. The WLS Local Group bulk flow is moving at 538 ± 86 km s^{-1} towards $(l, b) = (258^\circ \pm 10^\circ, 36^\circ \pm 11^\circ)$ and the CU bulk flow is moving at 446 ± 101 km s^{-1} towards $(l, b) = (273^\circ \pm 11^\circ, 46^\circ \pm 8^\circ)$. After performing a paired t-test we find that these values are in agreement.

To test how CU and WLS perform on a more realistic data set, we simulate data similar to the actual data and investigate how they perform as we change the direction of the dipole. We find for our two test cases, that CU produces less biased coefficients than WLS but that the uncertainties are larger for CU. We also find that the 95% confidence intervals detemined by CU are more representative of the actual 95% confidence intervals.

We estimate using simulations that with $\sim$200 data points, roughly double the current sample, we would be able to measure the quadrupole moment assuming a similarly dis-

tributed data set. Nearby SN Ia programs such as the CfA Supernova Group, Carnegie Supernova Project, KAIT, and the Nearby SN Factory will easily achieve this sample size in the next one to two years. The best way to constrain higher-order moments however, would be to obtain a nearly uniform distribution of data points on the sky. Haugbølle et al. (2007) estimate that with a uniform sample of 95 SNe Ia we can probe $l = 3$ robustly.

With future amounts of data the analysis can be expanded not only out to higher multipoles, but to modeling the peculiar velocity field as a function of redshift. This will enable us to determine the redshift at which the bulk flow converges to the rest frame of the CMB. Binning the data in redshift will also allow one to look for a monopole term that would indicate a Hubble bubble.

As there is no physical motivation for using spherical harmonics to model the sampling density, future increased amounts of data will also allow us to use non-parametric kernel smoothing both to estimate h and the peculiar velocity field; this would be ideal for distributions on the sky which subtend a small angle, like the SDSS-II Supernova Survey sample (Sako et al., 2008; Frieman et al., 2008).

2.8 ACKNOWLEDGMENTS

We would like to thank Malcolm Hicken for sharing the consistent results and RPK for his detailed useful comments. We would also like to thank Jeff Newman for useful discussions and the referee for useful suggestions. This research has made use of the NASA/IPAC Extragalactic Database (NED) which is operated by the Jet Propulsion Laboratory, California Institute of Technology, under contract with the National Aeronautics and Space Administration.

3.0 LIKELIHOOD-FREE COSMOLOGICAL INFERENCE WITH TYPE IA SUPERNOVAE: APPROXIMATE BAYESIAN COMPUTATION FOR A COMPLETE TREATMENT OF UNCERTAINTY

Cosmological inference becomes increasingly difficult when complex data-generating processes cannot be modeled by simple probability distributions. With the ever-increasing size of data sets in cosmology, there is increasing burden placed on adequate modeling; systematic errors in the model will dominate where previously these were swamped by statistical errors. For example, Gaussian distributions are an insufficient representation for errors in quantities like photometric redshifts. Likewise, it can be difficult to quantify analytically the distribution of errors that are introduced in complex fitting codes. Without a simple form for these distributions, it becomes difficult to accurately construct a likelihood function for the data as a function of parameters of interest. Approximate Bayesian computation (ABC) provides a means of probing the posterior distribution when direct calculation of a sufficiently accurate likelihood is intractable. ABC allows one to bypass direct calculation of the likelihood but instead relies upon the ability to simulate the forward process that generated the data. These simulations can naturally incorporate priors placed on nuisance parameters, and hence these can be marginalized in a natural way. We present and discuss ABC methods in the context of supernova cosmology using data from the SDSS-II Supernova Survey. Assuming a flat cosmology and constant dark energy equation of state, we demonstrate that ABC can recover an accurate posterior distribution. Finally, we show that ABC can still produce an accurate posterior distribution when we contaminate the sample with Type IIP supernovae.

3.1 INTRODUCTION

Since the discovery of the accelerated expansion of our Universe (Riess et al., 1998; Perlmutter et al., 1999), the quality of SN Ia data sets has improved and the quantity has grown to thousands through individual efforts with the Hubble Space Telescope (Knop et al., 2003; Riess et al., 2004; Amanullah et al., 2010) and surveys such as the Supernova Legacy Survey (Astier et al., 2006; Conley et al., 2011), the ESSENCE Supernova Survey (Miknaitis et al., 2007; Wood-Vasey et al., 2007), the CfA Supernova group (Hicken et al., 2009a, 2012), the Carnegie Supernova Project (Contreras et al., 2010; Stritzinger et al., 2011), the Sloan Digital Sky Survey-II (SDSS-II; Lampeitl et al. (2010)), and the Lick Observatory Supernova Search (Ganeshalingam et al., 2010). Additional current and near-future surveys such as the Palomar Transient Factory[1] (Law et al., 2009), the Panoramic Survey Telescope and Rapid Response System (Pan-STARRS)[2], SkyMapper[3], and the Dark Energy Survey[4] will increase the sample by another order of magnitude with the goal of obtaining tighter constraints on the nature of dark energy. The Large Synoptic Survey Telescope (LSST) anticipates observing hundreds of thousands of well-measured SNe Ia (LSST Science Collaborations et al., 2009).

In this new regime of large numbers of SNe Ia the weaknesses and limitations of our current χ^2 likelihood approach to estimating cosmological parameters are becoming apparent. For example, with limited spectroscopic follow-up, we must rely on light-curve classification codes and photometric redshift tools to maximize the scientific potential of SN Ia cosmology with LSST and near-future surveys. These two crucial steps alone introduce a nontrivial component to our probability models from which we construct the likelihood. Additionally, there are significant systematic uncertainties including errors from calibration, survey design and cadence, host galaxy subtraction and intrinsic dust, population evolution, gravitational lensing, and peculiar velocities. All of these uncertainties contribute to a probability model which simply cannot be accurately described by a multivariate normal distribution.

[1] http://www.astro.caltech.edu/ptf/
[2] http://pan-starrs.ifa.hawaii.edu/public/
[3] http://www.mso.anu.edu.au/skymapper/
[4] http://www.darkenergysurvey.org/

In this paper we describe how the statistical technique of approximate Bayesian computation (ABC) can be used to overcome these challenges and explore the space of cosmological parameters in the face of non-Gaussian distributions of systematic uncertainties, complicated functional priors, and large data sets. We encourage the reader to read the recent paper by Cameron & Pettitt (2012) for an introduction to and application of ABC in the context of galaxy evolution. We here focus on supernova cosmology, but ABC has applicability in a wide range of forward-modeling problems in astrophysics and cosmology.

3.1.1 Classical Estimation of Cosmological Parameters from SN Ia Data

Cosmological inference with SNe Ia is a classical statistical estimation problem. We have data, our set of supernova light curve observations, and we seek to infer something about the Universe in which we live. It is standard in cosmology to adopt a Bayesian approach to inference. To clarify our basic conceptual and notational framework, we review Bayes theorem, a simple identity which relates the posterior probability distribution–the probability of a set of model parameters given the data–to the probability of the data given the model, the likelihood. More precisely, the posterior probability distribution is derived as

$$\pi(\theta|\,\mathbf{x}) = \frac{p(\mathbf{x}|\,\theta)\pi(\theta)}{p(\mathbf{x})}, \tag{3.1}$$

where $p(\mathbf{x}|\theta)$ is the likelihood, $\pi(\theta)$ is the prior on the vector of model parameters θ, and $p(\mathbf{x})$ is the marginal probability of the data $\mathbf{x}$ ($p(\mathbf{x}) = \int_\Theta p(\mathbf{x}|\theta)\pi(\theta)d\theta$). The Bayesian framework is powerful in that it allows evidence and experience to modify the prior. The approach is challenging, however, in that standard computation methods rely upon full specification of the likelihood $p(\mathbf{x}|\,\theta)$; this can be challenging in applications of interest.

For example, consider a cosmological model for which the distance modulus can be written as $\mu_{\rm model} = \mu_{\rm model}(\Omega_M, \Omega_\Lambda, w, z)$. If we assume that each measured μ has a probability distribution function (PDF) described by a Gaussian with standard deviation σ we can write the likelihood for a single observation as

$$p(\mu_i, z_i|\Omega_M, \Omega_\Lambda, w) \propto \exp\left[-\frac{(\mu_i - \mu_{\rm model}(z_i, \Omega_M, \Omega_\Lambda, w))^2}{2\sigma_i^2}\right]. \tag{3.2}$$

If the distance observations are independent after calibration such that there are no correlated uncertainties we can simply multiply the likelihood of each observation together. By taking the logarithm, we can write a more convenient form of the likelihood as follows

$$-2\ln\left(p(\mu, z|\Omega_M, \Omega_\Lambda, w)\right) = K + \sum_{i=1}^{N} \frac{(\mu_i - \mu_{\rm model}(z_i, \Omega_M, \Omega_\Lambda, w))^2}{\sigma_i^2}, \tag{3.3}$$

where K is an unimportant constant, giving us the familiar χ^2 statistic. Note that the use of this form of the likelihood function and χ^2 statistic is based on the assumption of independent data with normally distributed uncertainties.

Traditionally when making cosmological inference with SNe Ia one calculates the χ^2 statistic (Conley et al., 2011; Kessler et al., 2009a; Wood-Vasey et al., 2007; Astier et al., 2006; Riess et al., 2004). One method of including systematic uncertainties in such a framework is to use the "quadrature" method, accurately named by Conley et al. (2011). Systematic errors which are not redshift dependent and add scatter to the overall Hubble diagram are added in quadrature to the statistical uncertainties. For other sources of systematic uncertainty it is typical to perform the analysis with and without including the systematic effect on the data. The difference in inferred cosmological parameter is then a measure of the systematic uncertainty. All systematic effects are then added in quadrature as the quoted total systematic uncertainty. This method has been used in recent cosmological analyses by Kessler et al. (2009a); Wood-Vasey et al. (2007) and Astier et al. (2006). It has the advantage of being simple to implement but the disadvantage of missing correlations between systematic uncertainties, not producing the full likelihood, and could be inappropriate for asymmetric error distributions (Barlow, 2003). One also has the difficult task of estimating the size of the systematic uncertainty and implementing its effect in the analysis.

Conley et al. (2011) presented a more thorough approach to incorporating systematic uncertainties into a χ^2 analysis using a covariance matrix. By implementing a covariance matrix one can drop the assumption of independent data in Equation 3.3. The covariance matrix can be decomposed into a diagonal, statistical component and two off-diagonal matrices which include statistical and systematic uncertainty. These off-diagonal covariance matrices include uncertainties from, e.g., uncertainty in the supernova model which is statistical in nature but could be correlated between different SNe Ia and uncertainty in zero

points which would systematically affect all SNe Ia. Kowalski et al. (2008) and Amanullah et al. (2010) present similar methods which are approximations to Conley et al. (2011)'s covariance matrix approach. However, the overall approach must be modified for uncertainties due to, e.g., type contamination and Malmquist bias. They have the effect of adding or removing supernovae from the sample which is difficult to represent in a covariance matrix. For systematic effects such as these the field of supernova cosmology is moving toward calculating the corrections to the data using artificial SNe Ia generated from Monte Carlo simulations.

Bayesian inference becomes increasingly difficult as we depart from normal error distributions or when the likelihood function is not analytically or computationally tractable. Direct calculation of the likelihood may involve many integrations over systematic uncertainties, nuisance parameters, and latent variables. These integrations can make the use of standard Markov Chain Monte Carlo (MCMC) techniques very challenging and computational expensive. It may also be incredibly difficult to construct an analytic probability model over which to marginalize.

ABC allows one to bypass direct calculation of the likelihood by simulating data from the posterior distribution. The posterior distribution is then constructed from the model parameters necessary to simulate data which resemble the observed data. By incorporating into the simulation all of the statistical and systematic uncertainties for which we have models and priors, the simulation *knows* about the complicated probability model even thought the observer may not be able to have the model written out as a set of equations or numerical integrals. By simulating many realistic data sets one can marginalize over the nuisance parameters and systematic uncertainties such that high-dimensional marginalization problems, as in population genetics for which ABC techniques were first developed, are now computationally feasible. ABC is a consistent framework to incorporate systematic uncertainties with the cosmological model and more clearly defines what it means to use Monte Carlo simulations of artificial SNe Ia to quantify systematic uncertainty.

We begin in Section 3.2 by motivating the general problem and discussing the breakdown of current cosmological inference methods using a simple example. In Section 3.3 we outline three separate ABC algorithms and discuss their merits. To provide the reader with an

introductory example of using ABC, we then illustrate how one might perform cosmological inference with sequential Monte Carlo (SMC) ABC using the simple model discussed in Section 3.2. In Section 3.4 we present a more sophisticated analysis using SNe Ia from the SDSS-II Supernova Survey and demonstrate how one might perform cosmological inference with a tool like the SuperNova ANAlysis (SNANA) (Kessler et al., 2009c) software using SMC ABC techniques. We compare our results to the cosmological analysis performed in Kessler et al. (2009a) using statistical errors only. At the end of this section we show that ABC can recover the full posterior distribution when we contaminate the data with simulated Type IIP supernovae. We discuss directions for future work in Section 3.5 and conclude in Section 3.6.

3.2 GENERAL PROBLEM FORMULATION

Here we establish notation that we will use in discussing the SN Ia inference problem. Below we explain how this framework could be extended to other cosmological inference challenges. Let μ_i be the measured distance modulus of the ith SN Ia in our sample, τ_i be its true distance modulus, z_i be the estimated redshift, and θ be the vector of cosmological parameters. We will use bold faced variables to indicate a set of n supernovae, e.g., $\mathbf{z} = \{z_1, ..., z_n\}$. Here, we stress that the "estimated redshift" will be, in practice, the redshift as estimated from photometry, i.e., the photometric redshift.

The underlying objective is to determine the posterior of the cosmological parameters θ given the observed data $(\boldsymbol{\mu}, \mathbf{z})$. There are two natural analytical routes, both of which lead to the same challenges. The first route is to note that the posterior of θ can be decomposed as

$$\pi(\theta|\, \boldsymbol{\mu}, \mathbf{z}) = K p(\boldsymbol{\mu}|\, \theta, \mathbf{z}) \pi(\theta, \mathbf{z}) \tag{3.4}$$

where K is a constant that does not depend on θ and

$$p(\boldsymbol{\mu}|\, \theta, \mathbf{z})\pi(\theta, \mathbf{z}) = \left[\int p(\boldsymbol{\mu}|\, \theta, \mathbf{z}, \boldsymbol{\tau})\, p(\boldsymbol{\tau}|\, \theta, \mathbf{z})\, d\boldsymbol{\tau} \right] \pi(\theta, \mathbf{z}) \tag{3.5}$$

$$= \left[\int p(\boldsymbol{\mu}|\, \theta, \boldsymbol{\tau})\, p(\boldsymbol{\tau}|\, \theta, \mathbf{z})\, d\boldsymbol{\tau} \right] \pi(\theta, \mathbf{z}). \tag{3.6}$$

Note that in this last step, the density of $\boldsymbol{\mu}$ conditional on θ and $\mathbf{z}$ is replaced with the density of $\boldsymbol{\mu}$ conditional only on θ. Here we are assuming that $\boldsymbol{\mu}$ and $\mathbf{z}$ are independent given $\boldsymbol{\tau}$: once $\boldsymbol{\tau}$ is known, the information in $\mathbf{z}$ does not affect the distribution of $\boldsymbol{\mu}$. We note that this assumption is not true if one is using the photometric redshift determined from the supernova light curve.

We could pose this problem in general statistical terms as follows. Assume that $\boldsymbol{\mu} = \{\mu_1, \mu_2, \ldots, \mu_n\}$ are random variables such that the distribution of μ_i is determined by parameters θ and τ_i. Here, θ represents the unknown parameters common to the μ_i while τ_i are the object-specific parameters. We further assume the existence of additional data, denoted z_i, which have the property that μ_i and z_i are independent conditional on τ_i. The quantities z_i can be thought of as properties that help in the estimation of τ_i, but would not be useful for estimating θ if τ_i were known.

Note that each of μ_i and τ_i could be vectors. For example, in Mandel et al. (2011), μ_i stores the full observed light curve of the supernova and τ_i comprises not only the true distance modulus, but also parameters that capture the effect of extinction and dust and that define the true, underlying light curve. As mentioned above, these have the property that, if τ_i were known, z_i would not provide useful additional information for the estimation of θ.

The second route is to rewrite the posterior as

$$\pi(\theta|\,\boldsymbol{\mu}, \mathbf{z}) = \int p(\theta, \boldsymbol{\tau}|\,\boldsymbol{\mu}, \mathbf{z})\, d\boldsymbol{\tau} \tag{3.7}$$

and then rely upon the fact that, as derived above,

$$p(\theta, \boldsymbol{\tau}|\,\boldsymbol{\mu}, \mathbf{z}) = p(\boldsymbol{\mu}|\,\theta, \boldsymbol{\tau})\, p(\boldsymbol{\tau}|\,\theta, \mathbf{z})\pi(\theta, \mathbf{z}) \tag{3.8}$$

to construct a hierarchical Bayesian model for the unknown "parameters" which now consist of both θ and $\boldsymbol{\tau}$. To analytically obtain the posterior in terms of only θ, one must integrate over $\boldsymbol{\tau}$, i.e., find

$$\int p(\boldsymbol{\mu}|\,\theta, \boldsymbol{\tau})\, p(\boldsymbol{\tau}|\,\theta, \mathbf{z})\, d\boldsymbol{\tau}. \tag{3.9}$$

This is exactly the form of the challenging integral that was confronted above in Equation (3.6). One can often justify further conditional independence assumptions and write

$$\int p(\boldsymbol{\mu}|\,\theta,\boldsymbol{\tau})\,p(\boldsymbol{\tau}|\,\theta,\mathbf{z})\,d\boldsymbol{\tau} = \int \prod_{i=1}^{n} p(\mu_i|\,\theta,\tau_i)\,p(\tau_i|\,\theta,z_i)\,d\boldsymbol{\tau} \tag{3.10}$$

$$= \prod_{i=1}^{n} \int p(\mu_i|\,\theta,\tau_i)\,p(\tau_i|\,\theta,z_i)\,d\tau_i. \tag{3.11}$$

Still, the computational feasibility of using analytical approaches to finding the posterior for θ will depend on the form of

$$p(\mu_i|\,\theta,z_i) = \int p(\mu_i|\,\theta,\tau_i)\,p(\tau_i|\,\theta,z_i)\,d\tau_i. \tag{3.12}$$

In practice, the complex nature of photometric redshift estimators will yield a complex form for the distribution $p(\tau_i|\,\theta,z_i)$.

An alternative is to adopt the "second route" described above but instead utilize MCMC methods to simulate from the posterior for both (θ,τ). This is the approach taken in Mandel et al. (2011). This avoids the integral over τ_i, but it is still apparent that practical implementation of analytical or MCMC methods when n is large (and hence $\boldsymbol{\tau}$ is of high-dimension) forces one to make choices for $p(\mu_i|\,\theta,\tau_i)$ and $p(\tau_i|\,\theta,z_i)$ which may not be realistic. Unfortunately, as n gets large, even small mistakes in the specification of these densities could lead to significant biases in the estimates of the parameters. This is one of the fundamental challenges facing cosmology as we are presented with ever-larger data sets. In what follows we will develop an example that illustrates this point.

3.2.1 A Simple Example

To begin, note that in the present example μ_i is the measured distance modulus, z_i is the measured redshift, τ_i is the true distance modulus, and θ represent the set of cosmological parameters. We ignore for the moment all parameters which affect the measured distance modulus except z_i and θ. The measured redshift z_i may differ from the true redshift of the supernova, which we will denote ζ_i. Consider the following three scenarios:

1. $z_i = \zeta_i$, *i.e., the redshift is known exactly.* In this case, and under our simplifying assumptions, we know exactly the value of τ_i, and hence the "density" $p(\tau_i \,|\, \theta, z_i)$ is a delta function at this known value.
2. The redshift is observed with some normal error. We model ζ_i with a Gaussian PDF with mean z_i and variance $\sigma^2_{z,i}$. In this case we can apply the so-called delta method and state that $p(\tau_i \,|\, \theta, z_i)$ is approximately Gaussian with mean $\mu(z_i, \theta)$. This scenario is analogous to measuring a spectroscopic redshift with a small error such that a Gaussian approximation for the PDF of ζ_i is sufficient or a photometric redshift which has a PDF which can be modeled well by a Gaussian.
3. z_i is observed with some complicated uncertainty. The PDF is not described by a simple function although $p(\tau_i \,|\, \theta, z_i)$ may be estimated using observed data. This is the case for most photometric redshifts.

Of course, the first case is unrealistic. In order to demonstrate the pitfalls of making unwarranted assumptions regarding the likelihood function, we will first focus on the second case, in particular assume that $p(\tau_i \,|\, \theta, z_i)$ is a Gaussian density with mean $\mu(z_i, \theta)$. The rationale for this approximation relies on the assumption that the true redshift ζ_i also has a Gaussian distribution, in this case with mean z_i and variance $\sigma^2_{z,i}$. The true distance modulus is $\tau_i = \mu(\zeta_i, \theta)$, so, using the standard linear approximation, we can argue that τ_i is approximately normal with mean $\mu(z_i, \theta)$ and variance

$$\left(\sigma^z_{\mu,i}\right)^2 = \left[\frac{\partial \mu(z_i, \theta)}{\partial z_i}\right]^2 \sigma^2_{z,i}. \tag{3.13}$$

Then, the observed distance modulus can be modeled as the true distance modulus plus some additional Gaussian error; this is taken to have mean zero and variance $(\sigma_{\mu,i})^2$. In a real-life application this variance includes uncertainty from the observed intrinsic dispersion in distance modulus and uncertainty from fitting the light curve.

This is the current approach in most cosmological analyses where one has spectroscopic redshifts for each SN Ia (Conley et al., 2011; Kessler et al., 2009a; Wood-Vasey et al., 2007; Astier et al., 2006). The uncertainty in redshift is transferred to the uncertainty in measured distance modulus and one can find an analytic solution to Equation 3.12 by noting that the integral is simply the convolution of two normal densities. Hence the result of Equation 3.12

is another normal density, but now with mean $\mu(z_i, \theta)$ and variance $\left(\sigma^z_{\mu,i}\right)^2 + (\sigma_{\mu,i})^2$. This approach is also possible for larger uncertainties like those from photometric redshifts, but the concern becomes the fact that the linear approximation utilized does not extend to larger ranges of redshift. In what follows we examine the consequences of making this Gaussian assumption for photometric redshift uncertainties when the approximation is not valid, i.e., we treat scenario 3 as if it were scenario 2.

Figure 23 shows the photometric versus spectroscopic redshift for a sample of 1744 SNe Ia generated using SNANA[5] version v9_32 and smoothed with a Gaussian kernel. To make this figure, light curves were simulated and fit from the MLCS2k2 model (Jha et al., 2007a) as described in Section 3.4 with the following changes; we fix the cosmology to $\Omega_\Lambda = 0.73$, $\Omega_M = 0.27$, and $w = -1$, and we estimate photometric redshifts when we fit the light curves without using a host galaxy photo-z prior.[6] We use this sample to represent a realistic joint distribution between the spectroscopic and photometric redshifts. We further assume that the spectroscopic redshift is equal to the true redshift $\zeta = z^{\text{spec}}$ and the observed redshift is the photometric redshift $z = z^{\text{phot}}$.

Figure 24 shows three cross-sections of the joint distribution of spectroscopic and photometric redshifts, comparing the photometric redshift distribution with the assumed Gaussian PDF. Our proposed model assumes that the horizontal cross-section of this distribution at z^{phot} is Gaussian with mean equal to z^{spec}. This figure demonstrates that the Gaussian approximation to the distribution of z^{spec} is not terrible. Further, under this Gaussian approximation $\mu(z_i^{\text{phot}}, \theta)$ should be approximately normal with mean τ_i, i.e., under the linear approximation the distance modulus estimated using the photometric redshift has mean equal to the true distance modulus. Figure 25 uses boxplots to show the distribution of $\tau_i - \mu(z_i^{\text{phot}}, \theta)$ at various values of z^{phot} for the simulated data. This plot reveals that there are significant deviations from the expected difference of zero.

The effect of this bias is made clear in Figure 26. This figure shows the 95% credible region as constructed by two different methods, which will be described below. In both cases, the data set utilized is the same. To construct this data set we simulated a sample of 200

[5] http://sdssdp62.fnal.gov/sdsssn/SNANA-PUBLIC/

[6] Please see Section 4.9 of the SNANA manual for details on measuring SN Ia redshift from photometry http://sdssdp62.fnal.gov/sdsssn/SNANA-PUBLIC/doc/snana_manual.pdf

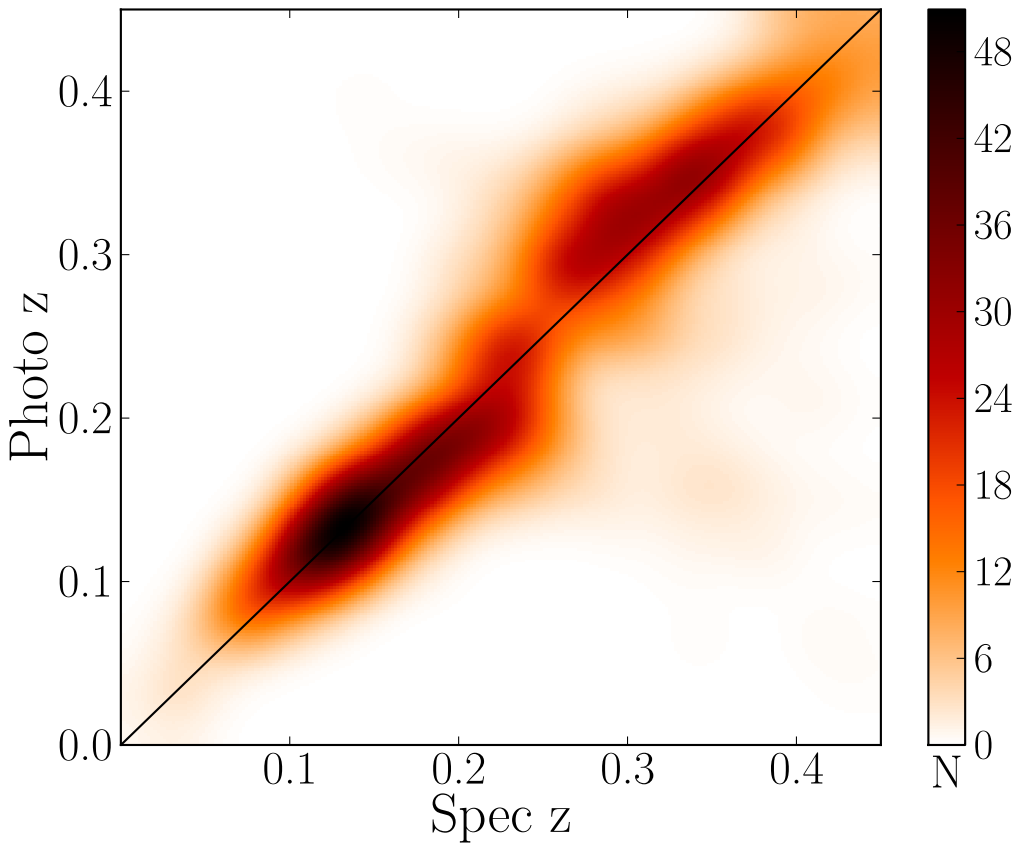

Figure 23 Photometric vs. spectroscopic redshift for 1744 simulated SNe Ia using SNANA and smoothed with a Gaussian kernel. Note the complex structure and asymmetry about the one-to-one line indicating departures from Gaussianity. This sample is used to represent a realistic joint distribution between the spectroscopic and photometric redshifts.

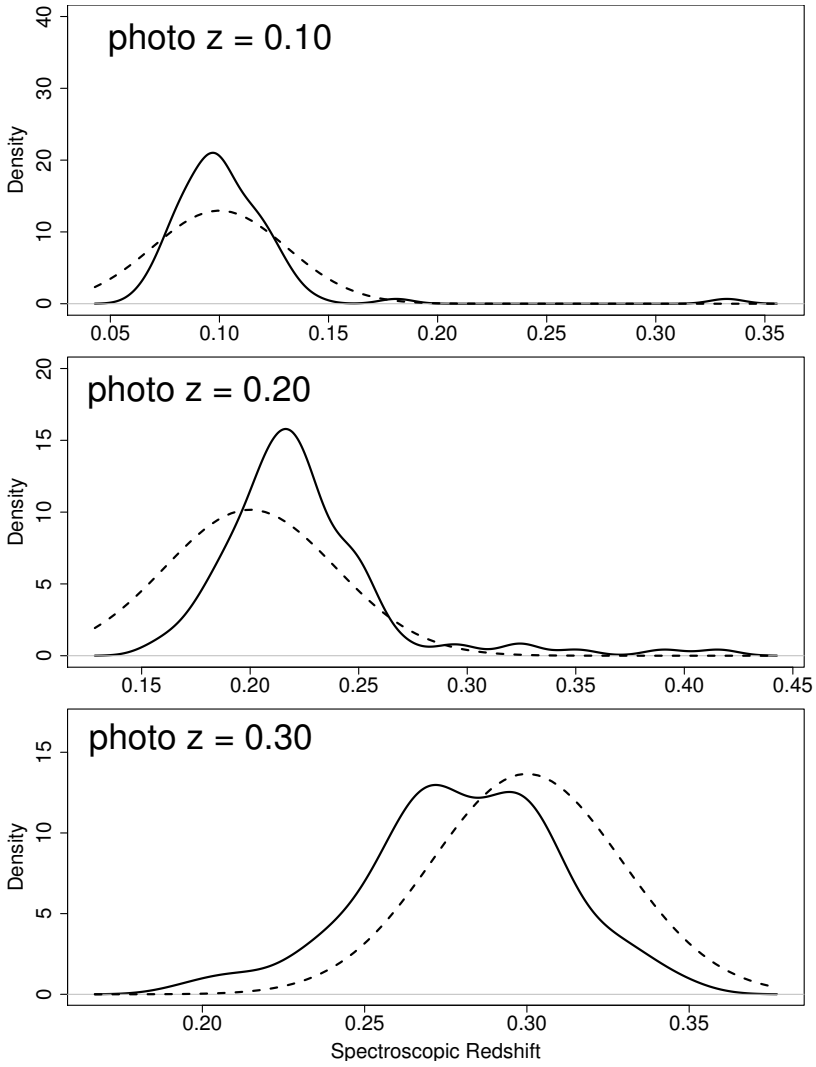

Figure 24 Comparison between the assumed Gaussian joint distribution between z and ζ_i (dashed) and non-parametric fits (solid) through the simulated data shown in Figure 23. Three cross-sections are shown, one at each of photometric redshifts of 0.1, 0.2, and 0.3. In each case, a bin of width 0.02 is constructed, centered on these values, and the observations which fall into this bin are used to estimate the distribution for spectroscopic redshift. A Gaussian is not a terrible approximation to these cross-sections, but is it far from ideal.

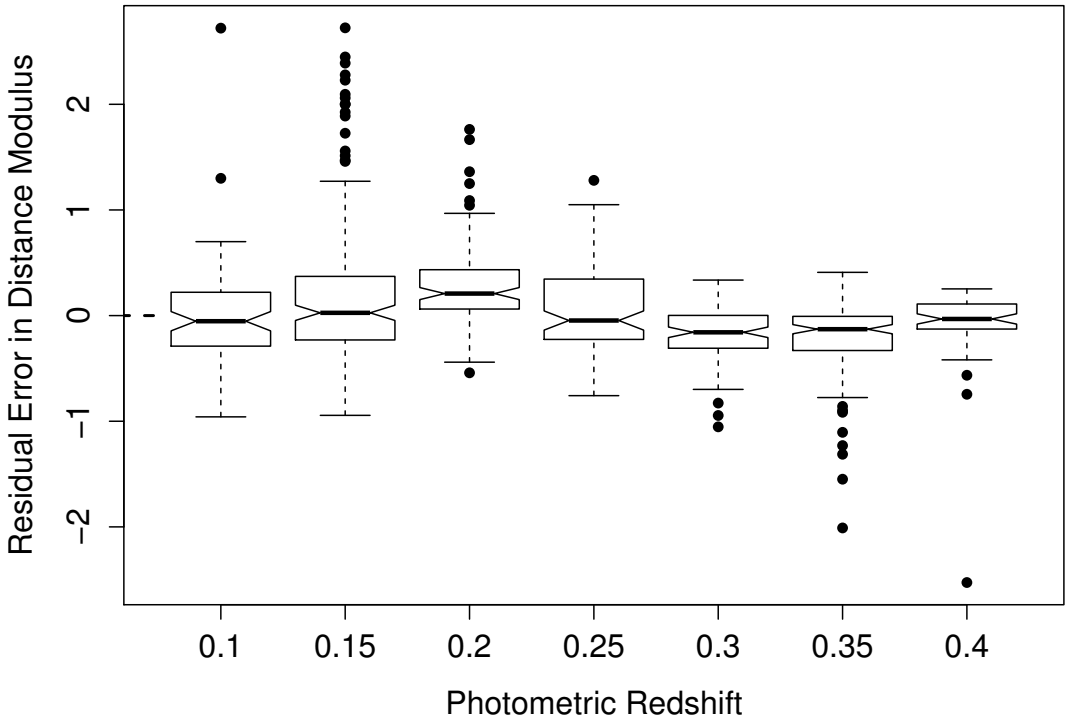

Figure 25 Distance modulus residual defined as $\mu(\zeta_i, \theta) - \mu(z_i, \theta)$ as a function of photometric redshift z_i. Under the described Gaussian approximation, these distributions should all have mean zero. The boxplots compare the distribution in different narrow redshift bins. The top and bottom of the box indicate the 25th and 75th percentile, the center line marks the median, and the "whiskers" mark 1.5 times the inter-quartile range. Points outside the whiskers are considered outliers. The "notch" in each boxplot allows for comparison to determine statistical significance: If the notches of two boxes do not overlap, then there is a statistically significant difference between the medians of the populations. Hence, it is evident that there is a bias introduced; the centers of these distributions are not always zero. This bias indicates that the Gaussian model for the joint distribution of (ζ, z) is inappropriate.

SNe Ia by drawing with replacement from the $(z^{\text{spec}}, z^{\text{phot}})$ sample shown in Figure 23. We then calculated $\tau = \mu(z^{\text{spec}}, \theta)$, where θ consists of $w = -1$ and $\Omega_M = 0.27$ and assumed a flat Universe. Finally, the observed distance modulus μ is constructed by adding mean-zero Gaussian error onto τ with variance $\sigma^2_{\mu,i} = 0.04$. The posterior for θ is found for this data set in two ways, and the 95% credible region[7] is displayed for each.

1. The solid line shows the credible region if the posterior is constructed using z^{spec}. It will serve as the fiducial reference for comparisons to the other region.
2. The dashed line is the credible region that results from using the approximation described above, i.e., assuming that the observed distance modulus has a Gaussian PDF with variance
$$\left[\frac{\partial \mu(z_i^{\text{phot}}, \theta)}{\partial z_i^{\text{phot}}}\right]^2 \sigma^2_{z^{\text{phot}},i} + \sigma^2_{\mu,i}. \tag{3.14}$$
The point of emphasis here is that the additional uncertainty in the redshift is now taken into account and reflected in the extra width of the region as compared to the solid region. The shift from the solid region to the dashed region is the result of a bias.

The bias shown in Figure 26 is much like the *attenuation bias* that results from inappropriately taking into account the errors in the predictor variables in a regression setting: Simply adding more error into the response will not adequately account for this additional error. There are methods for dealing with this additional error, but these are not practical in this setting because of another fundamental challenge: the variance of the error in redshift cannot be assumed to be constant, it needs to be modeled as a function of redshift. This *heteroskedastic* error introduces significant obstacles to any method that would seek to "back out" its effect on the estimates. In the next section we will instead consider approaches that exploit our ability to model and/or simulate the forward process that generated the data, and hence allow us to incorporate in a natural way the errors due to the use of photometric redshifts.

[7] The region which comprises 95% of the probability under the posterior is referred to as a *credible region* to distinguish it from a frequentist *confidence region*.

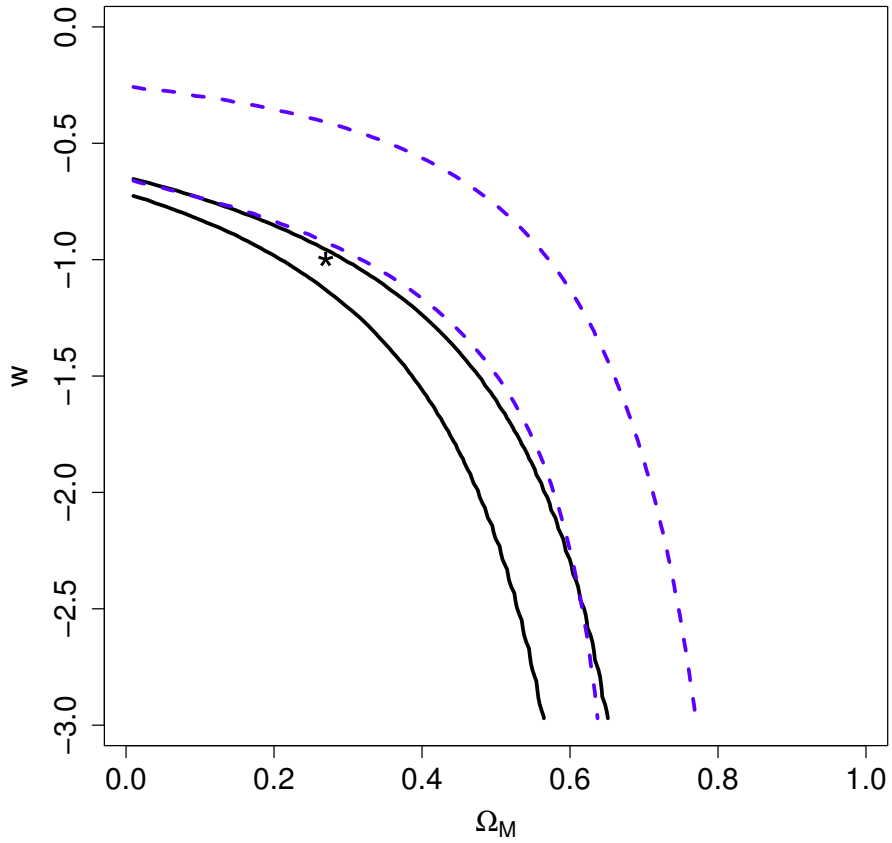

Figure 26 Comparison between the 95% credible regions for a simulated set of supernova formed by taking two approaches: (1) where the true redshift is known (black-solid line) and (2) where the approximation described in Section 2.1 is utilized (blue-dashed line). The star is at the true value of the parameters used in the simulation. The increased width of the confidence region is natural, given the use of photometric redshifts instead of spectroscopic redshifts, but the bias is a result of the inadequacy of the assumed Gaussian model.

3.3 APPROXIMATE BAYESIAN COMPUTATION

ABC methods simulate observations from the posterior distribution via algorithms that bypass direct calculation of the likelihood. This is done by drawing model parameters from some distribution, generating simulated data based on these model parameters and reducing the simulated data to summary statistics. Summary statistics are measures of the data designed to reduce the dimensionality of the data: they represent the maximum amount of information in the simplest form. Model parameters that generate data sufficiently similar to the observed data are drawn from the posterior distribution. This procedure allows one to simulate the complicated integral in Equation 3.12 rather than evaluate it but instead relies upon the ability to simulate the forward process that generated the observed data.

Here we review two classes of ABC algorithms; ABC rejection samplers and adaptive ABC algorithms. The roots of ABC techniques lie in the first class while the goal of adaptive ABC algorithms is to efficiently determine the relevant regions of parameter and probability space to sample from. In this section we will adopt a Bayesian approach and endeavor to determine (approximately) the posterior distribution of model parameters θ given observed data $\mathbf{x}$. The posterior is given by

$$\pi(\theta|\,\mathbf{x}) = \frac{p(\mathbf{x}|\,\theta)\pi(\theta)}{p(\mathbf{x})}, \tag{3.15}$$

where $p(\mathbf{x}|\,\theta)$ is the likelihood function and $p(\mathbf{x})$ is a normalization constant. For a review on ABC algorithms we refer the reader to Marin et al. (2011).

3.3.1 ABC Rejection Samplers

The basic ABC prescription is best considered for a situation in which the data $\mathbf{x}$ are discrete:

Rejection Sampler: Discrete Case

1. Draw candidate θ^* from $\pi(\theta)$,
2. Simulate data $\mathbf{x}^* \sim p(\mathbf{x}^*|\,\theta^*)$
3. Accept θ^* if $\mathbf{x}^* = \mathbf{x}$,

Repeat these steps until N candidates are accepted.

Under this algorithm, the probability that θ^* is accepted is exactly $\pi(\theta|\,\mathbf{x})$. Hence, it is simple in principle to generate a sample of size N from the posterior distribution. This sample is then used to estimate properties of the posterior distribution such as the 95% credible region.

In practice, however, most data are continuous, and we must instead decide to accept θ^* if $\mathbf{x}^*$ is suitably "close to" $\mathbf{x}$; hence, a metric or distance $\Delta(\mathbf{x}^*, \mathbf{x})$ must be chosen. Under this setup, the accepted parameter vectors θ^* are drawn from the posterior distribution conditioned on the simulated data being sufficiently close to the observed data. More precisely, the result will be a sample from the joint distribution $p(\mathbf{x}, \theta|\,\Delta(\mathbf{x}, \mathbf{x}^*) \leq \epsilon)$ where $\epsilon > 0$ is a fixed tolerance. If ϵ is small and one marginalizes over $\mathbf{x}$, then $p(\theta|\,\Delta(\mathbf{x}, \mathbf{x}^*) \leq \epsilon)$ is a reasonable approximation to $\pi(\theta|\,\mathbf{x})$ (Sisson et al., 2007). Note that if ϵ is very large the sample will be effectively drawn from the prior. The continuous version of the ABC rejection sampler, introduced by Tavare et al. (1997) and Pritchard et al. (1999), is built upon this idea:

Rejection Sampler: Continuous Case

1. Draw candidate θ^* from $\pi(\theta)$
2. Simulate data $\mathbf{x}^* \sim p(\mathbf{x}^*|\,\theta^*)$
3. Accept θ^* if $\Delta(\mathbf{x}^*, \mathbf{x}) \leq \epsilon$

Repeat these steps until N candidates are accepted.

If the data have many dimensions, requiring that $\Delta(\mathbf{x}^*, \mathbf{x}) \leq \epsilon$ may be impractical. For example, it would be nearly impossible to simulate 10^3 supernovae to within ϵ of the observed data even with the correct cosmology due to random photometric error, let alone population variance in realizations of stretch and color distribution.

Fu & Li (1997) and Weiss & von Haeseler (1998) improved Step 3 by instead making the comparison between lower-dimensional summaries of the data; here these will be denoted $s(\mathbf{x})$, or just s. The ideal choice for s would be a summary statistic that is a *sufficient statistic* for estimating θ. Technically, a vector s is sufficient if $p(\mathbf{x}|\,s, \theta)$ is not a function of θ, and hence the posterior conditioned on s is the same as the posterior conditioned on $\mathbf{x}$, i.e., $\pi(\theta|\,s) = \pi(\theta|\,\mathbf{x})$. Of course, one cannot expect to derive an exactly sufficient statistic when

the form of the likelihood is not known. Hence, much current research in ABC is focused on the derivation of *approximately sufficient statistics* or, more generally, summary statistics that preserve important information regarding the parameters of interest. Blum et al. (2012) provide an excellent overview and comparison of methods for constructing summary statistics. These methods generally fall into two categories: those that sift through a list of candidate summary statistics to find the "best" summary statistic as measured by some optimality criterion, and those that utilize the ability to simulate data sets under different parameter values as part of a process of fitting a regression where the responses are the parameters, and the predictors are the simulated data. This mapping is then used to transform observed summary statistics to parameters. For example, an early such example was Beaumont et al. (2002), who fit local linear regression to simulated parameter values on simulated summary statistics. The regression approach can be justified on theoretical grounds, see Fearnhead & Prangle (2012), and Cameron & Pettitt (2012) used this approach for their astronomical application. In our work, the relatively simple structure of the relationship between the simulated data and the parameters of interest leads to a natural approach to constructing a summary statistic: exploiting the known smooth distance modulus/redshift relationship. In other applications, there will not exist such a simple one-dimensional representation of the data, and these sophisticated approaches must be utilized.

There are advantages to the general ABC rejection sampler approach. Since each accepted parameter represents an *independent* draw from $p(\theta|\, \Delta(s^*, s) \leq \epsilon)$, properties of the posterior distribution are easily estimated from the accepted sample. There are no problems with such estimation due to dependence in the sample. Also, the ABC rejection sampler is simple to code and trivial to parallelize. However, the success of this method depends on how easy it is to simulate data from the model. If the model is complicated or if the acceptance rates are small, then the algorithm can be very expensive or inefficient. A low acceptance rate can be caused by a diffuse prior relative to the posterior or by a poor choice for the summary statistic. It is natural to consider approaches that do not rely upon independent sampling from the prior. In particular, one would anticipate that it would be possible to "learn" from the parameter values that have been accepted in the past to determine where good choices for future candidates θ^*.

3.3.2 Adaptive ABC Algorithms

The aforementioned challenges are the major motivations for the use of MCMC techniques: instead of relying on random draws from a distribution to produce candidates, random walks are taken in parameter space. Marjoram et al. (2003) presented an MCMC version of ABC as follows.

ABC MCMC

Initialize $\theta_i,\ i = 1$

For i=1 to i=N do:

1. Propose a move to θ^* according to a transition kernel $q(\theta_i \to \theta^*)$
2. Simulate $\mathbf{x}^* \sim p(\mathbf{x}^* \mid \theta^*)$
3. Measure s^* from $\mathbf{x}^*$
4. If $\Delta(s^*, s) \leq \epsilon$ proceed, else go to Step 1
5. Set $\theta_{i+1} = \theta^*$ with probability

$$h(\theta_i, \theta^*) = \min\left(1, \frac{\pi(\theta^*)q(\theta_i \to \theta^*)}{\pi(\theta_i)q(\theta^* \to \theta_i)}\right)$$

   and otherwise, $\theta_{i+1} = \theta_i$
6. $i = i + 1$

Here $q(\theta_i \to \theta^*)$ is a proposal density, $h(\theta_i, \theta^*)$ is the Metropolis-Hastings acceptance probability and N is the chain length. The chain length is determined after meeting some convergence criterion (see, e.g., Cowles & Carlin (1996)). As is proved in Marjoram et al. (2003), the posterior distribution of interest $\pi(\theta \mid \mathbf{x})$ is the stationary distribution of the chain.

The MCMC ABC algorithm can be much more efficient than the ABC rejection sampler, especially when the posterior and prior distributions are very different. This efficiency is gained, however, at the cost of highly correlated θ_i. Additionally, the MCMC ABC sampler can become inefficient if it wanders into a region of parameter space with low acceptance probability with a poor perturbation kernel. Successive perturbations have a small chance or being accepted and the chain can get "stuck." It is worth noting that this algorithm is replacing the likelihood ratio present in standard MCMC techniques with a one or zero based on whether or not $\Delta(s^*, s) \leq \epsilon$. This is a significant loss of resolution in the information

that was present in the likelihood ratio.

Sisson et al. (2007) (improved upon by Beaumont et al. (2009)) overcome the inefficiencies of an MCMC ABC algorithm via a method which they term *Population Monte Carlo* or SMC ABC. The SMC ABC approach adapts the SMC methods developed in Moral et al. (2006) to ABC. The algorithm learns about the target distribution using a set of weighted random variables that are propagated over iterations, similar to running parallel MCMC algorithms which interact at each iteration. The basic recipe of the SMC ABC algorithm is to initialize N points in parameter space according to $\pi(\theta)$. Points or particles are drawn from this sample, slightly perturbed, and are accepted for the next iteration if they meet the ϵ criterion. For each iteration, the tolerance ϵ is decreased, slowly migrating the N particles into the correct region of parameter space when we have reached a pre-specified tolerance threshold.

SMC ABC

Fix a decreasing sequence of tolerances $\epsilon = \epsilon_1, \epsilon_2, ..., \epsilon_T$
For the first iteration, t=1:

For i=1 to i=N do:

1. Draw θ_i^t from $\pi(\theta)$
2. Simulate $\mathbf{x}_i^t \sim p\left(\mathbf{x}_i^t | \, \theta_i^t\right)$
3. Measure s_i^t from $\mathbf{x}_i^t$
4. Proceed if $\Delta(s_i^t, s) < \epsilon_t$, else return to Step 1
5. Set $w_i = 1/N$
6. $i = i + 1$

Take τ_{t+1}^2 equal to twice the weighted variance of the set $\{\theta_i^t : i = 1, ..., N\}$.

For t=2 to t=T do:

For i=1 to i=N do:

1. Draw θ^* from $\{\theta_j^{t-1} : j = 1, ..., N\}$ with probabilities $\{w_j^{t-1}\}$
2. Generate θ_i^t from $K(\theta^*, \tau_t^2)$
3. Simulate $\mathbf{x}_i^t \sim p\left(\mathbf{x}_i^t | \, \theta_i^t\right)$
4. Measure s_i^t from $\mathbf{x}_i^t$
5. Proceed if $\Delta\left(s_i^t, s\right) < \epsilon_t$ else return to Step 1
6. Set
$$w_i^t \propto \frac{\pi(\theta_i^t)}{\sum_{j=1}^N w_j^{t-1} K\left(\tau_t^{-1}\left(\theta_i^t - \theta_j^{t-1}\right)\right)}$$
7. $i = i + 1$

Take τ_{t+1}^2 equal to twice the weighted variance of the set $\{\theta_i^t : i = 1, ..., N\}$

Here, $K(x)$ is a kernel which could be, e.g., a Gaussian kernel such that $K(x) \propto \exp\left(-x^2/2\right)$

and the weights are normalized after N points have been selected. Following Beaumont et al. (2009), each particle is perturbed using a multivariate normal distribution with mean centered on the particle's current position θ^* and variance equal to twice the weighted empirical covariance matrix of the previous iteration $N(\theta^*, \tau_t^2)$. Some work has been invested determining the most efficient method of perturbing points and includes implementing a locally adapted covariance matrix and incorporating an estimate of the Fisher information (see Filippi et al. (2011)).

Since the target distribution is approximated by a random sample of N particles that have migrated over iterations, properties of the posterior distribution are again properties of the sample, i.e., there is no covariance between the points as in the MCMC case. Using the importance weighting scheme in Beaumont et al. (2009) along with the distribution of particles in parameter space allows one to construct an estimate of the posterior distribution and derive estimates of parameters of interest based on this posterior.

SMC ABC has some distinct advantages over the other ABC methods. Both the ABC rejection sampler and the MCMC ABC scheme become very inefficient when the tolerance is small. SMC ABC derives its efficiency instead from sequentially learning about the target distribution by decomposing the problem into a series of simpler sub-problems. The sequence of ϵ's can be chosen such that the acceptance rates are never too poor and the algorithm converges at a reasonable rate. However, if the sequence of ϵ decreases too slowly the algorithm will be too computationally expensive and if it decreases too rapidly the acceptance rates will be too small. An inefficient perturbation kernel will also result in a poor exploration of the space and similarly poor acceptance rates as many simulated data sets will be generated before $\Delta(s_i^t, s) < \epsilon_t$ is reached.

ABC is an active field of research. Recent improvements have been made by Barnes et al. (2011), who employ an information-theoretical framework to construct approximately sufficient statistics and Blum & Francois (2008), who introduce a machine learning approach to estimate the posterior by fitting a nonlinear conditional heteroscedastic regression of the parameters on the summary statistics. The estimation is then adaptively improved using importance sampling. For a review and study of the improvements made in ABC methods in recent years we refer the reader to Marin et al. (2011).

3.3.3 Example: Revisited

Here, we apply SMC ABC to the stylized SN Ia inference example introduced in Section 3.2. The model is the same as was specified in that section. The "observed data" are simulated by constructing a sample of 200 SNe Ia under a flat cosmology with $\Omega_M = 0.27$ and $w = -1$. For this toy example, H_0 is assumed to be perfectly known as 72 km s^{-1} Mpc^{-1}.

Figure 27 depicts key steps in the SMC algorithm as applied to this situation. The prior is chosen to be uniform over the region $0 < \Omega_M < 1$ and $-3 < w < 0$. A collection of 500 (Ω_M, w) pairs, often called *particles* in the context of SMC methods, is migrated through the iterations of the algorithm. Figure 27a shows the collection of 500 particles at the conclusion of one of the early time steps. One of these particles is chosen at random and perturbed a small amount; the parameter combination is $\Omega_M = 0.11$ and $w = -1.21$, and is shown as the star in the plot. This parameter combination in denoted θ_i^t in the algorithm above. Simulated data are created by drawing a collection of 200 (z, z') pairs, sampling with replacement, from the collection shown in Figure 23. With θ_i^t specified and the 200 true redshifts, it is trivial to calculate the distance modulus of each SN Ia, and then add uncertainty using a Gaussian PDF with variance $(\sigma_{\mu,i})^2 = 0.04$. Figure 27b shows the resulting simulated distance moduli plotted against the photometric redshifts z. The point is that this is a plot that can be created using observable data: these data comprise the $\mathbf{x}_i^t$ that appear in the algorithm above.

A key step in any implementation of SMC ABC is the choice of the summary statistic. Here, the summary statistic s_i^t is found by applying a non-parametric regression smoother through these data; this curve is shown in Figure 27b. (The approach used to perform this smooth is briefly presented in the Appendix.) The motivation for this choice is as follows: as stated above, ideally we would choose a sufficient statistic as our summary statistic. A sufficient statistic is a summary that separates out from the full data that portion which is useful for estimating θ. In this case, we know that the relationship between redshift and distance modulus for fixed θ is a smooth curve. The deviation of the data from a smooth curve can be solely attributed to random error in the measurements, error which is not all informative of the value of θ. For this reason, it is reasonable to believe that a smoothed

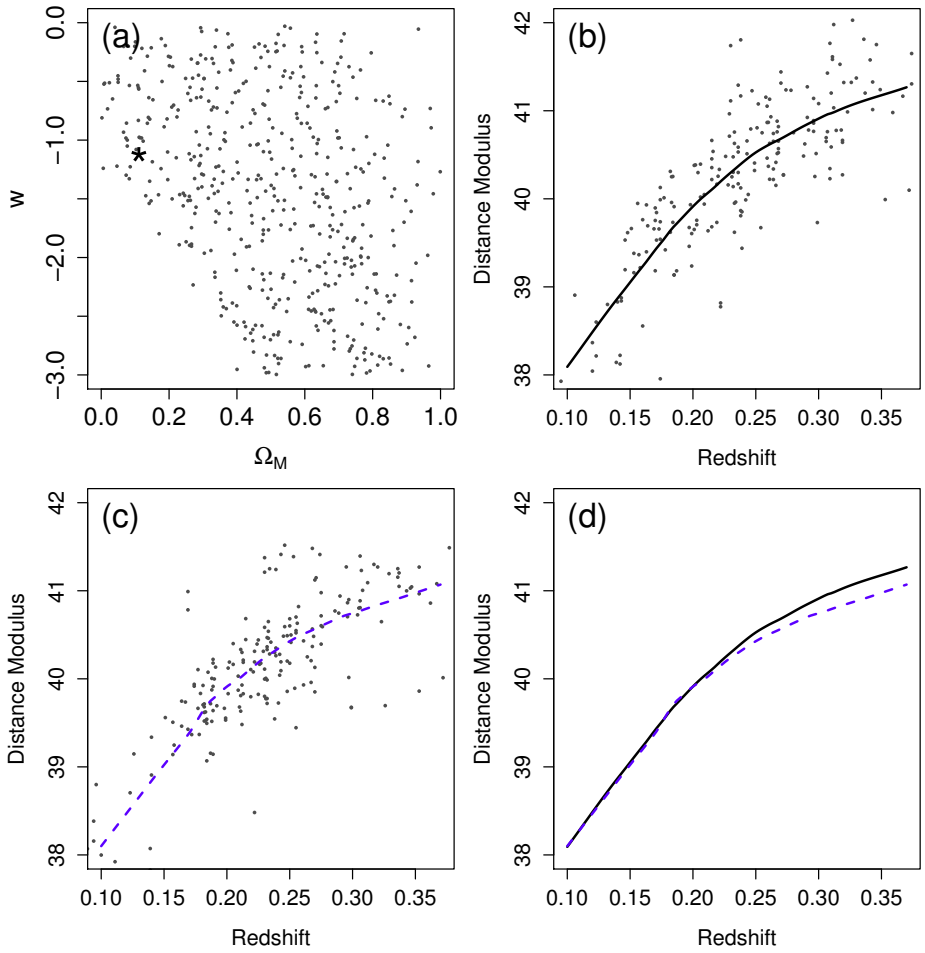

Figure 27 Illustration of key steps of the SMC ABC algorithm in the example. Panel (a): a collection of 500 particles plotted in the relevant parameter space from an intermediate iteration of the SMC ABC algorithm. A random particle is selected, plotted as the star, and perturbed a small amount. Panel (b): the simulated data set corresponding to the perturbed particle from panel a. The line is a non-parametric smooth of the data and represents the summary statistic. Panel (c): "Observed" data. The dashed line represents a non-parametric smooth of the observed data. Panel (d): a comparison between the simulated and observed data sets via the sum of squared deviations across the length of the curve. The particle is accepted in this iteration even though the curves are discrepant at high redshift as the tolerance is not small enough to reject it. Such a point would likely be rejected in a future iteration as the tolerance is decreased (see Figure 28).

version of the points shown in Figure 27b captures all of the useful information for estimating θ.

The comparison between the real and simulated data will be done via these smooth curves. Figure 27c shows the observed data, along with the result s of applying the same smoothing procedure to these data. Finally, in Figure 27d, these two curves are compared via a simple distance calculation between these curves, namely, the sum of squared deviations across the length of the curve. The particle is accepted in this iteration, because even though the curves differ at high redshift, the tolerance is not sufficiently small yet to reject at this difference. Figure 28 shows how the collection 500 particles evolves over the steps of the algorithm. As the steps progress, the particles converge in and approximate a sample from the posterior. The notable feature of this result is that this posterior is centered on the solid contours. Just as in Figure 26, these contours represent the posterior as derived by someone who had full knowledge of the redshifts. It is clear that by avoiding the unjustified Gaussian assumptions made in Section 3.2, the bias that was present in the previous posterior based on photometric redshifts has been removed.

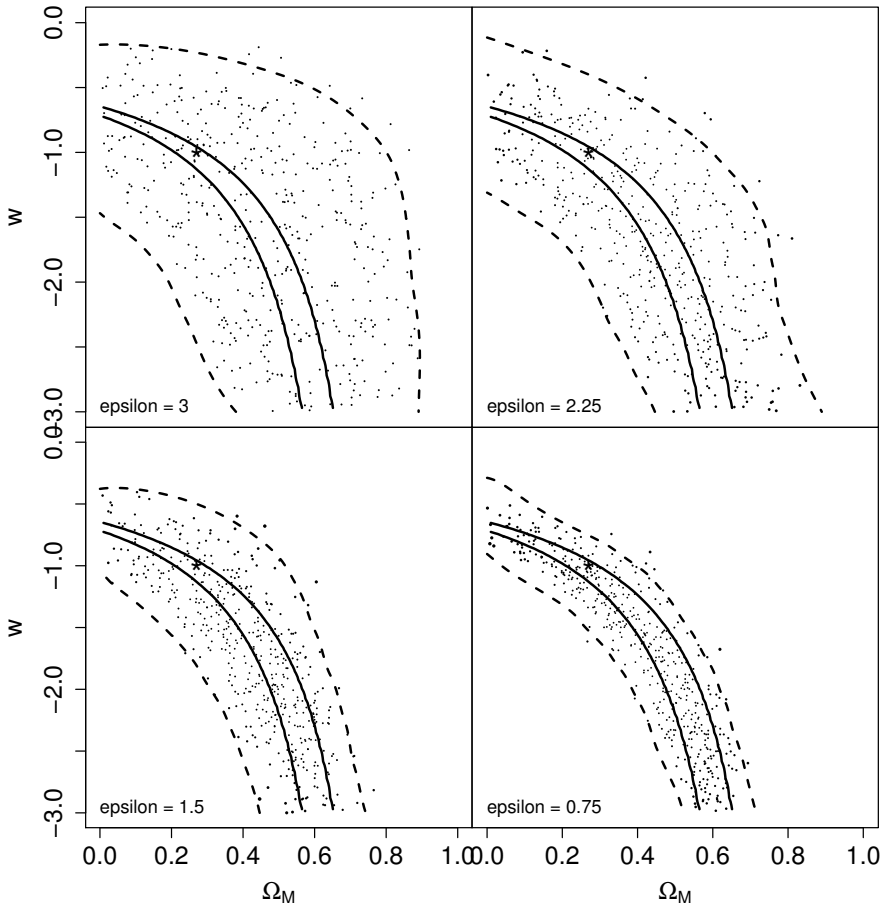

Figure 28 Progress of the ABC SMC algorithm in estimating the posterior distribution for the toy example. As ϵ decreases, the collection of particles converges to a sample from the posterior (when the weights are taken into account.) The solid contour is the 95% credible region that would have been formed by someone who had knowledge of the spectroscopic redshifts. The dashed contours result from fitting to the output of the ABC algorithm. Compare with Figure 26 to note the reduction of the bias that resulted from the Gaussian approximation. Note that it is not expected that these contours will be the same, as the ABC simulations are built upon data using photometric redshifts; hence, there is additional uncertainty in the parameter estimates.

3.4 SMC ABC COSMOLOGY WITH SDSS-II SUPERNOVAE

In this section we apply SMC ABC to first year data from the SDSS-II Supernova Survey (Holtzman et al., 2008; Kessler et al., 2009a). The development of the sophisticated supernova simulation and analysis software SNANA (Kessler et al., 2009c) has made possible the comparison between the SDSS-II supernova sample and simulated data sets and is a natural first choice to test ABC methods in cosmology. The purpose of this section is to demonstrate that ABC can be used to estimate an accurate posterior distribution. We use the spectroscopically confirmed sample to estimate cosmological parameters from assuming a spatially flat universe and a constant dark energy equation of state parameter, w. In this section we discuss how we create simulated data sets, our ABC setup, and compare our posterior distributions for the matter density Ω_M and the equation of state parameter w with those from a χ^2 analysis using statistical errors only. We close this section demonstrating the full utility of ABC by including Type IIP supernovae contamination to the SDSS sample and estimating the correct posterior distribution with ABC.

3.4.1 Simulation Setup

For this analysis we will use data from the fall 2005 SDSS-II Supernova Survey which were published in Holtzman et al. (2008). For detailed information regarding the scientific goals and data processing for the survey we refer the reader to Frieman et al. (2008), to Sako et al. (2008) for details of the supernova search algorithms and spectroscopic observations and to Section 2 of Kessler et al. (2009a) for a brief summary of the survey.

Our goal is to compare the derived posterior distributions for Ω_M and w using ABC with those from Kessler et al. (2009a) which were done using a more traditional χ^2 analysis. To make this comparison as meaningful as possible we apply the same relevant selection cuts to the data. Therefore, defining t_0 as the time of peak brightness in rest-frame B according to MLCS2k2 such that $t - t_0 = 0$, we require for each SN Ia light curve, one measurement before peak brightness and one measurement more than 10 days after peak brightness. Additionally we require five measurements with $-15 < t - t_0 < 60$ days. These

requirements ensure adequate time sampling to yield a robust light-curve model fit. Kessler et al. (2009a) additionally require one measurement in gri with a signal-to-noise ratio greater than 5 to put a floor on the quality of data and require $P_{\rm fit} > 0.001$, where $P_{\rm fit}$ is MLCS2k2 light curve fit probability based on χ^2. This requirement is designed to remove obvious peculiar SNe Ia in an objective fashion.

All supernovae in this sample have unambiguous spectroscopic confirmation and we use photometry in g, r, and i bands. This leaves us with 103 SDSS SNe Ia. This sample is identical to Kessler et al. (2009a)'s sample A and can be taken from their Table 10.

We can broadly separate the treatment of variables in the likelihood into two categories: (1) those which are of cosmological interest and (2) nuisance parameters. One will be able to construct posterior distributions for all parameters in the first category, in this case $\theta = [\Omega_M, w]$, while sampling from the probability space spanned by the set of nuisance parameters when generating simulated data sets.

We use SNANA to simulate sets of supernovae from different cosmologies. The idea is to randomly sample from the probability distributions of each nuisance parameter every time a simulated set of supernovae is generated. If we were to fix the cosmology and simulate many data sets, the probability space spanned by the nuisance parameters should be reflected in the variance of the sets of simulated data.

Within SNANA we will use the MLCS2k2 model (Jha et al., 2007a) to simulate SN Ia light curves. We use the same modified version of MLCS2k2 that was developed and trained in Kessler et al. (2009a). In this model the observed model magnitudes corrected for Galactic extinction, K-correction, and time dilation, for each passband, X, are given by

$$\begin{aligned} \mathbf{m}_X(t - t_0) &= \mathbf{M}^0_X + \mu_0 + \xi_X \left(\alpha_X + \frac{\beta_X}{R_V} \right) A^0_V, \\ &\quad + \mathbf{P}_X \Delta + \mathbf{Q}_X \Delta^2 \end{aligned} \tag{3.16}$$

where $\mathbf{M}^0_X$ are the fiducial absolute magnitudes, μ_0 is the distance modulus, R_V and A^0_V are the host galaxy extinction parameters, and $\mathbf{P}_X$ and $\mathbf{Q}_X$ describe the change in light-curve shape as a quadratic function of Δ. Quantities that are functions of phase are in bold. $\mathbf{M}^0_X$, $\mathbf{P}_X$, and $\mathbf{Q}_X$ are estimated from a training set leaving t_0, μ_0, Δ, A^0_V, and R_V as the free parameters.

The distance modulus can be related to the luminosity distance for a flat universe with a constant dark energy equation of state parameter of $w = -1$ in the following way

$$\begin{aligned} \mu_0 &= 5 \log \left(d_L / 10\text{pc} \right) && (3.17) \\ &= 5 \log \left(c(1+z) \int_0^z \left[\Omega_M (1+z')^3 + \Omega_\Lambda \right]^{1/2} dz' \right) \\ &\quad -5 \log H_0 + 25. && (3.18) \end{aligned}$$

Note that a change in H_0 simply scales the distance modulus. It is easy to see that if one rewrites Equation 3.16 in terms of luminosity distance that a degeneracy arises between H_0 and M_V. Even if H_0 is known from some other experiment, M_V would still need to be marginalized over.

ξ_X is defined as

$$\xi_X = \frac{A_X}{A_X^0} \tag{3.19}$$

and is equal to unity at maximum light. This framework allows one to separate out the time dependence of the extinction while being insensitive to the total extinction $E(B-V)$ and the extinction law R_V.

A major advantage of MLCS2k2 is that it allows one to separate reddening resulting from dust in the host galaxy (third term in Equation 3.16) from intrinsic color variations of the supernova which are captured by Δ. The validity of this approach depends on how separable these two terms are, how well intrinsic color is predicted by light curve shape, and relies on accurate models of the distribution of extinction with redshift (Wood-Vasey et al., 2007).

To generate a simulated set of data, we assume a flat universe and choose Ω_M and w from flat priors over the range $[0, 1]$ and $[-3, 0]$ respectively. One could instead draw cosmological parameters from priors based on the SDSS detection of the baryon acoustic oscillations (Eisenstein et al., 2005) and the five-year Wilkinson Microwave Anisotropy Probe observations (WMAP-5) of the cosmic microwave background (Komatsu et al., 2009). A random supernova redshift is selected from a power law distribution given by $\frac{dn}{dz} \sim (1+z)^\beta$ where $\beta = 1.5 \pm 0.6$ (Dilday et al., 2008). Δ and A_V are then drawn from empirical distributions determined in Section 7.3 of Kessler et al. (2009a). Using the parameterization

of Cardelli et al. (1989) to describe the extinction with $R_V = 2.18$ (as determined from Section 7.2 in Kessler et al. 2009a), the MLCS2k2 light curve model can now be used to generate supernovae magnitudes which are then K-corrected using spectral templates from Hsiao et al. (2007) into observer frame magnitudes.

SNANA then chooses a random sky coordinate consistent with the observed survey area and applies Galactic extinction using the Schlegel et al. (1998) dust maps, chooses a random date for peak brightness, and selects observed epochs from actual SDSS survey observations. Noise is simulated for each epoch and filter and includes Poisson fluctuations from the SN Ia flux, sky background, CCD read noise, and host galaxy background.

The simulation allows one to add additional intrinsic variations in SN Ia properties to better match the observed scatter in the Hubble diagram. We do this by "color smearing." A magnitude fluctuation drawn from a Gaussian distribution is added to the rest-frame magnitude for each passband leading to a change in model colors of ~ 0.1 mag. SNANA also includes options to model the search efficiency of the survey.

The aforementioned selection cuts on the observed data are then applied to the simulated data. This process is done for a selected cosmology for ~ 100 SN Ia over the redshift range of $[0.02, 0.45]$, similar to the SDSS data, assuming a redshift uncertainty of 0.0005. Finally, the distance modulus is measured by performing an MLCS2k2 light curve fit assuming the same prior on A_V and Δ from which the data were simulated.

In Figure 29 we plot the distance modulus as a function of redshift for the SDSS data in blue and a simulated data set in red. For the simulated data set we assume that $\Omega_M = 0.3$ and $w = -1.0$. The simulated data have been offset by 1 mag for clarity. The distance modulus uncertainties, intrinsic scatter, and redshift distributions are similar between the simulated and observed data sets.

3.4.2 SMC ABC Implementation

To calculate the measure of similarity between the observed and simulated data sets, $\Delta(s_i^t, s)$, we turn to the Hubble diagram. In the top panel of Figure 30 we show μ versus z for our observed data and a simulated data set with $\Omega_M = 0.1$, and $w = -2.0$. A reasonable distance

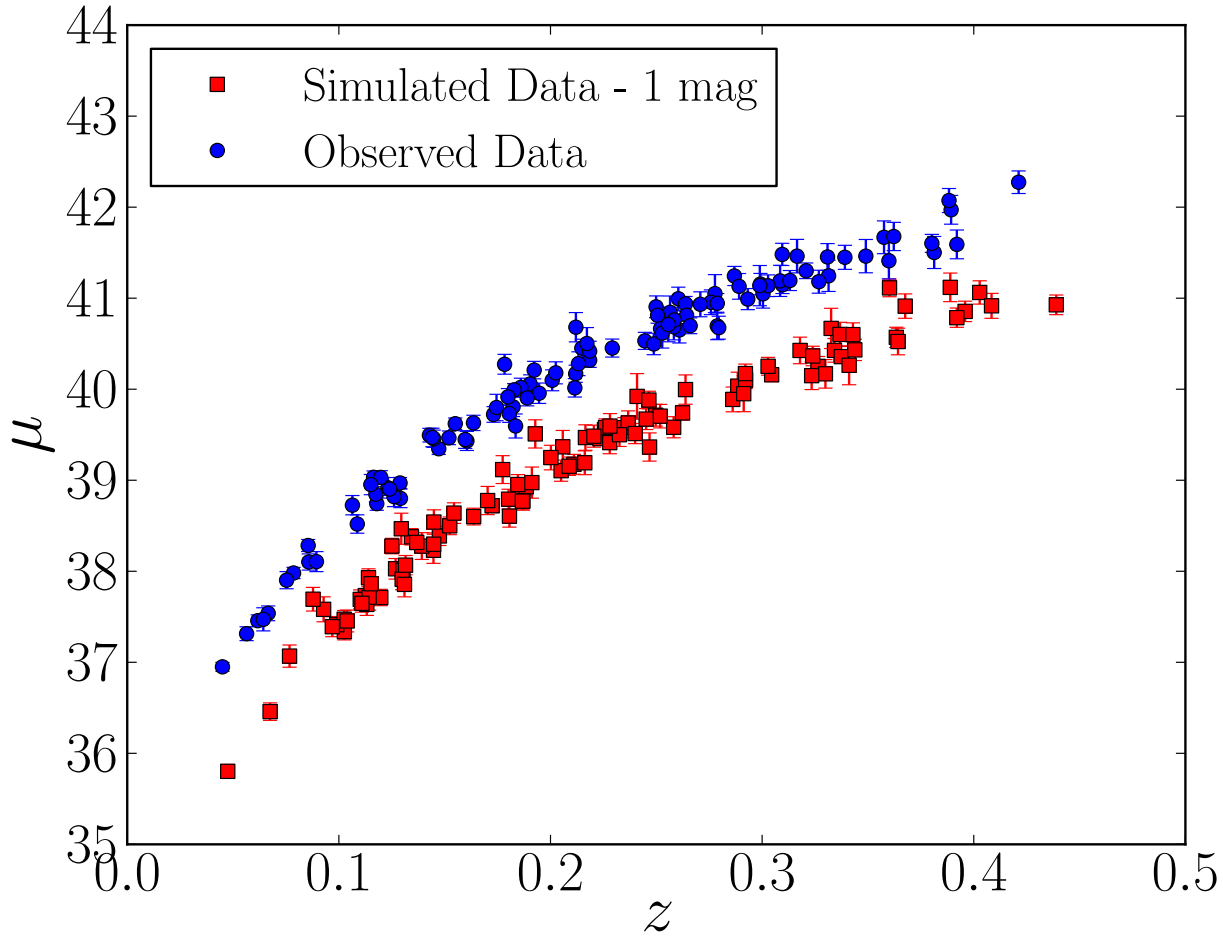

Figure 29 Hubble diagram for the observed data in blue and a simulated data set in red. The simulated data set is offset from the observed data by 1 mag and was generated assuming $\Omega_M = 0.3$ and $w = -1.0$. The distance modulus uncertainties, intrinsic scatter, and redshift distributions are well reproduced in the simulated data. Simulated data sets like this one with different cosmologies are used in our ABC analysis.

measure could be the Euclidean distance between the data sets at the redshifts of the observed data. However, in keeping with the notion of summary statistics, we would like to compare a smooth representation of the two data sets rather than the data themselves. In the bottom panel of Figure 30 we show a non-parametric smooth of the simulated and observed data. The details on how we perform the non-parametric smooth are in the Appendix B. We opt for a non-parametric smooth in the interests of efficiency and to prevent inserting additional assumptions about the data in an intermediate step in contrast to fitting the data with a cosmology fitter. We now define $\Delta(s_i^t, s)$ to be the median absolute deviation between the smoothed data sets evaluated at the observed redshifts. We choose this because it is simple, it is robust to poor smoothing at high and low redshifts, and allows for a physical interpretation of the minimum tolerance. Since we are basically measuring the distance between the two data sets in distance modulus, we consider our minimum tolerance to be equal to the median uncertainty in the smoothed observed data, i.e., we declare the observed data and simulated data sets sufficiently similar when the simulated data are within the error of the observed data.

For simplicity in this analysis we fix the value of H_0 to 65 km s^{-1} Mpc^{-1} to restrict the relevant region of parameter space. This improves the efficiency of the ABC algorithm and more importantly, makes the comparison between ABC and χ^2 more striking. However, we note that for this particular definition of the distance metric the simulated value of H_0 directly scales $\Delta(s_i^t, s)$ in a trivial manner. One could naively treat H_0 as a nuisance parameter and randomly sample H_0 from a flat prior over some range. Since H_0, w, and Ω_M are correlated, a faster approach would be to add H_0 as another cosmological parameter, adding a third dimension to the parameter space. The particles would then trace out the three-dimensional posterior distribution from which one could marginalize over H_0 to obtain the two-dimensional projection. Given the simulation expense, one would like to take advantage of the simple relationship between H_0 and $\Delta(s_i^t, s)$. To this end one could calculate a set of $\Delta(s_i^t, s)$s corresponding to a range of Hubble parameter values for a given w and Ω_M. The particle is then accepted with a percentage based on the number of $\Delta(s_i^t, s)$ elements that meet the tolerance criterion. This avoids re-simulating data sets a given number of times over a range of H_0 values while still sampling the probability space fully and thus

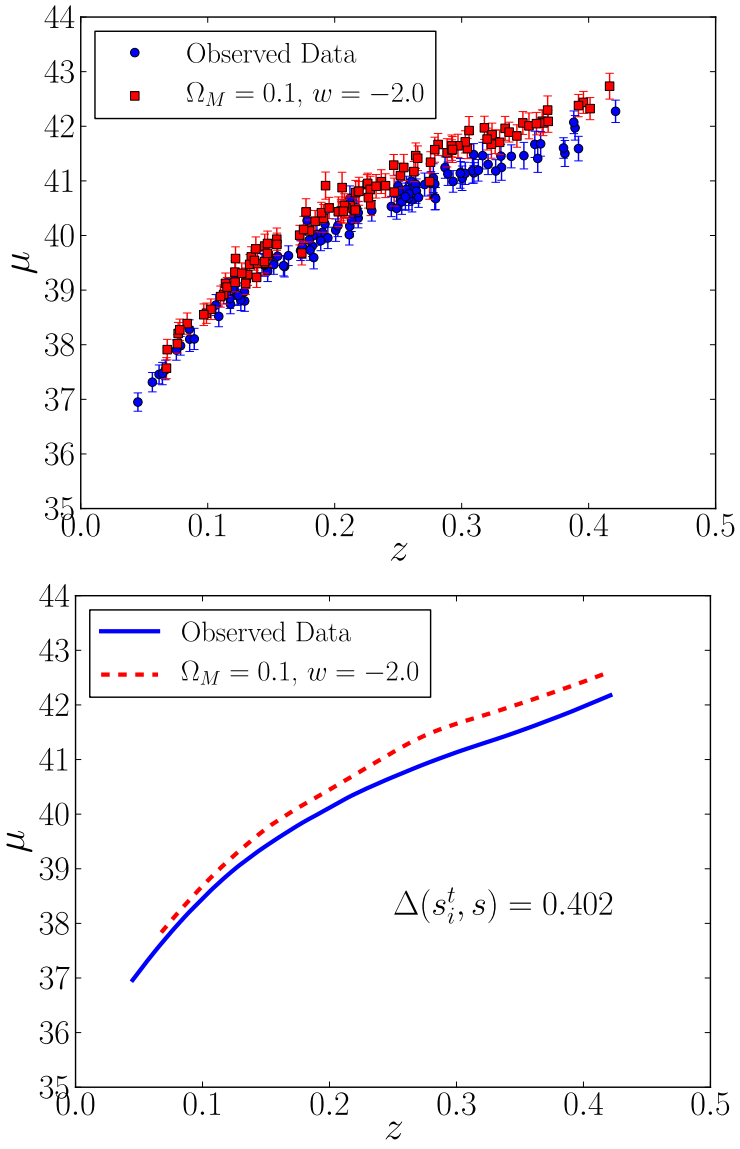

Figure 30 Illustration of the distance metric using SDSS data and simulated data from SNANA. Top: Hubble diagram for the observed data in blue and simulated data in red. The simulated data were generated assuming $\Omega_M = 0.1$ and $w = -2.0$. Bottom: non-parametric smooth of the two data sets. The distance metric is defined to be the median absolute deviation between the smoothed curves which is equal to 0.402 for this case. Our final tolerance is 0.033.

marginalizing over H_0.

We choose ϵ_t according to the distribution of $\{\Delta(s_i^{t-1}, s) : i = 1, ..., N\}$ instead of having a predefined sequence of tolerances to walk though. For the first iteration, we accept all points, i.e., the tolerance is infinite. For the next iteration, $t = 2$, the tolerance $\epsilon_{t=2}$ is set to the 25% percentile of $\{\Delta(s_i^1, s)\}$. All subsequent ϵs are the 50% percentile of the previous iteration. A percentile which is too large allows for many acceptances and will not localize into the correct region until T is large. Conversely, if one is too strict in their sequence of tolerances, many simulations are required before a point is accepted. We found that putting a stricter cut on what ϵ should be early on helps concentrate quickly into the correct area of parameter space, requiring fewer simulations in future iterations.

We define ϵ to be sufficiently small when it is less than the uncertainty on the non-parametric smooth of the observed data, which we estimate via bootstrap. The median uncertainty on the non-parametric smooth for the SDSS data set is 0.033. We require $\Delta(s_i^t, s)$ for each particle to be less than this value at the final iteration.

We choose $N = 150$ particles and run the code on eight different processors. As the initial particles are independently drawn between the three runs, the results can be combined to better estimate the posterior distribution. However, the sequence in ϵ is slightly different for each run. In practice one should parallelize the code at the level of accepting N points so that there is just one sequence of tolerances. Ours do not vary significantly and is not a concern for our demonstration.

Properties of the posterior distribution are then drawn from the final sample of particles and their weights which meet the minimum tolerance criteria.

3.4.3 Results and Discussion

It is useful to first review the cosmological analysis performed in Kessler et al. (2009a). MLCS2k2 provides an estimate of the distance modulus for each supernova. The χ^2 statistic is then calculated over a grid of model parameters and used to derive cosmological parameter estimates. Recall that $-2\ln(\pi(\theta|\,\mathbf{x})) = \chi^2$. The χ^2 statistic for the SDSS supernova sample

is calculated according to

$$\chi^2 = \sum_i \frac{\left[\mu_i - \mu_{\rm mod}(z_i|\, w, \Omega_M, H_0)\right]^2}{\sigma_\mu^2} \tag{3.20}$$

where μ_i and z_i are the distance modulus returned from MLCS2k2 and measured redshift of the supernova, and $\mu_{\rm mod}$ is the model magnitude. The distance modulus uncertainties are given by

$$\sigma_\mu^2 = \left(\sigma_\mu^{\rm fit}\right)^2 + \left(\sigma_\mu^{\rm int}\right)^2 + \left(\sigma_\mu^z\right)^2 \tag{3.21}$$

where $\sigma_\mu^{\rm fit}$ is the statistical uncertainty reported by MLCS2k2, $\sigma_\mu^{\rm int} = 0.16$ is additional intrinsic error, and

$$\sigma_\mu^z = \sigma_z \left(\frac{5}{\ln 10}\right) \frac{1+z}{z(1+z/2)}. \tag{3.22}$$

The posterior distributions for Ω_M and w assuming a flat universe can then be found by marginalizing over H_0. Recall for our comparison that we are fixing the value of H_0 and do not need to marginalize over H_0.

In Figure 31 we compare our posterior distribution to that found using the approach described above. The top plot has the particles from the final iteration of the SMC ABC algorithm. The area of the particle symbol represents the weight. These points and their weights represent a sample from the posterior distribution. We estimate the 95% credible region from this sample and compare with the 95% confidence region from a χ^2 analysis in the bottom plot. Overall the contours are well matched. The weights on the particles become large just inside the hard boundaries set by the priors on Ω_M and w. The algorithm is accounting for the fact that there is parameter space beyond the boundary which it cannot explore. This is similar to an MCMC algorithm running into a boundary and sampling more in that region because it cannot cross the boundary. As a result the ABC contours become wider than those from χ^2 near the boundaries.

We reiterate that the goal of this exercise was not to derive new cosmological constraints but merely to see how well we can recover the likelihood contours presented in Kessler et al. (2009a) using a simple implementation of SMC ABC. We demonstrate that we can recover the posterior distribution derived from current analysis techniques with the hope of convincing the reader this approach will be useful in the near future. We do note that the A in ABC

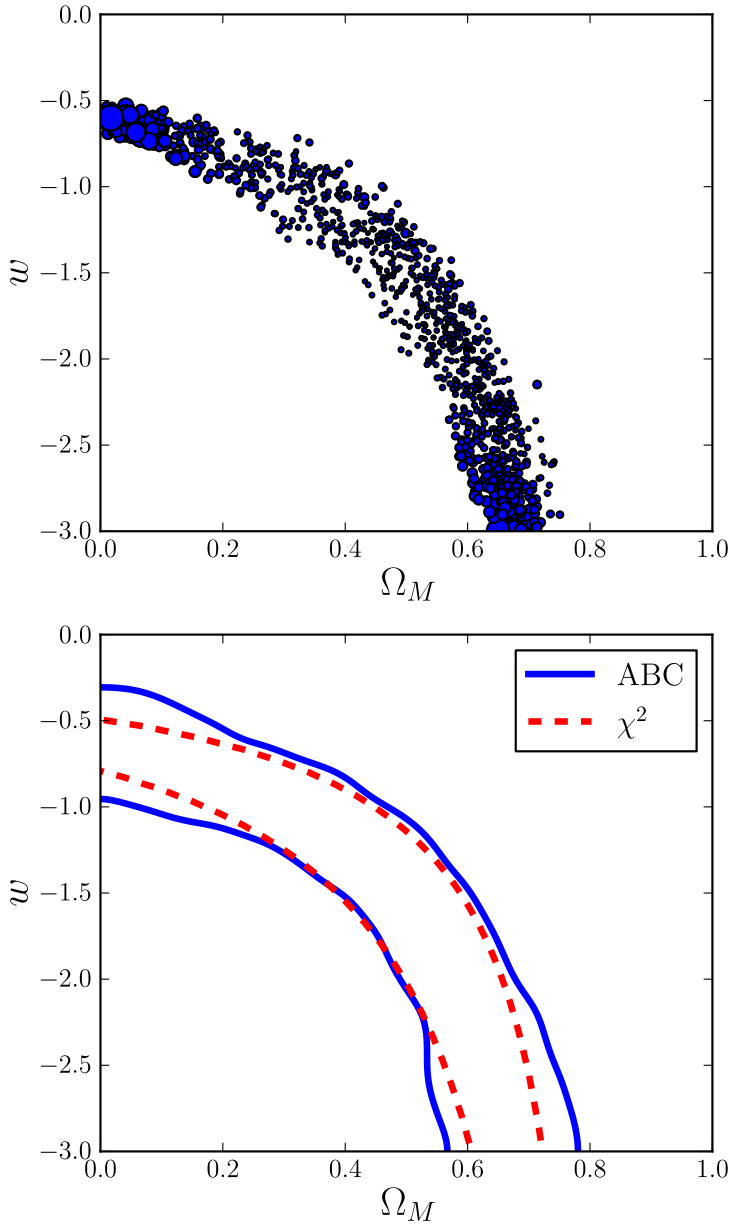

Figure 31 Comparison of SMC ABC with a χ^2 analysis. Top: particles from the final ABC iteration. Bottom: the 95% credible regions from ABC (blue-solid) and χ^2 (red-dashed). The contours between ABC and χ^2 are well matched except near the boundaries. The discrepancy results from the sharp boundaries of our prior. ABC is attempting to account for the fact that there is relevant parameter space which it cannot explore.

stands for "Approximate." One should expect slight differences in the estimated posterior distributions due to choices of distance metric, summary statistics, and final tolerance.

3.4.4 Type IIP Contamination

We add 34 simulated Type IIP supernovae to the SDSS sample so that the overall type contamination is 25%. While the amount and type are a bit extreme it is useful for illustrative purposes. We use SNANA to simulate the data which uses spectral templates and smoothed light curves of well observed supernovae. We use the "NONIa" option which computes the observer magnitudes from the spectral energy distribution and we set MAGOFF=-0.6 and MAGSMEAR=0.9. For details on these keywords and additional information on simulating non-Ia light curves we refer the reader to Section 3.5 of the SNANA manual.[8] The selection cuts, other observing parameters, and fitting procedure remain as described in Section 3.4.1. Our new sample is plotted in Figure 32.

We modify our SMC ABC analysis as follows; after drawing cosmology parameters from $\pi(\theta)$, we simulate and fit additional Type IIP light curves in the aforementioned manner and add those to our simulated Type I data. From this point the SMC ABC algorithm proceeds as before. Our new final tolerance has increased to 0.038 due to the additional scatter in the Hubble diagram.

The resulting 95% credible region is plotted in Figure 33 as the blue-solid line along with the 95% confidence regions from χ^2 with (red-dashed) and without (black-dotted) type contamination. The contours from the χ^2 analysis have shifted due to the type contamination. One can attempt to fix this bias with simulations about the best fit value but one can use SMC ABC to reproduce the full bias-correct contours. The ABC contours are 42% larger in area than the χ^2 uncontaminated contours, but cover essentially the same area as the original ABC contours from the uncontaminated sample. If contamination is properly modeled the ABC method is robust against these effects that can only be applied on a population basis rather than as a per-object correction.

It is worthwhile to note that while the division between statistical and systematic errors

[8] http://sdssdp62.fnal.gov/sdsssn/SNANA-PUBLIC/doc/snana_manual.pdf

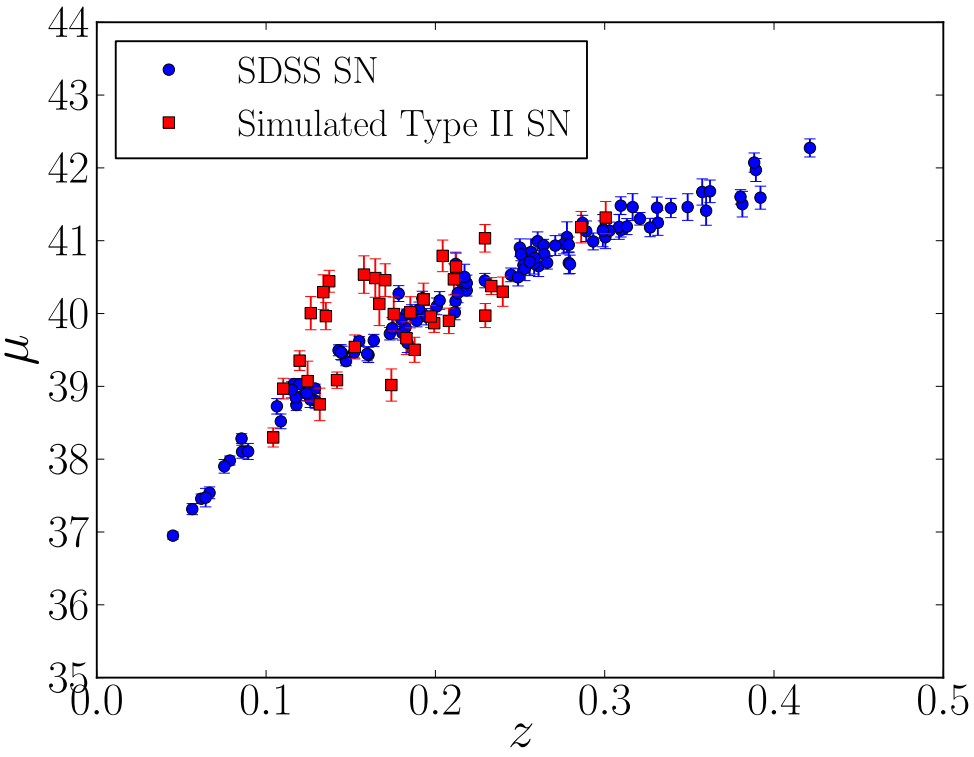

Figure 32 SDSS sample plus 34 Type IIP supernovae simulated with SNANA. This combined data set is our "observed" sample for the type contamination analysis.

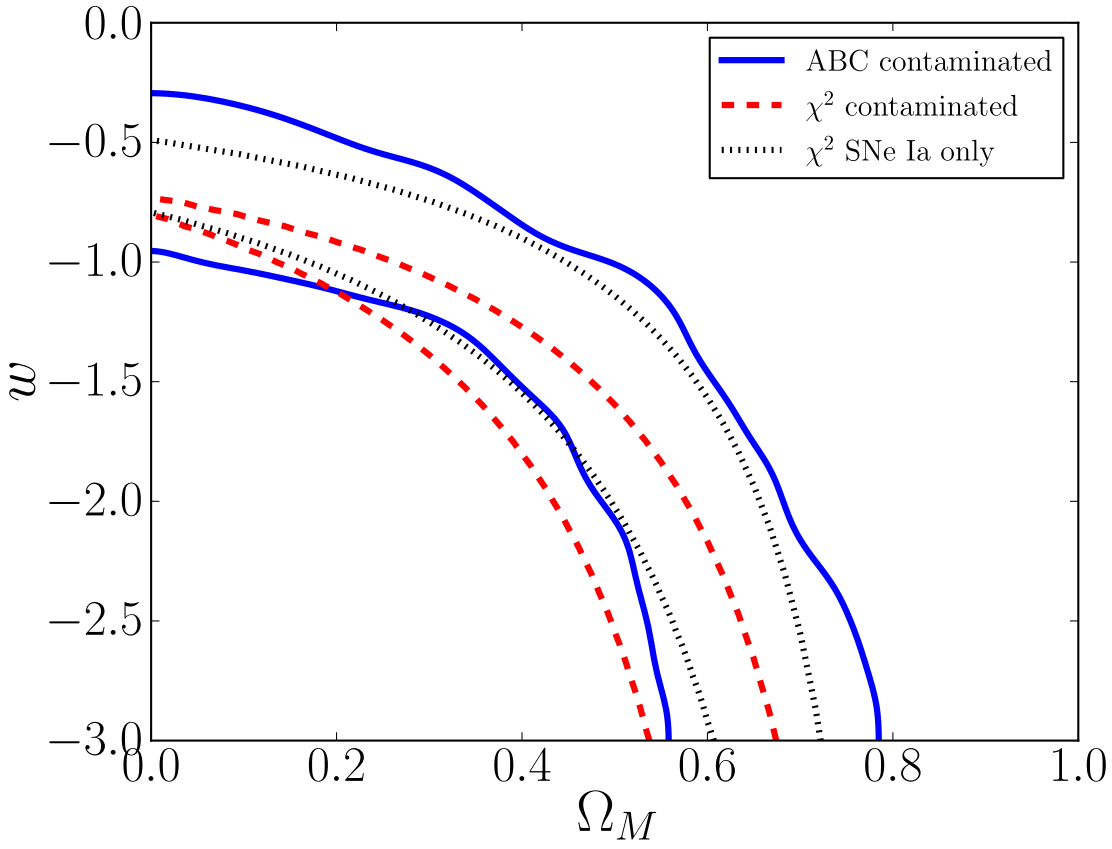

Figure 33 95% credible region from ABC (blue-solid) and the 95% confidence interval from χ^2 for the SDSS sample with type contamination (red-dashed) and the original SDSS sample (black-dotted). The type contamination biases the χ^2 result. ABC reproduces the entire credible region without this bias and reflects additional uncertainty due to increased scatter in the Hubble diagram.

is often loosely used to make a distinction between uncertainties that will decrease with more data of the same form versus uncertainties that will not decrease with larger sample sizes, the benefit of a forward-modeling framework is that they can be treated consistently and simultaneously. To create a simulation model one is forced to make choices regarding the distributions of all statistical and systematic uncertainties through either analytic or empirical methods. Systematic errors come in at least three flavors: (1) effects that we know and understand and have a reasonable understanding of the relevant input distribution; (2) effects we qualitatively understand, but for which we do not have a good input prior distribution: e.g., R_V values in host galaxies. We can compute the effect on a supernova lightcurve, but we are relatively uncertain about the correct distribution of R_V in galaxies in the Universe; (3) effects that we lose sleep over but that we have so little understanding of that we cannot model their effects at all, although we may have some purely empirical guidance: spectroscopic selection biases; evolving metallicity content of stars over the last 8 billion years. Systematic errors of type 1 are easy to include in ABC. One can use ABC to examine the effects on the posterior distribution from different choices of distributions for systematic errors of type 2. One may be able to include empirical distributions for systematic errors of type 3. Otherwise ABC can not tell you something about these systematic errors unless they are treated as model parameters. Forward modeling with an SMC ABC approach provides a powerful way to fully incorporate all available knowledge and ignorance.

3.5 FUTURE WORK

We presented here a proof of concept for an SMC ABC method to infer model parameters based on SN Ia. To fully deploy this method will require an incorporation of all data sets and modeling relative systematics between the surveys, e.g., relative calibration. This is tractable, if somewhat tedious, and has been done with varying degrees of completeness already in the literature. Extending this approach to explorations of time-variable dark energy is a simple matter of implementing at different generating model for luminosity distance as a function of redshift.

For future photometric-focused surveys, we would explore more fully the non-Gaussianity of photometric redshifts as derived from calibration samples. The probability distributions for these photometric redshifts will be strongly affected by evolution of the contamination fraction of non-SN Ia with redshift. Once that is phrased as part of the generating model, ABC will incorporate such uncertainties on the same basis as all of the other cosmological and astrophysical parameters.

The ABC+SNANA framework is a very suitable vehicle for testing the effects of different lightcurve fitters on the derived cosmological parameters. ABC will help efficiently determine what different parameter choices in the fitters should be explored.

But the real long-term goal would be to apply the summary statistic comparison at the individual lightcurve level. This could significantly reduce the computing time. The analysis presented in this work with $\sim$100 supernovae and 1200 particles required $\sim$600 CPU-hours. We estimate that a realistic problem with a sample of 10^4 supernovae could be done on $O(10)$ CPU-years, which is within reasonable computing resources. Applying the summary statistic comparison at the individual light curve level rather than in Hubble diagram space bypasses fitting the simulated light curves which currently requires most ($\sim$90%) of the computing time.

Comparing the simulated and observed data at the individual lightcurve level would also be the cleanest framework to explore agreement and evolution of systematics. The only "training" would be in the generation of the templates that the SN Ia are derived from in the first place. The cosmological distance and supernova property comparison would be finally integrated in one direct comparison.

3.6 CONCLUSIONS

We have introduced and demonstrated the use of ABC techniques to address the requirements for analyzing near-future SN Ia cosmological data sets. ABC presents a consistent and efficient approach to explore multi-dimensional non-Gaussian parameter distributions with full incorporation of systematic uncertainties.

- Forward modeling is often the only way to correctly incorporate the full range of statistical and systematic uncertainties in some of the big astronomy questions being addressed today.
- Calculation of likelihood functions for evaluation in a traditional MCMC approach may not be analytically tractable.
- ABC allows for a simultaneous exploration of parameter space and tolerance to create credible regions for physical parameters of interest without the need to construct an explicit likelihood function.
- SMC ABC offers an efficient way to explore the full parameter space of all important input parameters and model effects.
- The use of a summary statistic focuses attention directly on the ability to discriminate model parameter values in the relevant space of observed values.

We encourage scientists facing similar problems to consider the use of ABC techniques to increase their incisive power to explore the complicated parameter spaces that are surrounding the key questions in astrophysics and cosmology today.

3.7 ACKNOWLEDGEMENTS

We thank the referee for helpful comments and A.W. and M.W.-V. thank Saurabh Jha for insightful discussions. This research was supported in part by NSF DMS-1106956. A.W. and M.W.-V. were supported in part by NSF AST-1028162. A.W. additionally acknowledges support from PITT PACC and the Zaccheus Daniel Foundation.

4.0 SWEETSPOT: NEAR-INFRARED OBSERVATIONS OF THIRTEEN TYPE IA SUPERNOVAE FROM A NEW NOAO SURVEY PROBING THE NEARBY SMOOTH HUBBLE FLOW

We present 13 Type Ia supernovae (SNe Ia) observed in the rest-frame near-infrared (NIR) from $0.02 < z < 0.09$ with the WIYN High-resolution Infrared Camera on the WIYN 3.5-m telescope. With only one to three points per light curve and a prior on the time of maximum from the spectrum used to type the object we measure an H-band dispersion of spectroscopically normal SNe Ia of 0.164 mag. These observations continue to demonstrate the improved standard brightness of SNe Ia in an H-band even with limited data. Our sample includes two SNe Ia at $z \sim 0.09$, which represent the most distant rest-frame NIR H-band observations published to date.

This modest sample of 13 NIR SNe Ia represent the pilot sample for "SweetSpot" – a three-year NOAO Survey program that will observe 144 SNe Ia in the smooth Hubble flow. By the end of the survey we will have measured the relative distance to a redshift of $z \sim 0.05$-1%. Nearby Type Ia supernova (SN Ia) observations such as these will test the standard nature of SNe Ia in the rest-frame NIR, allow insight into the nature of dust, and provide a critical anchor for future cosmological SN Ia surveys at higher redshift.

4.1 INTRODUCTION

The discovery of the accelerating expansion of the Universe with SNe Ia (Riess et al., 1998; Perlmutter et al., 1999) has sparked a decade and a half of intensive SN Ia studies to pursue the nature of dark energy. High-redshift SN Ia surveys attempt to measure the equation-of-

state parameter to sufficiently distinguish among dark energy models. The majority of this work has been focused on standardizing the rest-frame optical luminosities of SNe Ia. The goal of low-redshift surveys has been to both provide the distance anchor for high-redshift relative distance measurements, and to better-calibrate SNe Ia as standard candles through an improved understanding of SNe Ia themselves.

As the amount of available SN Ia data has grown dramatically, systematic uncertainties have come to dominate cosmological distance measurements with SNe Ia (Albrecht et al., 2006b; Astier et al., 2006; Wood-Vasey et al., 2007; Kessler et al., 2009b; Sullivan et al., 2010; Conley et al., 2011). A well-established systematic affecting SNe Ia is dust reddening and extinction (see, for example, Jha et al., 2007a; Conley et al., 2007; Wang et al., 2006; Goobar, 2008; Hicken et al., 2009a; Wang et al., 2009; Folatelli et al., 2010; Foley & Kasen, 2011; Chotard et al., 2011; Scolnic et al., 2013). It is difficult to separate the effects of reddening as a result of dust from intrinsic variation in the colors of SNe Ia. Unfortunately, most observations of SNe Ia are made in the rest-frame optical and UV where reddening corrections are large.

SNe Ia are superior distance indicators in the near-infrared (NIR),[1] with more standard peak JHK_s magnitudes and relative insensitivity to reddening (Meikle, 2000; Krisciunas et al., 2004a, 2007) than in the rest-frame optical passbands traditionally used in SN Ia distance measurements. Additionally, Krisciunas et al. (2004a) found that objects that are peculiar at optical wavelengths such as SN 1999aa, SN 1999ac, and SN 1999aw appear normal at infrared wavelengths. Although it appears that the 2006bt-like subclass of SNe have normal decline rates and V-band peak magnitudes but display intrinsically-red colors and have broad, slow-declining light curves in the NIR similar to super-Chandra SNe Ia (Foley et al., 2010; Phillips, 2012).

These early results have motivated several efforts to pursue large samples of SNe Ia observed in the rest-frame NIR with 1.3–2.5-m telescopes: the Carnegie Supernova Project (CSP-I,II) (Contreras et al., 2010; Folatelli et al., 2010; Stritzinger et al., 2011; Kattner et al., 2012); Center for Astrophysics (CfA) (Wood-Vasey et al., 2008a); RAISIN (Kirshner et al., 2012). The results from these projects to date indicate that SNe Ia appear to be

[1]In this paper we use the term "near-infrared" to refer to observed wavelengths from $1 < \lambda < 2.5$ μm.

standard NIR candles to $\leq$ 0.15 mag (Wood-Vasey et al., 2008a; Folatelli et al., 2010; Kattner et al., 2012), particularly in the H band. NIR observations of SNe Ia are a current significant focus of nearby studies of SNe Ia. Recent work by Barone-Nugent et al. (2012) used 8-m class telescopes to observe 12 SNe Ia in the NIR from $0.03 < z < 0.08$ and found promising evidence that the H-band peak magnitude of SNe Ia may have a scatter as small $\sigma_H = 0.085$ mag. This work demonstrated the benefit of using larger-aperture telescopes in overcoming the significantly increased background of the night sky in the NIR.

In this paper we introduce a new effort to observe SNe Ia in the NIR in the nearby smooth Hubble flow. "SweetSpot" is a 72-night, three-year National Optical Astronomy Observatory (NOAO) Survey program (2012B-0500) to observe SNe Ia in JHK_s using the WIYN 3.5-m telescope and the WIYN High-resolution Infrared Camera (WHIRC). Our goal is to extend the rest-frame H-band NIR Hubble diagram to $z \sim 0.08$ to (1) verify recent evidence that SN Ia are excellent standard candles in the NIR, particularly in the H band; (2) test if the recent correlation between optical luminosity and host galaxy mass holds in the NIR; (3) improve our understanding of intrinsic colors of SNe Ia; (4) study the nature of dust in galaxies beyond our Milky Way; (5) provide a standard well-calibrated NIR rest-frame reference for future higher-redshift supernova surveys.

In this paper we present results from our 2011B pilot proposal. In Section 4.2 we discuss our data reduction and present light curves of 13 SNe Ia. To this sample we add data from the literature (Section 4.3) and fit the light curves using SNooPy (Burns et al., 2011). Details of how we perform the fitting are discussed in Section 4.4. We present our results, including an H-band Hubble diagram, in Section 4.5. We discuss our overall SweetSpot program strategy and goals along with future prospects for rest-frame H-band SN Ia observations in Section 4.7, and conclude in Section 4.8.

4.2 THE OBSERVATION AND PROCESSING OF THE SN IA SAMPLE

4.2.1 Observations and Sample Selection

We were awarded seven nights of NOAO time in 2011B to image SNe Ia in the NIR using the WIYN 3.5m Observatory at Kitt Peak National Observatory (KPNO) with the WHIRC detector. WHIRC (Meixner et al., 2010) is an NIR imager (0.9–2.5 μm) with a 3.'3 field of view and 0."1 pixel scale. The combination of WIYN+WHIRC allows us to observe SNe Ia out to a redshift of ~ 0.09.

Three and a half nights of this time were usable; the rest were lost to bad weather. Thus, the light curves presented here typically have only 1–3 points in each filter and are sparser than our eventual program goals of 3–10 points per light curve. Our sample (see Table 6) was selected from SNe Ia reported in the IAU Central Bureau for Astronomical Telegrams (CBET)[2] and The Astronomers Telegram (ATel)[3] that were spectroscopically confirmed as Type Ia and were in our preferred redshift range of $0.02 < z < 0.08$.

Our goal is to have the first observation in the light curve within two weeks of the maximum. We are focused on the time from 10–20 days after B-band maximum light as the most standard brightness for SNe Ia in the H-band. Our awarded time is typically scheduled around the full moon and therefore spaced 2-3 weeks apart. Additionally, there is a lack of targets at the beginning of the season until searches are up and running. When we combine weather with these factors, we find that about 30% of our light curves from 2011B have their first observation more than 14 days after maximum.

During the first two semesters of our SweetSpot survey, we were awarded more nights per semester, more nights occurring later in the semester, and had better weather. Preliminary results show that we are doing significantly better in obtaining earlier light-curve points, with only 10% of our light curves having their first observation more than 14 days after B-band maximum light.

Here we present J- and H-band light curves of the 13 of the 18 SNe Ia that were sufficiently isolated from the background light of their host galaxy. We obtained template

[2] http://www.cbat.eps.harvard.edu/cbet/RecentCBETs.html
[3] http://www.astronomerstelegram.org/

Table 6. SN Ia Properties

SN	Host Galaxy	Spectral[a] Subtype	ATel/[b] CBET	Discovery Group/ Individual	Disc./Spec.[d] Reference
SN 2011hr	NGC 2691	91T-like	C 2901	LOSS	N11, Z11b
SN 2011gy	UGC 02756	Normal	C 2871	Z. Jin, X. Goa	JG11, Z11a
SN 2011hk	NGC 0881	91bg-like	C 2892	K. Itagaki Y. Hirose	Na11, MB11b
			A 3798	PTF	GY11b
SN 2011fs	UGC 11975	Normal	C 2825	Z. Jin, X. Goa	J11, B11
SN 2011gf	SDSS J211222.69-074913.9	Normal	C 2838	CRTS	D11, M11
SN 2011hb	NGC 7674	Normal	C 2880	CRTS	H11, MB11a
			A 3739	PTF	GY11a
SN 2011io	2MASX J23024668+0848186	Normal	C 2931	MASTER	BL11, F11
SN 2011iu	UGC 12809	Normal	C 2939	Puckett	C11, MB11c
PTF11qri	LCRS B124431.1-060321	SN Ia	A 3798	PTF	GY11b
PTF11qmo	2MASX J10064866-0741124	SN Ia	A 3798	PTF	GY11b
PTF11qzq	2MASX J07192718+5413454	SN Ia	A 3798	PTF	GY11b
PTF11qpc	SDSS J122005.46+092418.3	SN Ia	A 3798	PTF	GY11b
SN 2011ha	PGC 1375631	Normal	C 2873	MASTER	LB11, O11

[a]Spectral classifications according to SNID (Blondin & Tonry, 2007) and PTF. Subtypes given when provided in the original CBET or ATEL.

[b]A:ATEL; C:CBET

[c]References/URLs: KAIT/LOSS (Filippenko et al., 2001); CRTS (Drake et al., 2009); PTF `http://www.astro.caltech.edu/ptf/`; MASTER `http://observ.pereplet.ru/sn_e.html`; Puckett `http://www.cometwatch.com`

[d]Reference Codes: N11: Nayak et al. (2011); Z11b: Zhang et al. (2011b); JG11: Jin & Gao (2011); Z11a: Zhang et al. (2011a); Na11: Nakano (2011); MB11b: Marion & Berlind (2011b); GY11b: Gal-Yam et al. (2011a); J11: Jin et al. (2011); B11: Balam et al. (2011); D11: Drake et al. (2011); M11: Marion (2011); H11: Howerton et al. (2011); MB11a: Marion & Berlind (2011a); GY11a: Gal-Yam et al. (2011b); BL11: Balanutsa & Lipunov (2011); F11: Fraser et al. (2011); C11: Cox et al. (2011); MB11c: Marion & Berlind (2011c); LB11: Lipunov & Balanutsa (2011); O11: Ochner et al. (2011)

Table 7. SN Ia Sample Summary I

Name	R.A.(J2000)	Decl.(J2000)	t_{max}[a]	z_{helio}	z from Host/SN	Redshift Citation
SN 2011hr	08:54:46.03	+39:32:16.1	55883	0.01328	Host	de Vaucouleurs et al. (1991)[b]
SN 2011gy	03:29:35.30	+40:52:02.9	55865	0.01688	Host	Falco et al. (1999)[b]
SN 2011hk	02:18:45.84	-06:38:30.3	...	0.01756	Host	Bottinelli et al. (1993)[b]
SN 2011fs	22:17:19.52	+35:34:50.0	55833	0.02091	Host	Fisher et al. (1995)[b]
SN 2011gf	21:12:24.27	-07:48:52.0	55827	0.02766	Host	Abazajian et al. (2003)[b]
SN 2011hb	23:27:55.52	+08:46:45.0	55872	0.02892	Host	Nishiura et al. (2000)[b]
SN 2011io	23:02:47.59	+08:48:09.8	55894	0.04	SN	Fraser et al. (2011)
SN 2011iu	23:51:02.27	+46:43:21.7	55894	0.04598	Host	Bottinelli et al. (1993)[b]
PTF11qri	12:47:06.28	-06:19:49.7	55897	0.055	SN	Gal-Yam et al. (2011a)
PTF11qmo	10:06:49.76	-07:41:12.3	55894	0.05523	Host	Jones et al. (2009)[b]
PTF11qzq	07:19:27.24	+54:13:48.0	55905	0.06	SN	Gal-Yam et al. (2011a)
PTF11qpc	12:20:05.47	+09:24:12.1	55902	0.08902	Host	Abazajian et al. (2005)[b]
SN 2011ha	03:57:40.87	+10:09:55.2	55842	0.094	SN	Ochner et al. (2011)

[a]Time of maximum in the B-band according to SNID/PTF reported in CBET/ATel.

[b]Heliocentric redshifts citations via NASA/IPAC Extragalactic Database (NED) http://ned.ipac.caltech.edu/.

images for the other five supernovae starting in 2012B during our main NOAO Survey program. The full host-galaxy-subtracted sample will be presented in future work. A summary of the SNe Ia presented in this work can be found in Tables 7 and 8. We describe our data processing in Section 4.2.2 and photometric analysis and calibration in Section 4.2.3.

A typical WIYN observation consisted of a 3 x 3 grid dither pattern with 30" spacing with a 60 s exposure time at each pointing. For objects or conditions requiring more total exposure time, we typically executed the dither pattern multiple times with a 5" offset between dither sets. Our observations were conducted in both J and H with priority given to H. We obtained calibration images consisting of a set of 10 dome flats with the flat lamp off and another set with the flat lamp on. We used the WHIRC "high" lamps, which are the standard KPNO MR16 halogen lamps with the reflective surface coated with aluminum by the NOAO coatings lab. We also obtained dark images for monitoring the dark behavior of the detector, but we do not use these dark images in our analysis.

Table 8. SN Ia Sample Summary II

Name	$z_{\mathrm{CMB+VIRGO}}$[a]	nobs$_J$	nobs$_H$	$m_{J,\mathrm{max}}$ [mag]	$\sigma(m_{J,\mathrm{max}})$[b] [mag]	$m_{H,\mathrm{max}}$ [mag]	$\sigma(m_{H,\mathrm{max}})$[b] [mag]
SN 2011hr	0.01453	2	2	14.352	0.220	15.022	0.200
SN 2011gy	0.01623	2	2	15.300	0.285	15.630	0.194
SN 2011hk	0.01625	2	2	...	...	...	...
SN 2011fs	0.01958	4	4	15.727	0.123	16.141	0.085
SN 2011gf	0.02626	2	3	16.814	0.020	16.841	0.010
SN 2011hb	0.02715	2	3	16.623	0.105	17.026	0.068
SN 2011io	0.04 ± 0.01	1	1	17.817	0.558	17.841	0.560
SN 2011iu	0.04475	2	2	17.640	0.232	18.005	0.169
PTF11qri	0.057 ± 0.001	2	2	18.769	0.122	18.689	0.147
PTF11qmo	0.05696	2	2	18.621	0.265	18.503	0.188
PTF11qzq	0.06 ± 0.01	1	1	19.122	0.377	18.634	0.383
PTF11qpc	0.09084	0	2	···	···	19.687	0.082
SN 2011ha	0.093 ± 0.001	1	1	19.520	0.152	20.067	0.214

[a]We follow Mould et al. (2000) to correct for the Virgo cluster and transform to the CMB using Karachentsev & Makarov (1996) and Fixsen et al. (1996).

[b]Error includes photometric and redshift uncertainty as well as uncertainty from the template used to fit the data.

4.2.2 Image Processing and Coaddition

The data were reduced in IRAF[4] following the steps outlined in the WHIRC Reduction Manual (Joyce, 2009):

1. The raw images were trimmed of detector reference pixels outside the main imaging area and corrected for the sub-linear response of the array.
2. The ON dome flats were combined; the OFF dome flats were combined; and the OFF combined dome flat was then subtracted from the ON combined dome flat to yield the pixel-by-pixel response.
3. The pupil ghost (an additive artifact resulting from internal reflection within the optical elements of WHIRC) was removed from this response using the IRAF routine `mscred.rmpupil`.

[4]IRAF is distributed by the National Optical Astronomy Observatory, which is operated by the Association of Universities for Research in Astronomy, Inc., under cooperative agreement with the National Science Foundation

4. For each target, the set of dithered science images were used to generate a median-filtered sky frame. The individual science images were then sky-subtracted and flat-fielded using these median frames.
5. The geometric distortion resulting from a difference in plate scales in the x and y coordinates and field distortion at the input to WHIRC was corrected using the IRAF routine `geotran` and the pre-computed WHIRC geometric distortion calibration from 2009 March 05[5].
6. The individual science images were stacked using the IRAF routine `upsqiid.xyget` to find the common stars in the images and create a registration database between the individual images in an observation sequence. Intensity offsets were determined from the overlap regions in the registration database and the set of individual images were combined into a composite image using the IRAF routine `upsqiid.nircombine`. An exposure map of a typical stacked observation sequence can be found in Figure 34.

Representative postage stamp images from the processed H-band composite images of our supernovae are shown in Figure 35.

4.2.3 Photometry and Calibration

We measured the detected counts of the SNe Ia and the stars in the field with aperture photometry on the stacked images using the Goddard Space Flight Center IDL Astronomy User's Library routines `gcntrd` and `aper`[6]. We used an aperture diameter of 1.5 FWHM (FWHM values were typically around 2") and measured the background in a surrounding sky annulus from 1.5 FWHM + 0."1 to 1.5 FWHM + 0."6. These counts in ADU/(60-second) equivalent exposure were converted to instrumental magnitudes $m_{\mathrm{inst},f} = -2.5 \log_{10} \mathrm{ADU}/60$ sec.

To calibrate the instrumental magnitudes, we first define a transformation between the WHIRC and the Two Micron All Sky Survey (2MASS; Skrutskie et al., 2006) systems using the following equation

$$m_f^{\mathrm{2MASS}} - m_{\mathrm{inst},f}^{\mathrm{WHIRC}} = \mathrm{zpt}_f + k_f\,(X-1) + c_f\left((m_J^{\mathrm{2MASS}} - m_H^{\mathrm{2MASS}}) - 0.5\ \mathrm{mag}\right) \qquad (4.1)$$

[5] http://www.noao.edu/kpno/manuals/whirc/datared.html
[6] http://idlastro.gsfc.nasa.gov/

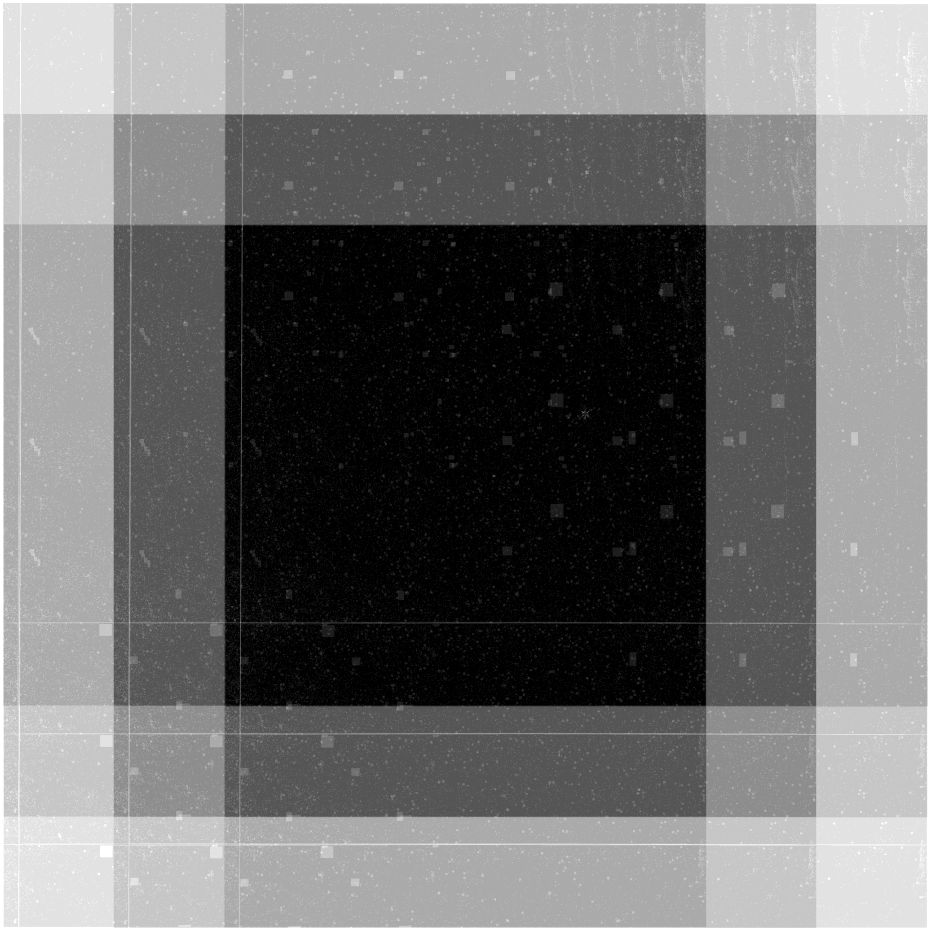

Figure 34 Exposure map of a typical WIYN+WHIRC stacked observation sequence consisting of a 3 x 3 grid dither pattern with 30" spacing with a 60 s exposure time at each pointing.

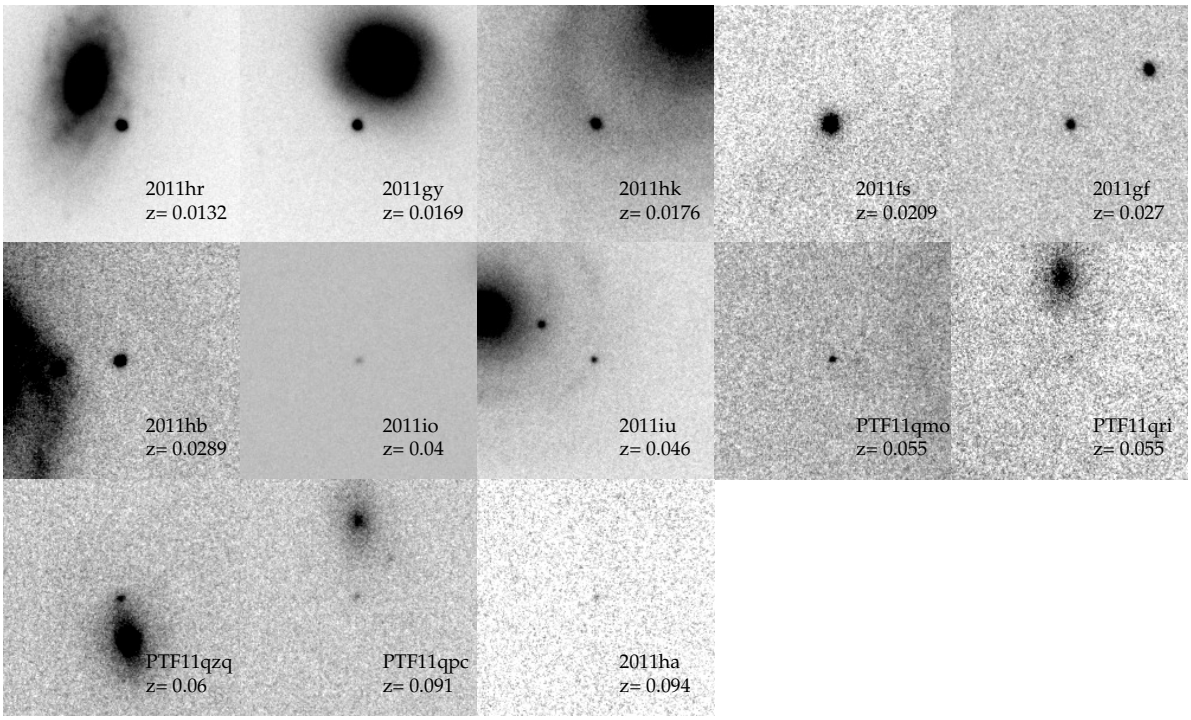

Figure 35 Postage stamps of each of the new SNe Ia presented in this work from our WIYN+WHIRC H-band stacked images. The postage stamps are in order of increasing redshift. Each image is 10" square.

Table 9. Photometric Calibration Terms

Filter	Zero Point [mag]	k [mag/airmass]	c
J	27.041 ± 0.012	-0.051 ± 0.020	$+0.062 \pm 0.035$
H	27.140 ± 0.014	-0.066 ± 0.030	-0.186 ± 0.043

where f designates the filter, X is the airmass, and the 2MASS color is compared to a reference of $m_J^{\rm 2MASS} - m_H^{\rm 2MASS} = 0.5$ mag, which represents the typical color of stars in our fields as well as SNe Ia after maximum. We then jointly solve for the zeropoint (zpt), airmass coefficient (k)[7], and color coefficient (c) using all instrumental magnitudes measured from 2MASS stars in the fields from our 2011 November 15 and 2012 January 8 nights. This procedure was performed separately for each filter following Equation 4.1.

Our fit for each filter is plotted in Figure 36 and our fit results are summarized in Table 9. We find non-zero color terms of $c_J = 0.062 \pm 0.035$ and $c_H = -0.186 \pm 0.043$ between the 2MASS and WHIRC systems, and airmass coefficients of $k_J = -0.051 \pm 0.020$ mag/airmass and $k_H = -0.066 \pm 0.030$ mag/airmass.

Matheson et al. (2012) used the same WIYN+WHIRC system to observe the very nearby SN 2011fe in M101, and used "canonical" values of $(k_J, k_H, k_{K_s}) = (-0.08, -0.04, -0.07)$ mag/airmass (in our sign convention for k). These values were based on a long-term study of k_J, k_H, and k_K at KPNO in the 1980s using single-channel NIR detectors. This effort found a range of values of $-0.12 < k_J < -0.07$ mag/airmass, $-0.08 < k_H < -0.04$ mag/airmass, and $-0.11 < k_K < -0.07$ mag/airmass with a significant seasonal variation dependent on the precipitable water vapor (R. R. Joyce and R. Probst, private communication). The filters used in these measurements were wider than the standard 2MASS filters or WHIRC filters we use here. The narrow WHIRC filters do not include some of the significant water-vapor absorption regions included in the NIR filters used in the 1980s KPNO study, and thus would reasonably be expected to have a smaller absolute value of k_J. Our determined k_J and k_H values are thus consistent with these previous results. However, the variation of k in the NIR

[7]Our sign convention for k means that k should be negative. The opposite convention is also common in the literature.

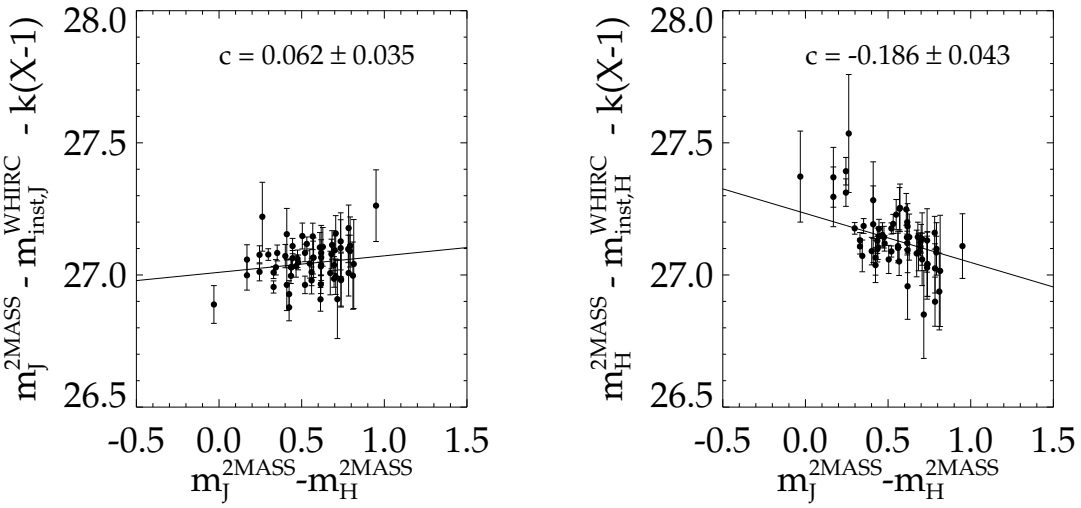

Figure 36 The difference in 2MASS magnitude and WHIRC instrumental magnitude corrected for airmass as a function of 2MASS color for the J and H filters. Fitting Equation 4.1 to these stars (over-plotted) reveals a significant color term between WHIRC and 2MASS. The results of this fit allow us to transform between the WHIRC and 2MASS system and are used to define our natural WHIRC system.

Table 10. 2MASS Calibration Stars

2MASS ID	SN Field	WHIRC Natural System				2MASS Catalog Magnitudes			
		m_J [mag]	σ_J	m_H [mag]	σ_H	m_J [mag]	σ_J	m_H [mag]	σ_H
02184937−0637528	SN 2011hk	15.162	0.021	14.384	0.029	15.022	0.045	14.408	0.047
03293834+4051347	SN 2011gy	16.640	0.025	15.883	0.040	16.565	0.102	15.827	0.122
03573901+1009372	SN 2011ha	14.570	0.015	14.119	0.021	14.592	0.033	14.117	0.041
07192306+5414071	PTF11qzq	16.788	0.022	16.060	0.042	16.725	0.127	15.915	0.145
08544039+3933230	SN 2011hr	15.526	0.015	14.923	0.023	15.587	0.054	14.903	0.070
10064485−0740334	PTF11qmo	16.325	0.022	15.570	0.038	16.376	0.109	15.583	0.099
12200392+0925144	PTF11qpc	...	...	13.728	0.021	14.482	0.036	13.779	0.043
12470715−0620106	PTF11qri	15.019	0.019	14.770	0.030	15.017	0.029	14.673	0.060
21122081−0748443	SN 2011gf	15.131	0.020	14.317	0.029	15.171	0.052	14.389	0.062
22172193+3533349	SN 2011fs	15.708	0.020	15.423	0.032	15.686	0.056	15.517	0.113
23024227+0848225	SN 2011io	15.875	0.019	15.529	0.030	15.732	0.070	15.163	0.090
23275179+0846392	SN 2011hb	15.745	0.024	15.021	0.037	15.684	0.067	14.978	0.099
23505996+4643586	SN 2011iu	15.389	0.018	14.760	0.026	15.379	0.055	14.830	0.057

as a result of water vapor strongly motivates future improvements in tracking precipitable water vapor and NIR extinction to improve the instantaneous determination of k.

We then selected a star in each field that was near the supernova and had a similar color to the supernova at the time of our observations. These reference stars are listed in Table 10. We used the best observation of the reference star, our fit results from Table 9, and Equation 4.1 to create a list of calibrated standard stars in the WHIRC natural system. We note that our only observation of SN 2011io was taken under partial clouds. For a given field, the standard star was then used to find the zeropoint for each stacked image as follows

$$\mathrm{zpt}_{f,i} = m_{\mathrm{cal},f}^{\mathrm{WHIRC}} - m_{\mathrm{inst},f,i}^{\mathrm{WHIRC}} \tag{4.2}$$

where the i subscript indicates stacked image and m_{cal} is the calibrated standard star for that field. This zeropoint was then applied to the measured instrument magnitude from the supernovae to generate the calibrated supernova magnitude in the WHIRC natural system. These light curves are presented in Table 11.

We report magnitudes in the WIYN+WHIRC natural system.[8]

[8]For reference, the filter transmissions for WIYN+WHIRC can be found at http://www.noao.edu/kpno/manuals/whirc/filters.html

Table 11: SN Ia Light Curves

Name	Date MJD	Filter	m[a] mag	$\sigma(m)$ mag	$\Delta_m^{K-\mathrm{corr}}$ [b] mag
SN 2011hr	55887.52	*J*	14.872	0.024	-0.042
SN 2011hr	55904.47	*J*	16.676	0.037	0.023
SN 2011hr	55887.52	*H*	15.056	0.036	-0.073
SN 2011hr	55904.46	*H*	15.325	0.037	-0.114
SN 2011gy	55881.50	*J*	17.036	0.040	-0.009
SN 2011gy	55904.32	*J*	18.237	0.051	-0.017
SN 2011gy	55881.47	*H*	15.879	0.045	-0.089
SN 2011gy	55904.30	*H*	16.879	0.057	-0.062
SN 2011hk	55881.36	*J*	17.572	0.024	...
SN 2011hk	55904.28	*J*	19.671	0.071	...
SN 2011hk	55881.34	*H*	17.027	0.033	...
SN 2011hk	55904.26	*H*	18.415	0.057	...
SN 2011fs	55860.31	*J*	17.209	0.038	-0.016
SN 2011fs	55881.17	*J*	17.804	0.029	-0.025
SN 2011fs	55904.12	*J*	19.087	0.045	-0.016
SN 2011fs	55935.11	*J*	19.975	0.185	0.000
SN 2011fs	55860.30	*H*	16.281	0.040	-0.072
SN 2011fs	55881.16	*H*	16.908	0.035	-0.063
SN 2011fs	55904.10	*H*	17.886	0.044	-0.063
SN 2011fs	55935.08	*H*	18.829	0.135	0.000
SN 2011gf	55860.22	*J*	18.200	0.044	-0.065
SN 2011gf	55881.08	*J*	19.004	0.046	-0.066
SN 2011gf	55860.23	*H*	17.126	0.045	-0.042
SN 2011gf	55881.07	*H*	17.917	0.052	-0.054

Continued on Next Page...

Table 11 – Continued

Name	Date MJD	Filter	m[a] mag	$\sigma(m)$ mag	$\Delta_m^{K-\mathrm{corr}}$ [b] mag
SN 2011gf	55904.07	*H*	19.081	0.188	0.000
SN 2011hb	55881.29	*J*	17.927	0.035	-0.083
SN 2011hb	55904.20	*J*	17.888	0.025	-0.072
SN 2011hb	55881.28	*H*	17.536	0.043	-0.032
SN 2011hb	55904.18	*H*	17.166	0.038	-0.034
SN 2011hb	55935.14	*H*	18.542	0.111	-0.048
SN 2011io	55904.16	*J*	19.172	0.058	-0.124
SN 2011io	55904.14	*H*	18.343	0.055	0.020
SN 2011iu	55904.24	*J*	19.096	0.033	-0.141
SN 2011iu	55935.20	*J*	18.899	0.114	-0.198
SN 2011iu	55904.22	*H*	18.612	0.038	0.047
SN 2011iu	55935.18	*H*	18.362	0.104	-0.060
PTF11qri	55904.54	*J*	19.672	0.129	-0.147
PTF11qri	55935.47	*J*	19.992	0.146	-0.268
PTF11qri	55904.52	*H*	19.402	0.301	0.027
PTF11qri	55935.45	*H*	19.224	0.251	-0.039
PTF11qmo	55904.50	*J*	19.963	0.075	-0.175
PTF11qmo	55935.42	*J*	19.966	0.163	-0.275
PTF11qmo	55904.49	*H*	19.176	0.068	0.083
PTF11qmo	55935.39	*H*	18.729	0.099	-0.058
PTF11qzq	55904.36	*J*	19.056	0.043	-0.136
PTF11qzq	55904.34	*H*	18.635	0.078	-0.065
PTF11qpc	55904.56	*H*	19.795	0.108	-0.079
PTF11qpc	55935.50	*H*	20.122	0.225	0.126

Continued on Next Page...

Table 11 – Continued

Name	Date MJD	Filter	m[a] mag	$\sigma(m)$ mag	$\Delta_m^{K-\mathrm{corr}}$ [b] mag
SN 2011ha	55881.40	J	20.434	0.130	-0.756
SN 2011ha	55881.38	H	20.627	0.191	0.018

4.3 SN IA SAMPLE FROM THE LITERATURE

To our sample of WHIRC SNe Ia we add the following data from the literature:

- A compilation of 23 SNe Ia from Jha et al. (1999), Hernandez et al. (2000), Krisciunas et al. (2000), Krisciunas et al. (2004a), Krisciunas et al. (2004c), Phillips et al. (2006), Pastorello et al. (2007b), Pastorello et al. (2007a), and Stanishev et al. (2007). This is the same set that was used as the "literature" sample by Wood-Vasey et al. (2008a). We use 22 SNe Ia from this set, one of which was observed by the CSP. We refer to the 21 SNe Ia that are unique to this sample as K+ in recognition of the substantial contributions by Kevin Krisciunas to this sample and the field of NIR SNe Ia.
- Wood-Vasey et al. (2008a) presented JHK_s measurements of 21 SNe Ia from the CfA Supernova Program using the robotic 1.3 m Peters Automated Infrared Imaging Telescope (PAIRITEL; Bloom et al. 2006) at Mount Hopkins, Arizona. We use 17 SNe Ia from this sample which we refer to as WV08.

[a]Magnitudes reported in the WHIRC natural system, which is referenced to 2MASS at $(m_J^{\mathrm{2MASS}} - m_H^{\mathrm{2MASS}}) = 0.5$ mag.

[b]K-correction as calculated by SNooPY (Burns et al., 2011). Subtract K-correction value (column 6) from reported natural-system magnitude (column 4) to yield K-corrected magnitude in the CSP system (Stritzinger et al., 2011).

- Contreras et al. (2010) and Stritzinger et al. (2011) present 69 SNe Ia from the CSP using observations at the Las Campanas Observatory in Chile (Hamuy et al., 2006). The CSP observations in $YJHK_s$ were carried out with the Wide Field Infrared Camera attached to the du Pont 2.5 m Telescope and RetroCam on the Swope 1-m telescope supplemented by occasional imaging with the PANIC NIR imager (Osip et al., 2004) on the Magellan Baade 6.5-m telescope. We use 55 SNe Ia from this sample, 6 of which are also in WV08. We refer to the 49 SNe Ia that were not observed by Wood-Vasey et al. (2008a) as CSP.
- Barone-Nugent et al. (2012) extended the rest-frame NIR sample out to $z \sim 0.08$ with 12 SNe Ia observed in JH on Gemini Observatory's 8.2m Gemini North with the NIR Imager and Spectrometer (Hodapp et al., 2000) and on ESO's 8.1m Very Large Telescope using HAWK-I (Casali et al., 2006). We use these 12 SNe Ia and refer to this set as BN12.

To arrive at these samples we removed supernovae that were reported to have a spectrum similar to the sub-luminous SN 1991bg (SN 2006bd, SN 2007N, SN 2007ax, SN 2007ba, SN 2009F); were reported to have a spectrum that was peculiar (SN 2006bt, SN 2006ot); were identified as possible super-Chandrasekhar mass objects (SN 2007if, SN 2009dc); were determined to be highly reddened (SN 1999cl, SN 2003cg, SN 2005A, SN 2006X); or were found to have a decline rate parameter $\Delta m_{15} > 1.7$ (SN 2005bl, SN 2005ke, SN 2005ku, SN 2006mr) according to the information provided in Folatelli et al. (2010); Contreras et al. (2010); Stritzinger et al. (2011); Burns et al. (2011). We also removed SN 2002cv that Elias-Rosa et al. (2008) found to be heavily obscured and SN 2007hx whose photometry is unreliable (Maximilian Stritzinger, private communication). A redshift histogram of this entire sample, which represents the currently available collection of published normal NIR SNe Ia, is plotted in Figure 37. Note that with WIYN+WHIRC we can reach out to $z \sim 0.09$ and cover the entirety of the nearby smooth Hubble flow from $0.03 < z < 0.08$.

We used the quoted system transmission function reported by each survey. For SNe Ia that were observed by multiple surveys, we fit all of the available photometry for the SN Ia.

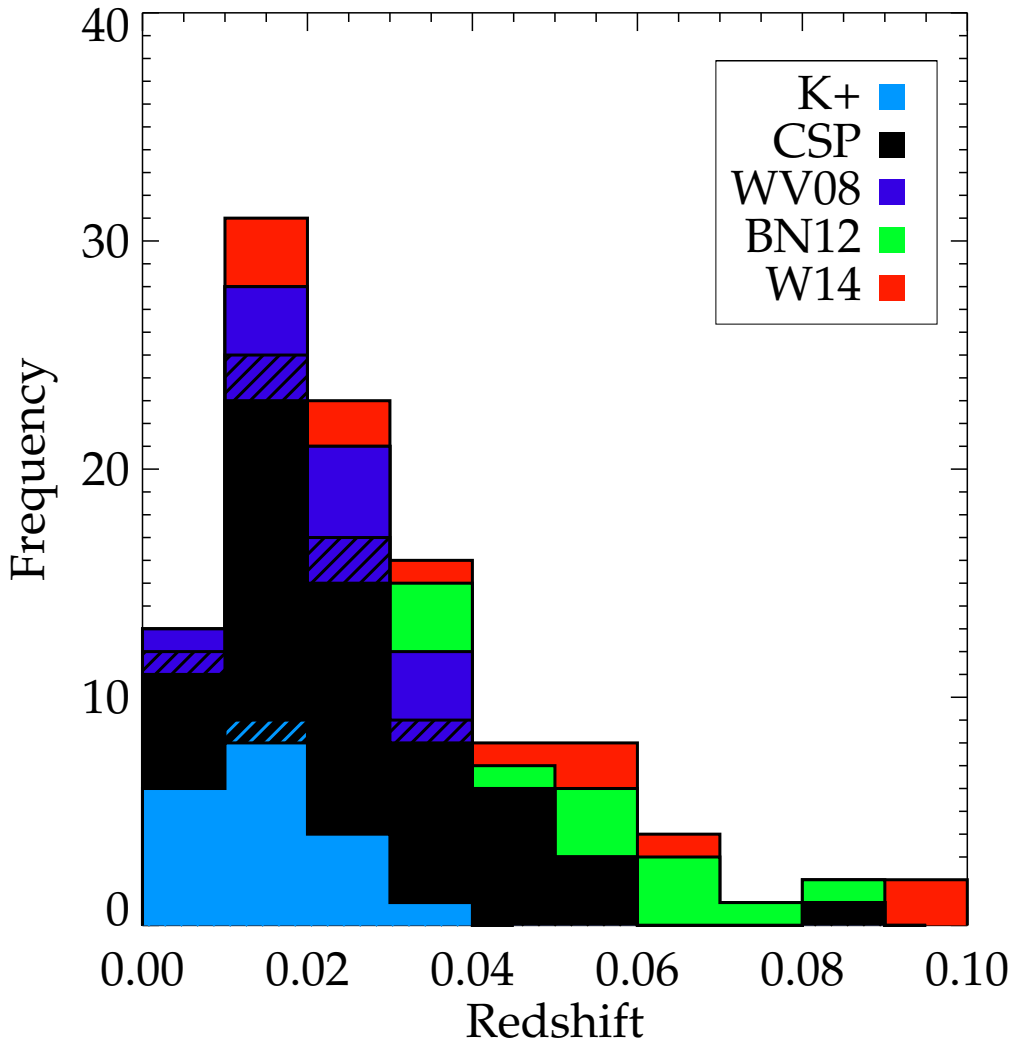

Figure 37 Cumulative distribution in redshift of supernovae from the K+ sample in cyan, Contreras et al. (2010) and Stritzinger et al. (2011) in black (CSP), Wood-Vasey et al. (2008a) in blue (WV08), Barone-Nugent et al. (2012) in green (BN12), and this present paper in red (W14). The hatched region represents SN observed by multiple groups. With WIYN+WHIRC we can probe a large redshift range and populate the NIR Hubble diagram above $z > 0.03$ where measurements of the distance-redshift relation are less affected by peculiar velocities.

4.4 ANALYSIS

We fit the light-curves using the suite of supernova analysis tools developed by CSP called SNooPy (Burns et al., 2011). We fit the data using SNooPy (version 2.0-267) "max_model" fitting that uses the following model m_X:

$$\begin{aligned} m_X(t - t_{\max}) &= T_Y((t' - t_{\max})/(1+z), \Delta m_{15}) + m_Y + R_X E(B-V)_{\rm Gal} + \\ & K_{X,Y}(z, (t' - t_{\max})/(1+z), E(B-V)_{\rm host}, E(B-V)_{\rm Gal}) \end{aligned} \quad (4.3)$$

where t is time in days in the observer frame, T_Y is the SNooPy light-curve template, m_Y is the peak magnitude in filter Y, $t_{\max}$ is the time of maximum in the B band, Δm_{15} is the decline rate parameter (Phillips, 1993), $E(B-V)_{\rm Gal}$ and $E(B-V)_{\rm host}$ are the reddening resulting from the Galactic foreground and the host galaxy, R_X is the total-to-selective absorption for filters X, and $K_{X,Y}$ is the cross-band K-correction from rest-frame X to observed Y. The free parameters in this model are $t_{\max}$, Δm_{15}, and m_Y. We do not assume any relationship between the different filters and therefore do not apply any color correction. We generate the template $T(t, \Delta m_{15})$ from the code of Burns et al. (2011) which generates rest-frame templates for J and H from the CSP data (Folatelli et al., 2010).

We use SNooPy to perform the K-corrections on all of the data using the Hsiao et al. (2007) spectral templates. We do not warp or "mangle" the spectral template to match the observed color when performing the K-corrections. A simpler approach makes sense as we are interested in measuring the peak brightness using one NIR band and a prior on $t_{\max}$. In Figure 38 we plot the H-band filter transmission for the different surveys in our sample. Overlaid are synthetic spectra at various redshifts. Note the difference in widths and up to 0.05 μm shift in the positions of the blue and red edges of the different H-band filters. While SNe Ia are standard in their rest-frame H-band brightness, there is a significant feature at 1.8 μm which moves longward of the red edge of the H-band filter quickly from just $z = 0$ to $z = 0.05$. This feature means that it is quite important to have well-understood transmission functions and spectral templates. However, given that the main effect is the feature moving across the edge of the filter cutoff, knowing the filter bandpass provides most of the necessary information without an immediate need for a full system transmission function.

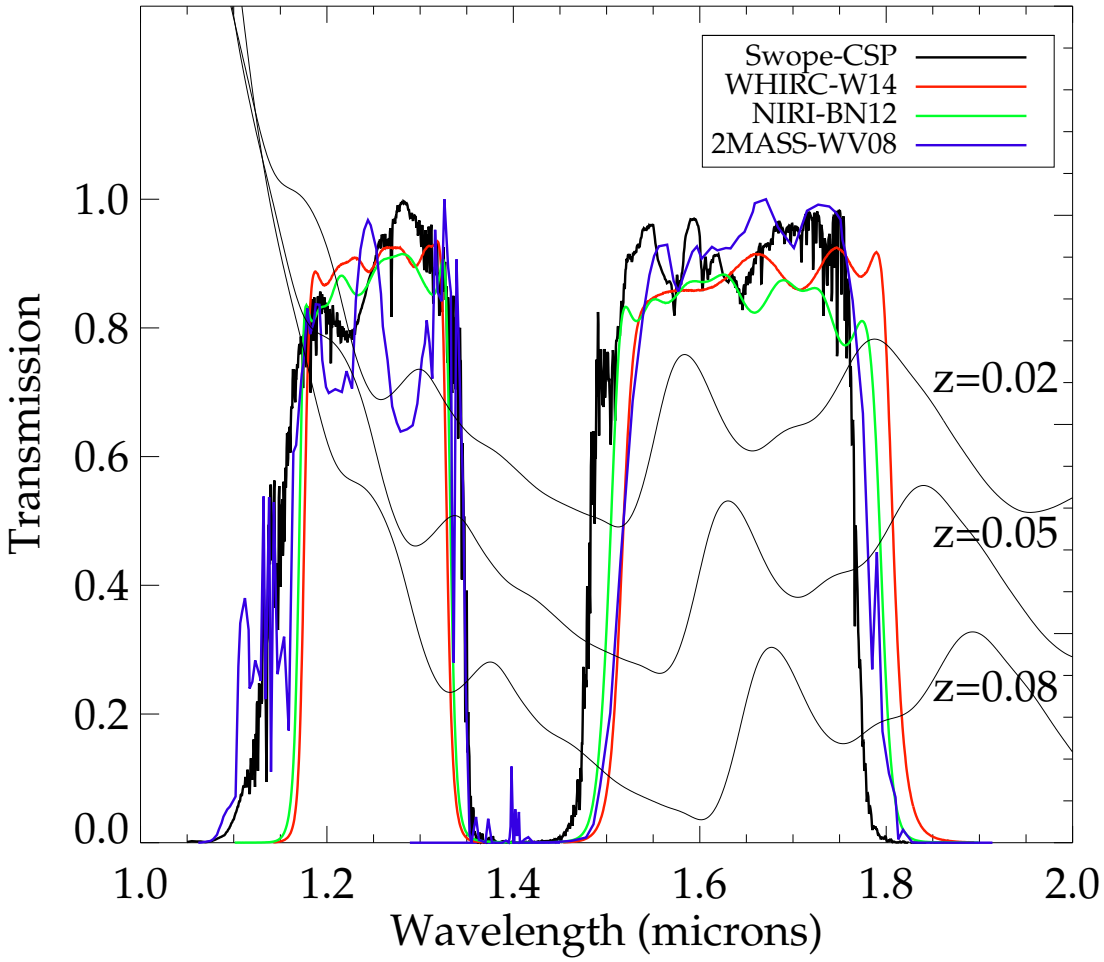

Figure 38 Filter transmission for the different instruments in our sample. The atmosphere is included in the filter transmission curve for 2MASS and Swope, but not in the ones for WHIRC and NIRI. Over-plotted is a synthetic spectrum for a Type Ia which is 30 days old from Hsiao et al. (2007) at three different redshifts. Note in particular the variation in the red edge of the filters for the different telescope+detector systems and the shifting of a significant NIR feature (rest-frame $\lambda \sim 1.75$ μm) from $z = 0.02$ to $z = 0.08$.

For the 2011B data presented in this paper $t_{\rm max}$ is fixed to an estimate measured from the spectrum as reported in the ATels/CBETs. This significant prior is necessary as our NIR data only have a few points per light curve (see Table 7), which are not enough to independently estimate $t_{\rm max}$. We also fix the light-curve width parameter to $\Delta m_{15} = 1.1$. This is reasonable as we have already eliminated SNe Ia spectroscopically identified as 91bg-like from observations in our own program and from considerations when including the current literature sample. As a result of these priors, only the peak magnitude in each filter (JH) is determined from fitting the light curve (see Table 8). The quoted peak magnitude uncertainties are then determined from least-squares fitting. The light-curve fits to each of the new SNe Ia presented here are shown in Figure 39.

In order to use a consistent method to compare the apparent brightness of the SNe Ia across our entire sample, we applied a similar process for the literature sample. We use a prior on the time of maximum for the K+, CSP, and WV08 data from the SNooPy fit to the B-band light curve alone and fixed $\Delta m_{15} = 1.1$. SN 2005ch is an exception as we do not have a B-band light curve. We fixed the time of maximum for this SN to an estimate from the spectrum reported in Dennefeld & Ricquebourg (2005). The optical light curves are not available for the BN12 data and not all SNe Ia in this sample were reported in ATels. We cannot estimate $t_{\rm max}$ for a fixed value of Δm_{15} as we have done for the other samples. Therefore, we fixed the time of maximum and stretch to that reported for these SNe Ia in Maguire et al. (2012).

The peak apparent magnitudes for the 2011B SNe Ia in JH are listed in Table 8. A summary of the light curve fit parameters - which includes the peak apparent magnitude - for the CSP, WV08, BN12, and the present W14 samples can be found in Table 12. The W14 data is the same as that in Table 8, but we include it in Table 12 for the convenience of presenting all of the Hubble diagram information in a single table.

Table 12: H-band Maximum Apparent Magnitude for Current Sample

Name	$t_{\rm max}$[a]	$z_{\rm CMB}$	$\sigma(z_{\rm CMB})$	$m_{H,\rm max}$ [mag]	$\sigma(m_{H,\rm max})$ [mag]	Reference[b]	Sample[c]
SN 1998bu	50953.4	0.0024	0.0001	11.662	0.025	J99,H00	K+
SN 1999cp	51364.2	0.0113	0.0001	14.741	0.039	K00	K+
SN 1999ee	51470.1	0.0102	0.0001	14.948	0.017	K04a	K+
SN 1999ek	51482.5	0.0176	0.0001	15.885	0.027	K04b	K+
SN 1999gp	51550.7	0.0258	0.0001	16.722	0.093	K01	K+
SN 2000E	51577.5	0.0045	0.0001	13.516	0.033	V03	K+
SN 2000bh	51634.5	0.0246	0.0001	16.541	0.054	K04a	K+

Continued on Next Page...

Table 12 – Continued

Name	$t_{\max}$[a]	$z_{\rm CMB}$	$\sigma(z_{\rm CMB})$	$m_{H,\max}$ [mag]	$\sigma(m_{H,\max})$ [mag]	Reference[b]	Sample[c]
SN 2000bk	51645.7	0.0285	0.0001	17.151	0.072	K01	K+
SN 2000ca	51667.7	0.0251	0.0001	16.556	0.048	K04a	K+
SN 2000ce	51670.6	0.0169	0.0001	15.878	0.094	K01	K+
SN 2001ba	52035.3	0.0312	0.0001	17.212	0.034	K04a	K+
SN 2001bt	52064.1	0.0144	0.0001	15.643	0.030	K04a	K+
SN 2001cn	52072.6	0.0154	0.0001	15.591	0.053	K04b	K+
SN 2001cz	52104.9	0.0170	0.0001	15.603	0.053	K04b	K+
SN 2001el	52182.3	0.0036	0.0001	12.871	0.025	K03	K+
SN 2002bo	52357.3	0.0057	0.0001	13.822	0.026	K04b	K+
SN 2002dj	52450.8	0.0113	0.0001	14.669	0.021	P08	K+
SN 2003du	52768.2	0.0074	0.0001	14.417	0.050	St07	K+
SN 2004S	53040.2	0.0100	0.0001	14.693	0.040	K07	K+
SN 2004ef	53264.5	0.0294	0.0001	17.208	0.128	C10	CSP
SN 2004eo	53278.5	0.0146	0.0001	15.692	0.043	Pa07b,C10	CSP
SN 2004ey	53304.9	0.0143	0.0001	15.672	0.022	C10	CSP
SN 2004gs	53354.7	0.0280	0.0001	17.369	0.122	C10	CSP
SN 2004gu	53366.1	0.0477	0.0001	17.995	0.071	C10	CSP
SN 2005M	53406.2	0.0236	0.0001	16.570	0.022	C10	CSP
SN 2005ag	53415.1	0.0806	0.0001	18.980	0.083	C10	CSP
SN 2005al	53430.1	0.0140	0.0001	15.749	0.064	C10	CSP
SN 2005am	53435.1	0.0097	0.0001	14.144	0.056	C10	CSP
SN 2005ao	53441.2	0.0384	0.0001	17.805	0.075	WV08	WV08
SN 2005cf	53534.0	0.0067	0.0001	13.914	0.018	WV08,Pa07a	WV08
SN 2005ch	53535.0	0.0285	0.0001	16.996	0.066	WV08	WV08

Continued on Next Page...

Table 12 – Continued

Name	$t_{\max}$[a]	$z_{\rm CMB}$	$\sigma(z_{\rm CMB})$	$m_{H,\max}$ [mag]	$\sigma(m_{H,\max})$ [mag]	Reference[b]	Sample[c]
SN 2005el	53648.2	0.0148	0.0001	15.647	0.039	WV08,C10	WV08
SN 2005eq	53655.9	0.0279	0.0001	17.159	0.042	WV08,C10	WV08
SN 2005eu	53665.8	0.0337	0.0001	17.167	0.066	WV08	WV08
SN 2005hc	53668.2	0.0444	0.0001	17.929	0.063	C10	CSP
SN 2005hj	53675.8	0.0564	0.0001	18.338	0.119	S11	CSP
SN 2005iq	53687.4	0.0323	0.0001	17.603	0.054	WV08,C10	WV08
SN 2005kc	53698.2	0.0134	0.0001	15.555	0.024	C10	CSP
SN 2005ki	53705.8	0.0211	0.0001	16.359	0.051	C10	CSP
SN 2005na	53741.3	0.0270	0.0001	16.829	0.040	WV08,C10	WV08
SN 2006D	53757.0	0.0085	0.0001	14.585	0.028	WV08,C10	WV08
SN 2006N	53759.2	0.0145	0.0001	16.132	0.118	WV08	WV08
SN 2006ac	53781.2	0.0247	0.0001	16.725	0.065	WV08	WV08
SN 2006ax	53827.5	0.0187	0.0001	15.971	0.021	WV08,C10	WV08
SN 2006bh	53833.4	0.0104	0.0001	15.058	0.059	C10	CSP
SN 2006br	53851.4	0.0263	0.0001	17.112	0.084	S11	CSP
SN 2006cp	53897.2	0.0241	0.0001	16.740	0.108	WV08	WV08
SN 2006ej	53975.1	0.0188	0.0001	16.397	0.069	S11	CSP
SN 2006eq	53971.4	0.0480	0.0001	18.564	0.292	C10	CSP
SN 2006et	53994.7	0.0210	0.0001	16.288	0.021	S11	CSP
SN 2006ev	53987.4	0.0272	0.0001	17.346	0.072	S11	CSP
SN 2006gj	53998.3	0.0274	0.0001	17.169	0.190	S11	CSP
SN 2006gr	54012.9	0.0331	0.0001	18.052	0.274	WV08	WV08
SN 2006gt	54000.1	0.0431	0.0001	18.226	0.254	C10	CSP
SN 2006hb	53997.3	0.0152	0.0001	15.828	0.107	S11	CSP

Continued on Next Page...

Table 12 – Continued

Name	$t_{\max}$[a]	$z_{\rm CMB}$	$\sigma(z_{\rm CMB})$	$m_{H,\max}$ [mag]	$\sigma(m_{H,\max})$ [mag]	Reference[b]	Sample[c]
SN 2006hx	54022.6	0.0438	0.0001	17.817	0.055	S11	CSP
SN 2006is	53996.1	0.0313	0.0001	17.016	0.219	S11	CSP
SN 2006kf	54040.4	0.0205	0.0001	16.497	0.086	S11	CSP
SN 2006le	54048.1	0.0174	0.0001	16.234	0.023	WV08	WV08
SN 2006lf	54045.7	0.0130	0.0001	15.265	0.042	WV08	WV08
SN 2006lu	54037.9	0.0548	0.0001	17.693	0.219	S11	CSP
SN 2006ob	54062.0	0.0577	0.0001	18.761	0.194	S11	CSP
SN 2006os	54064.6	0.0317	0.0001	17.326	0.052	S11	CSP
SN 2007A	54113.9	0.0160	0.0001	15.957	0.049	S11	CSP
SN 2007S	54145.4	0.0158	0.0001	15.489	0.020	S11	CSP
SN 2007af	54174.8	0.0075	0.0001	13.613	0.013	S11	CSP
SN 2007ai	54174.8	0.0324	0.0001	17.078	0.036	S11	CSP
SN 2007as	54181.3	0.0180	0.0001	16.119	0.047	S11	CSP
SN 2007bc	54201.3	0.0226	0.0001	16.514	0.056	S11	CSP
SN 2007bd	54207.6	0.0322	0.0001	17.343	0.052	S11	CSP
SN 2007ca	54228.5	0.0159	0.0001	15.666	0.029	S11	CSP
SN 2007cq	54280.6	0.0246	0.0001	16.998	0.102	WV08	WV08
SN 2007jg	54366.6	0.0362	0.0001	17.873	0.051	S11	CSP
SN 2007le	54399.8	0.0051	0.0001	13.922	0.013	S11	CSP
SN 2007nq	54396.5	0.0433	0.0001	18.008	0.141	S11	CSP
SN 2007on	54419.8	0.0060	0.0001	13.293	0.092	S11	CSP
SN 2008C	54466.6	0.0173	0.0001	16.062	0.043	S11	CSP
SN 2008R	54490.6	0.0125	0.0001	15.547	0.205	S11	CSP
SN 2008bc	54550.7	0.0160	0.0001	15.744	0.023	S11	CSP

Continued on Next Page...

Table 12 – Continued

Name	$t_{\max}$[a]	$z_{\rm CMB}$	$\sigma(z_{\rm CMB})$	$m_{H,\max}$ [mag]	$\sigma(m_{H,\max})$ [mag]	Reference[b]	Sample[c]
SN 2008bq	54564.6	0.0345	0.0001	17.523	0.129	S11	CSP
SN 2008fp	54731.7	0.0067	0.0001	13.507	0.014	S11	CSP
SN 2008gp	54779.9	0.0324	0.0001	17.359	0.082	S11	CSP
SN 2008hv	54817.6	0.0143	0.0001	15.541	0.046	S11	CSP
SN 2008ia	54813.0	0.0225	0.0001	16.477	0.066	S11	CSP
PTF09dlc	55073.7	0.0662	0.0001	18.995	0.046	BN12	BN12
PTF10hdv	55344.1	0.0548	0.0001	18.608	0.016	BN12	BN12
PTF10hmv	55351.4	0.0333	0.0001	17.534	0.018	BN12	BN12
PTF10mwb	55390.7	0.0315	0.0001	17.412	0.066	BN12	BN12
PTF10ndc	55390.3	0.0820	0.0001	19.402	0.036	BN12	BN12
PTF10nlg	55391.5	0.0562	0.0001	18.655	0.040	BN12	BN12
PTF10qyx	55426.1	0.0647	0.0001	19.125	0.024	BN12	BN12
PTF10tce	55442.0	0.0392	0.0001	18.045	0.023	BN12	BN12
PTF10ufj	55456.5	0.0758	0.005	19.307	0.035	BN12	BN12
PTF10wnm	55476.5	0.0640	0.0001	18.969	0.019	BN12	BN12
PTF10wof	55474.2	0.0508	0.0001	18.587	0.020	BN12	BN12
PTF10xyt	55490.9	0.0478	0.0001	18.477	0.099	BN12	BN12
PTF11qmo	55894	0.05696	0.0001	18.503	0.188	W14	W14
PTF11qpc	55902	0.09084	0.0001	19.687	0.082	W14	W14
PTF11qri	55897	0.057	0.001	18.689	0.147	W14	W14
PTF11qzq	55905	0.06	0.01	18.634	0.383	W14	W14
SN 2011fs	55833	0.01958	0.0001	16.141	0.085	W14	W14
SN 2011gf	55827	0.02626	0.0001	16.841	0.010	W14	W14
SN 2011gy	55865	0.01623	0.0001	15.630	0.194	W14	W14

Continued on Next Page...

Table 12 – Continued

Name	$t_{\max}$[a]	$z_{\rm CMB}$	$\sigma(z_{\rm CMB})$	$m_{H,\max}$ [mag]	$\sigma(m_{H,\max})$ [mag]	Reference[b]	Sample[c]
SN 2011ha	55842	0.093	0.001	20.067	0.214	W14	W14
SN 2011hb	55872	0.02715	0.0001	17.026	0.068	W14	W14
SN 2011hr	55883	0.01453	0.0001	15.022	0.200	W14	W14
SN 2011io	55894	0.04	0.01	17.841	0.560	W14	W14
SN 2011iu	55894	0.04475	0.0001	18.005	0.169	W14	W14

[a] $t_{\max}$ from B-band optical light curve fits using SNooPy for WV08 and CSP and reported B-band $t_{\max}$ from Maguire et al. (2012) for BN12.

[b] Reference codes J99: Jha et al. (1999); H00: Hernandez et al. (2000); K00: Krisciunas et al. (2000); K04a: Krisciunas et al. (2004a); K04b: Krisciunas et al. (2004c); Ph06: Phillips et al. (2006); Pa07a: Pastorello et al. (2007b); Pa07b: Pastorello et al. (2007a); St07: Stanishev et al. (2007); WV08: Wood-Vasey et al. (2008a); C10: Contreras et al. (2010); S11: Stritzinger et al. (2011); BN12: Barone-Nugent et al. (2012); W14: this present paper.

[c] Sample name used for the divisions in the analysis. Some SNe Ia were observed by multiple projects. We assign each SNe Ia to a single sample for the purposes of quoting dispersions and distributions in the analysis.

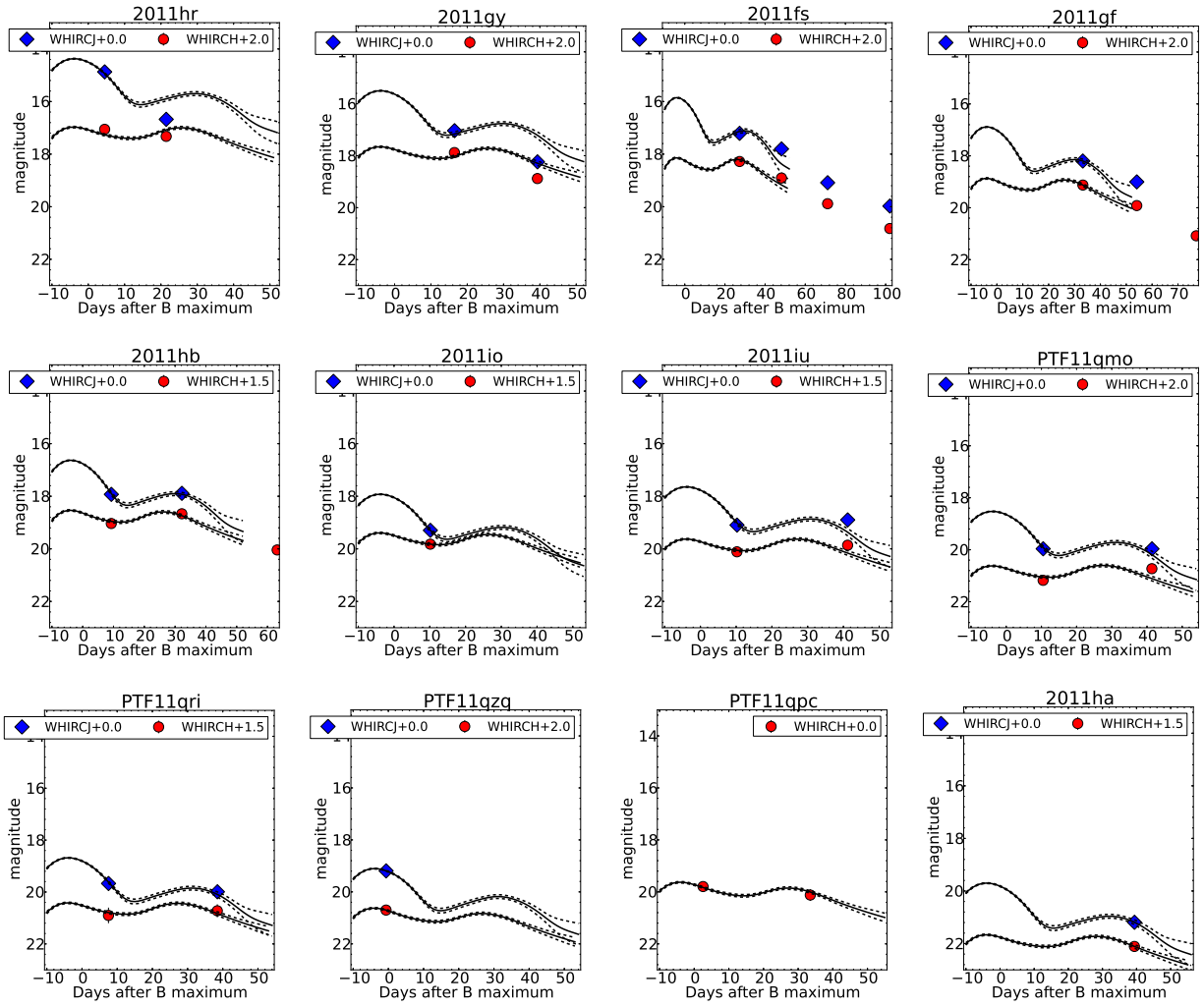

Figure 39 SNooPy light-curve fits for our 12 normal SNe Ia to our H-band (red circle) and J-band (blue diamond) data. H-band is offset for clarity. For these fits the time of maximum was fixed to the value estimated from the spectrum that was used to type the event and was reported in an ATel or CBET. The decline-rate parameter is also fixed to $\Delta m_{15} = 1.1$ making apparent magnitude the only free parameter in the fit. SN 2011hk is not included because it was spectroscopically classified as a sub-luminous supernova similar to SN 1991bg.

4.5 RESULTS

4.5.1 Near-Infrared SN Ia Hubble Diagram

An H-band Hubble diagram for our entire sample is presented in Figure 40. The recession velocities are based on the Virgo infall model of Mould et al. (2000) (see Table 7). For SNe Ia within 3000 km s^{-1} we fix the redshifts to those summarized in Wood-Vasey et al. (2008a). The solid line in the top panel of Figure 40 represents the observed apparent magnitude assuming a standard, flat cosmology of $\Omega_M = 0.28$ and $H_0 = 72$ km s^{-1} Mpc^{-1} and $M_H = -18.32$ mag (see Section 5.2). The residuals, with respect to this line, are plotted in the bottom panel. The highest redshift outlier from CSP is SN 2005ag at $z = 0.08062$. Folatelli et al. (2010) find SN 2005ag to be a slow-decliner and therefore more luminous than a normal SN Ia, although the luminosity versus decline-rate relationship should correct for this. They also believe that this SN was at the detection limit of LOSS such that the Malmquist bias could explain its over brightness.

We plot the distribution of residuals for each sub-sample in Figure 41 for the entire set (hatched) and for $z > 0.02$ (solid). The standard deviation of the residuals, σ, for each sample and for the subsample with $z > 0.02$ is given in each subpanel. One can clearly see the smaller spread in the BN12 and W14 samples, a benefit of a higher redshift sample with reduced peculiar velocity uncertainty and photometric uncertainty.

We find a dispersion for W14 of $\sigma_H = 0.227$ mag which reduces to $\sigma_H = 0.164$ mag when we exclude SN 2011hr. SN 2011hr is 91T-like and could be expected to be over-luminous. The dispersion is further reduced to $\sigma_H = 0.138$ mag if we exclude all SN with only one H-band observation and SN 2011hr which leaves us with 8 SNe Ia.

4.5.2 Absolute H-band Magnitude of a SN Ia

We find the absolute H-band magnitude M_H by calculating the weighted mean of the difference between the peak apparent magnitude and the distance modulus evaluated at the corresponding redshift assuming a standard flat ΛCDM cosmology of $\Omega_M = 0.28$ and $H_0 = 72$ km s^{-1} Mpc^{-1}. The weight includes the additional uncertainty as a result of red-

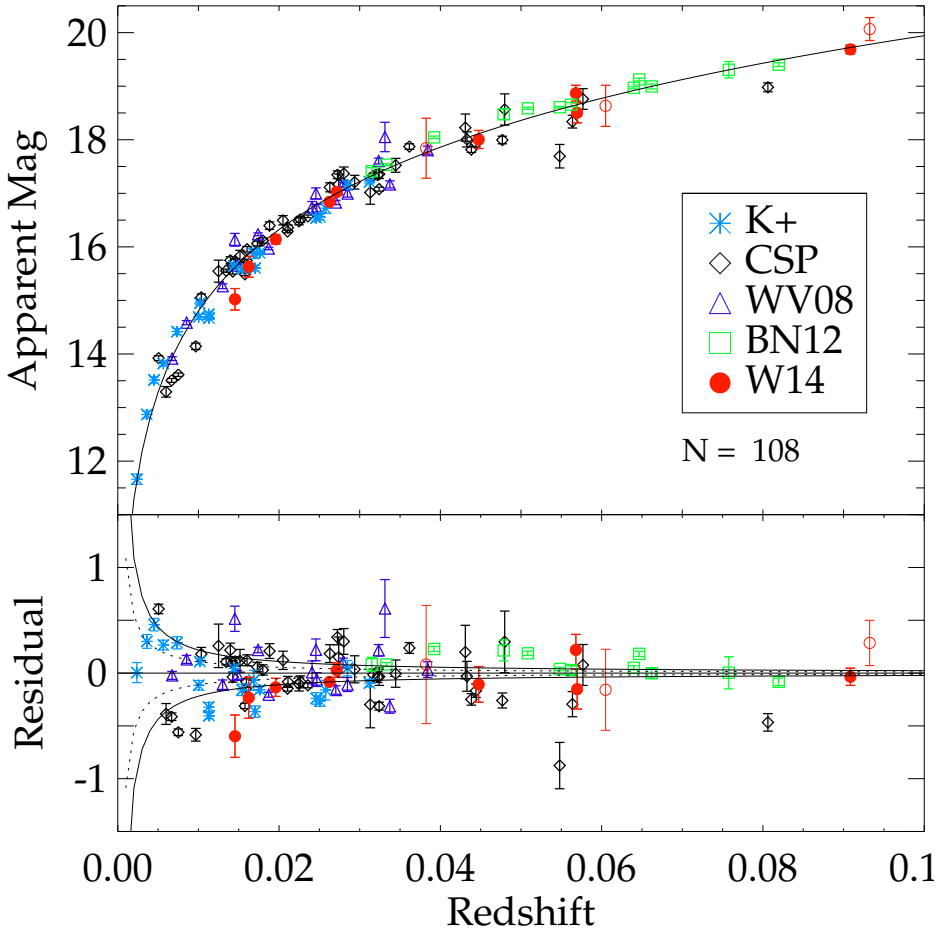

Figure 40 (Top) H-band Hubble diagram. The additional supernovae from this work (red circles) confirm the standard nature of SNe Ia in H-band and include the two farthest SNe Ia observed in rest-frame H to date. The open red circles indicate supernovae from our sample which have only one observation in their light curve. The model line plotted over the data is a standard flat ΛCDM cosmology with $\Omega_M = 0.28$. Assuming a value of $H_0 = 72$ km s^{-1} Mpc^{-1} we measure the SN Ia H-band absolute magnitude from the entire sample to be -18.314 ± 0.024 mag. (Bottom) Hubble residuals (data−model). The solid (dotted) line represents the magnitude associated with a peculiar velocity uncertainty in redshift of 300 km s^{-1} (150 km s^{-1}). Note that the largest statistical outlier from our sample, SN 2011hr, is both the lowest-redshift of our sample ($z = 0.01328$) and is also spectroscopically classified as 91T-like and could be expected to be over-luminous with respect to the assumption of a fiducial SN Ia made in our fits.

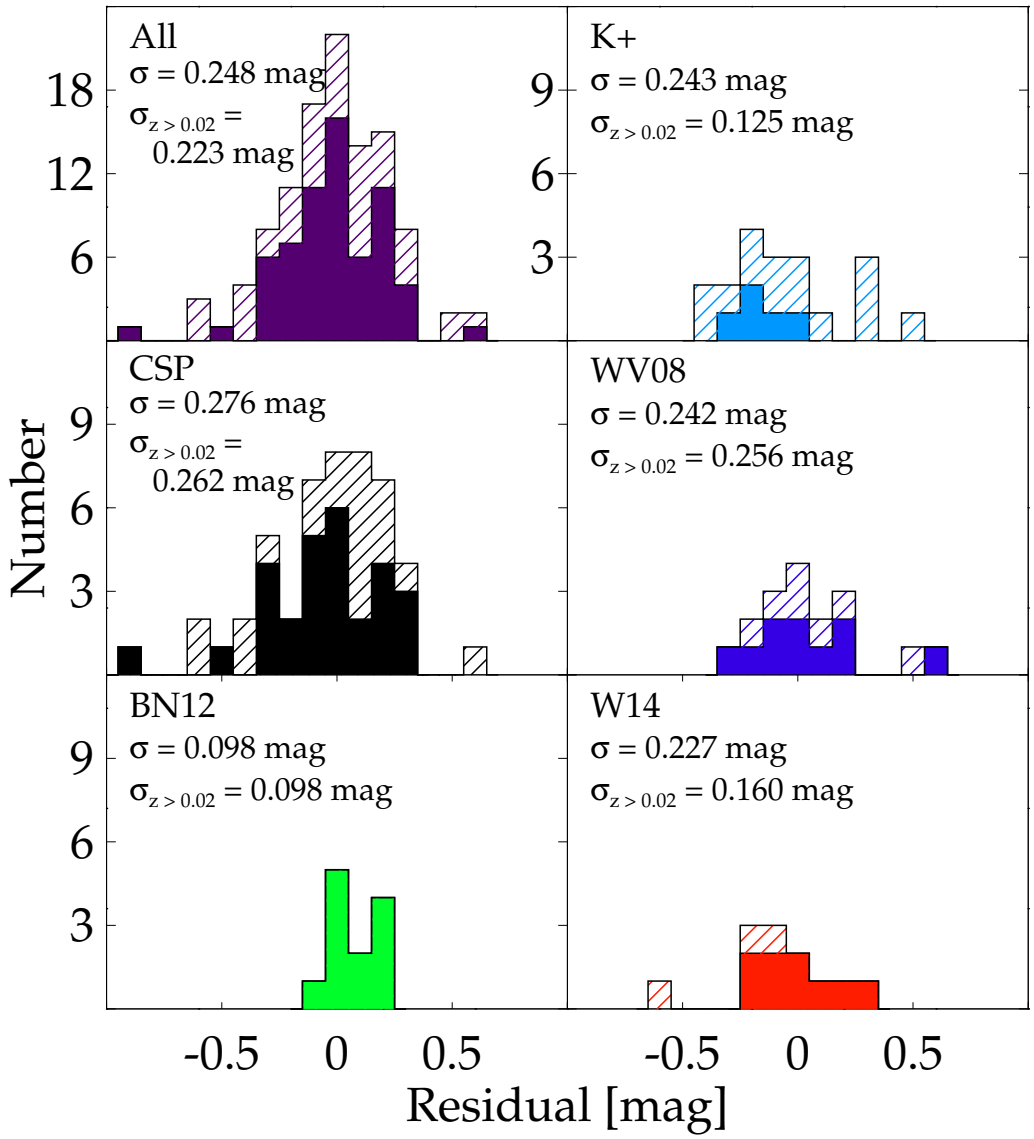

Figure 41 Distribution of the H-band residuals with respect to the global mean -18.314 ± 0.024 mag. organized by survey for the entire sample (hatched) and for SN Ia with $z > 0.02$ (solid). Supernovae observed by WV08 and CSP are included in the WV08 sample. The weighted standard deviation is quoted in the top right corner for the whole sample (top) and the higher redshift sub-sample (bottom). One can clearly see the benefit of obtaining a sample in the smooth Hubble flow by the tight BN12 residual distribution and to some extent in W14.

shift uncertainty associated with a peculiar velocity of 150 km s^{-1} (Radburn-Smith et al., 2004b). We find $M_H = -18.314 \pm 0.024$ mag for the entire sample. This value is completely degenerate with the choice of H_0, in the sense that a larger H_0 corresponds to a fainter absolute magnitude. So in more generality we find $M_H = (-18.314 \pm 0.024) + 5\log_{10}\left(H_0/(72 \text{ km s}^{-1} \text{ Mpc}^{-1})\right)$ mag.

If we analyze the measured peak H-band absolute magnitude separately for each sample we find: -18.449 ± 0.056 mag for K+, -18.376 ± 0.040 mag for CSP, -18.317 ± 0.059 mag for WV08, -18.224 ± 0.028 mag for BN12, and -18.375 ± 0.066 mag for W14 (assuming the same $\Omega_M = 0.28$, $H_0 = 72$ km s^{-1} Mpc^{-1} ΛCDM cosmology). Note that the uncertainties quoted here are the standard error (i.e., the uncertainty in the determination of the mean) rather than the standard deviation of the distribution around these absolute magnitudes (see Figure 41). The peak magnitude uncertainty quoted for each SN Ia is underestimated for at least two reasons: (1) SNooPy only returns the statistical uncertainty from fitting and does not include any systematic uncertainties[9] and (2) the time of maximum is fixed such that uncertainty in the time of maximum is not propagated to the uncertainty in peak magnitude. As a result, we cannot calculate the uncertainty in measured peak H-band absolute magnitude as the uncertainty in the weighted mean. This would underestimate the error in M_H. Instead, we look at the spread of the distribution of residuals as a whole to estimate the uncertainty and thus quote the standard error ($\sigma_H/\sqrt{N}$).

We consider a worst-case scenario to estimate the maximal contribution of uncertainty in $t_{\max}$ to the uncertainty in M_H by coherently shifting $t_{\max}$ for the entire sample by the uncertainty in $t_{\max}$. Excluding for a moment the W14 sample for which we do not have an estimate of the $t_{\max}$ uncertainty, we find that M_H shifts by 0.0017 mag indicating that the contribution from $t_{\max}$ uncertainty is negligible. If we assume an uncertainty of $\pm$ 2 days for the W14 sample we find a shift of 0.059 mag in the peak absolute brightness. This means for our sample of 12 SN Ia, the maximal contribution of $t_{\max}$ uncertainty to our estimate for M_H is $0.059/\sqrt{(12.)} = 0.017$ mag."

To examine the error in M_H incurred by fixing Δm_{15}, we refit the WV08, CSP, and K+ B-band light curves allowing $t_{\max}$ and Δm_{15} to float. We then use this $t_{\max}$ and Δm_{15} as

[9]For a list of systematic uncertainties that SNooPy fails to report see Section 4.4 of (Burns et al., 2011).

fixed priors when fitting the JH-band light curves. We find shifts in the measured peak H-band absolute magnitude of -0.031 mag, 0.019 mag, and -0.007 mag for the CSP, K+ and WV08 samples. These are well within our uncertainty on the measured peak apparent magnitude for each sample. Additionally, we find a negligible change in the χ^2 per degree of freedom between the two approaches, and thus conclude that we are justified in using the simpler light-curve model.

4.6 DISCUSSION

4.6.1 NIR SN Ia as Standard Candles

The dispersion of our W14 sample excluding SN 2011hr ($\sigma_H = 0.164$ mag) is comparable to that of Wood-Vasey et al. (2008a) who find an rms of 0.16 mag in H and Folatelli et al. (2010) who find an rms of 0.19 mag in H when not correcting for host galaxy extinction. Similar to our analysis, neither result makes a correction to the absolute magnitude according to the decline-rate.

Barone-Nugent et al. (2012) estimate that one to two points per light curve should yield a dispersion between 0.096 and 0.116 mag. However, these results derive from a sample with B-band stretch values ranging from 0.8 to 1.15. Greater diversity in our sample is one possible explanation for our larger measured dispersion. Our measured dispersion may be higher because most of our data is from +10 days after maximum and we have no pre-maximum data. Additionally, the times of maximum for our sample came from spectroscopic observations as reported in ATels and CBETs. Spectroscopic phase determinations are only precise to ± 2 days (Blondin & Tonry, 2007) and there is potentially the equivalent of a couple of days of additional scatter from quick at-the-telescope reductions.

It is possible that the spectroscopic classification and reporting of the time of B-band is systematically biased in some way. For example, while some groups report precisely the best fit spectrum used to type the object and estimate the phase, others merely state the phase as, e.g., "near maximum" or "several days after maximum." We examined the implications

of the extreme case of a coherent bias on $t_{\rm max}$ for the W14 estimate of M_H by adding and subtracting 2 days to the prior on the time of maximum to *all* W14 SNe Ia. We found that systematically shifting the time of maximum results in a shift of about +0.06 mag for +2 days and −0.06 mag for -2 days in M_H. This coherent shift in apparent magnitude for the W14 sample is because all of our data are post-maximum light where the SNe Ia are generally fading rather than increasing in brightness.

We also note that the SNe Ia which comprise the W14 sample are not drawn from the faint limits of their discovery surveys. Therefore, the Malmquist bias is unlikely to be a problem with the W14 sample.

Our analysis shows that for a set of spectroscopically normal SNe Ia using limited NIR data and a simplified light curve model which does not rely on any optical or stretch information, but rather only a prior on the time of maximum, we find an observed rms of 0.164 mag that is comparable to detailed lightcurves from optical-only surveys.

4.6.2 Absolute Brightness

Our measurement of the absolute brightness for the CSP-sample is in good agreement with the literature. Our CSP-sample results are 0.056 mag dimmer than those of Kattner et al. (2012) who find $M_H = -18.432 \pm 0.017$ mag for their CSP sample of 27 well-observed NIR light curves. The Kattner et al. (2012) analysis included a decline-rate correction. Folatelli et al. (2010) find $M_H = -18.40 \pm 0.08$ using the first set of CSP data and including no decline-rate correction, which is only 0.024 mag brighter than our analysis of the full CSP sample including up through Stritzinger et al. (2011).

We are in slight disagreement with Barone-Nugent et al. (2012) at the 1.5σ level who find $M_H = -18.30 \pm 0.04$ mag as the median absolute magnitude for their sample. [10]

We also note that while our measurements for M_H for W14, K+, CSP, and WV08 are in good agreement with each other, W14 and WV08 are in slight disagreement with the BN12 sample ($\sim 2\sigma$), and K+ and CSP are in poor agreement with the BN12 sample ($+3\sigma$).

[10]For this comparison we have adjusted the originally reported M_H values of Barone-Nugent et al. (2012) to match the common scale of $H_0 = 72$ km s^{-1} Mpc^{-1} used in this present analysis and in Folatelli et al. (2010) and Kattner et al. (2012).

Our treatment of the BN12 sample is different as we do not have access to the optical light curves. We did not determine $t_{\rm max}$ for a fixed value of stretch as we did for the other samples, but instead used the quoted $t_{\rm max}$ and stretch from Maguire et al. (2012) as was used in Barone-Nugent et al. (2012). This inconsistent treatment of this sample may be part of the discrepancy with the results of other samples. To test this, we reran the analysis on the BN12 data fixing the decline-rate parameter to $\Delta m_{15} = 1.1$ and allowing the time of maximum to float. We found $M_H = -18.248 \pm 0.030$ mag which is a marginal improvement in agreement. We speculate that additional disagreement here is caused by differences in the SNooPY (Burns et al., 2011) and FLIRT(Mandel et al., 2009) light-curve fitters.

4.7 SWEETSPOT: A 3-YEAR SURVEY PROGRAM WITH WHIRC

Building off the pilot program presented in this paper, we are currently engaged in a 3-year 72-night large-scale NOAO Survey (2012B-0500; PI: W. M. Wood-Vasey) program to image SNe Ia in the NIR using WIYN+WHIRC. Our goal is to observe $\sim$ 150 spectroscopically confirmed nearby SNe Ia in the NIR using WHIRC. We will obtain a total sample of $\sim$150 SN Ia light curves sampled in JH with 3–6 observations per light curve for the bulk of the sample and a subset of 25 SNe Ia observed in JHK_s out to late phases ($> +30$ days) with 6–10 observations per supernova. If SNe Ia are standard in the NIR with to $\sigma_H = 0.1$ mag with no significant systematic bias, then 150 SNe Ia in the nearby Hubble flow will allow us to make an overall relative distance measurement to $z \sim 0.05$ to 1%. Alternatively, we will be able to probe systematics at the few percent level, beyond what we are able to do today in the optical due to the significant confusion from host galaxy dust extinction and greater dispersion in the SN Ia optical luminosities.

We continue to rely on the hard work of several nearby supernovae surveys to discover and spectroscopically-confirm the SNe Ia we observe. Specifically, we follow announcements from the IAU/CBETs and ATels of supernovae discovered and/or classified by KAIT/LOSS (Filippenko et al., 2001), CRTS (Drake et al., 2009) surveys, the intermediate Palomar Tran-

sient Factory,[11] Robotic Optical transient search experiment,[12] the Backyard Observatory Supernova Search,[13] the Italian Supernova Search Project,[14] the La Silla Quest survey,[15] (Baltay et al., 2012) the CfA Supernova Group,[16](Hicken et al., 2012) the Public ESO Spectroscopic Survey of Transient Objects,[17] the Padova-Asiago Supernova Group,[18] and the Nearby Supernova Factory II[19] (Aldering et al., 2002).

We would be happy to work on collaborative efforts to analyze the SNe Ia we are observing with those who have optical lightcurves and spectra or other NIR data and invite those interested to contact the first two authors (A.W. and M.W.V.) to pursue such opportunities.

With this sample we will extend the SNe Ia NIR H-band Hubble Diagram out to $z \sim 0.08$. This will increase the currently published sample size in this "sweet spot" redshift range by a factor of five. The Carnegie Supernova Project II[20] is currently engaged in a similar effort to obtain optical+NIR imaging and spectroscopy for a similar sample size in this same redshift range.

While we will obtain 6–10 light curve observations for most of the SNe Ia, we will also explore constructing the "minimal" H-band Hubble diagram. NIR observations are expensive to take from the ground as a result of the significant emission and absorption from the atmosphere, and expensive from space due to the cryogenic detectors often desired. If we could determine distances reliably with just a few NIR data points combined with an optical light curve, we would significantly increase the number of SN Ia distances that could be measured for a given investment of NIR telescope time. We will realistically evaluate this "minimal" required contribution of NIR data to SN Ia cosmology by analyzing the optical light curve with only one or two H-band observations near maximum and check this against the luminosity distance determined from the actual full H-band light curve. The optical light curve will give us the phase and we will measure the brightness in the NIR. If this

[11] http://ptf.caltech.edu/iptf/
[12] http://www.rotse.net
[13] http://bosssupernova.com
[14] http://italiansupernovae.org
[15] http://hep.yale.edu/lasillaquest
[16] http://www.cfa.harvard.edu/supernova/SNgroup.html
[17] http://www.pessto.org/pessto/index.py
[18] http://graspa.oapd.inaf.it
[19] http://snfactory.lbl.gov
[20] http://csp2.lco.cl/

approach is successful it opens the window to exploring SNe Ia at higher redshift even given the significant cost of rest-frame NIR observations. We will quantify the improvement of adding one to three NIR observations per SN Ia and make recommendations for the most feasible and beneficial strategy for improving SN Ia cosmology.

If modest observations of only a few rest-frame H-band points along the lightcurves of a SNe Ia are sufficient enough to provide a robust and relatively precise distance measurement, then there is significant potential in supplementing future large, ground-based surveys, such as the Large Synoptic Survey Telescope (LSST Science Collaborations et al., 2009), with space-based resources such as the James Webb Space Telescope[21] to obtain rest-frame H-band observations to check systematic effects in these large surveys and to independently obtain reliable NIR distances to $z > 0.5$.

A newly identified systematic affecting inferred optical luminosity distances from SNe Ia is the stellar mass of the host galaxy (Kelly et al., 2010; Lampeitl et al., 2010; Sullivan et al., 2010; Gupta et al., 2011; Childress et al., 2013). These analyses show that, after light-curve shape corrections, SNe Ia in high-stellar-mass galaxies are found to be 0.1 mag brighter in rest-frame B than in low-stellar-mass galaxies. Recent work based on IFU observations of the local (1 kpc) environments of SNe Ia (Rigault et al., 2013) explains this effect as a consequence of the distribution of *local* star-formation conditions in nearby galaxies. They find that a population of SNe Ia in locally passive environments is 0.2 mag brighter than SNe Ia in locally star-forming environments. In higher-mass galaxies, there is an equal mix of these SNe Ia, leading to a 0.1 mag bias, while in lower-mass galaxies ($M_{\odot} < 10^{9.5}$) such a bright population does not appear to exist.

The NIR photometry we will obtain of the SN host galaxies will provide both reference templates for the supernova lightcurves as well as key observations to determine stellar mass. We will explore if these mass and environmental correlations hold in the NIR by combining our NIR supernova observations with samples from the literature together with observations of the host galaxies.

We will finally examine the late time color evolution of SNe Ia in the NIR. SNe Ia have a uniform optical color evolution starting around 30 days past maximum light (Lira,

[21] http://www.jwst.nasa.gov/

1996; Phillips et al., 1999). The full decay rate and color evolution from maximum light to 100 days will provide excellent calibration of the intrinsic color and dust extinction in SNe Ia. If SNe Ia are confirmed to be standard in their NIR late-time color evolution, then we can use a combined UV, optical, and NIR data set to make detailed measurements of the dust extinction in the SN Ia host galaxies.

4.8 CONCLUSION

We are using the WIYN 3.5m Observatory at Kitt Peak as part of an approved NOAO Survey to image nearby SN Ia in the NIR using WHIRC. In this paper we have presented 13 light curves for SNe Ia observed in 2011B as part of this program. Within this set we have contributed 12 new standard SNe Ia to the current nearby NIR sample out to $z \sim 0.09$.

We have presented an updated H-band Hubble diagram including the latest samples from the literature. Considering that we have late-time sparsely sampled lightcurves and a time of maximum that is accurate to a few days, it is remarkable that we measure a dispersion of our sample to be 0.164 mag when excluding 91T-like SN 2011hr. With future semesters of observing and a larger sample of SN Ia observed near maximum, we expect the dispersion to decrease as a result of more comprehensive temporal sampling. The dispersion will also improve as the optical counterparts of these SN Ia become available and the times of maximum can be more accurately determined.

4.9 ACKNOWLEDGMENTS

The observations presented in this paper came from NOAO time on WIYN under proposal ID 2011B-0482. AW and MWV were supported in part by NSF AST-1028162. A.W. additionally acknowledges support from PITT PACC and the Zaccheus Daniel Foundation. Supernova research at Rutgers University is supported in part by NSF CAREER award

AST-0847157 to SWJ. The "Latest Supernovae" website[22] maintained by David Bishop was helpful in planning and executing these observations. We thank the referee for helpful comments and the careful reading of our work. We thank Chris Burns for his significant assistance in using SNooPy. We thank Sandhya Rao for her assistance with IRAF. We thank the staff of KPNO and the WIYN telescope and engineering staff for their efforts that enabled these observations. We thank the Tohono O'odham Nation for leasing their mountain to allow for astronomical research. We thank the Aspen Center for Physics for hosting the 2010 summer workshop on "Taking Supernova Cosmology into the Next Decade" where the original discussions that led to the SweetSpot survey took place.

This research has made use of the NASA/IPAC Extragalactic Database (NED) which is operated by the Jet Propulsion Laboratory, California Institute of Technology, under contract with the National Aeronautics and Space Administration.

This publication makes use of data products from the Two Micron All Sky Survey, which is a joint project of the University of Massachusetts and the Infrared Processing and Analysis Center/California Institute of Technology, funded by the National Aeronautics and Space Administration and the National Science Foundation.

[22] http://www.rochesterastronomy.org/supernova.html

5.0 CONCLUSIONS

SN Ia data sets are expected to grow to hundreds of thousands of SNe Ia over the next decade. As a result, statistical errors on inferred model parameters from SN Ia measurements are reduced by $\sqrt{N}$ but systematic uncertainties will quickly come to dominate the error budget. For my dissertation I have applied modern statistical methods to several problems in astrophysics which rely on accurate distance measurements from SNe Ia. I here summarize the results of my dissertation and include suggestions for future directions.

- I have provided a method for modeling the local peculiar velocity field which accounts for the non-uniform sampling of objects across the sky and produces less biased model coefficients.
- I have presented an ABC method to infer cosmological parameters from SNe Ia which bypasses direct calculation of the inherently complicated likelihood function but relies on accurately simulating systematic uncertainties and nuisance parameters.
- I introduce a new NOAO survey to image SNe Ia in the NIR with the major goals of improving our ability to standardize the total luminosity of SNe Ia and provide a well calibrated sample to anchor a future, space-based survey.

Modeling the Local Peculiar Velocity Field We address a bias common to local peculiar velocity field models resulting from the non-uniform distribution of data on the sky. We model the field with spherical harmonics and employ non-parametric risk estimation to determine at which multipole to truncate the series. The minimum of the estimated risk reveals the multipole which achieves an optimum balance of variance and bias.

We show using simulations that if there is power beyond the maximum multipole used in a regression analysis, a bias is introduced on the coefficients if the data are not uniformly

distributed. One can estimate multipole coefficients without this bias by accurately modeling and accounting for the non-uniform distribution of data. This method, which we called Coefficient Unbiased, can return a more accurate measure of the e.g. dipole but sacrifices in overall accuracy of an all-sky model.

After applying non-parametric risk estimation to current SN Ia data sets we find that there are not enough data to measure power beyond the dipole. There is also no significant evidence for a monopole term, indicating that we are using consistent values of H_0 and M_V. We measure the bulk flow to be moving at 446 ± 101 km s^{-1} towards $(l, b) = (273° \pm 11°, 46° \pm 8°)$. We estimate using simulations that with $\sim$200 SNe Ia, roughly double the sample at the time of this analysis, we would be able to probe the quadrupole moment.

This analysis can be expanded to higher multipoles and to three dimensions as data sets continue to grow. Modeling the peculiar velocity field as a function of redshift would enable one to determine the redshift at which the bulk flow converges to the rest-frame of the CMB and allow one to look for a local void or Hubble bubble.

Cosmological Inference with Approximate Bayesian Computation We have demonstrated the use of ABC techniques to address the requirements for analyzing near-future SN Ia cosmological data sets when calculation of a sufficiently accurate likelihood function is no longer computationally or analytically tractable. These techniques rely on accurately forward modeling the full range of statistical and systematic uncertainties to bypass direct calculation of the likelihood. Sequential Monte Carlo ABC efficiently explores multi-dimensional parameter distributions. This method uses a summary statistic to aid in our ability to discriminate model parameter values in the relevant space of observed values.

Presented here is an implementation of the SMC ABC algorithm to infer model parameters based on SNe Ia from SDSS. To fully deploy this method will require an incorporation of all SN Ia data sets and modeling relative systematics between the surveys. ABC also allows for easy incorporation of priors on model parameters from e.g. CMB or BAO constraints.

One key future implementation of ABC will be for photometric-based surveys when there simply is not enough follow-up time to spectroscopically confirm all SNe Ia. One would explore and model more fully the non-Gaussianity of photometric redshifts as derived from calibration samples. ABC easily incorporates such uncertainties when generating the

model.

A more immediate goal would be to apply the summary statistic comparison at the individual light curve level rather than in Hubble diagram space. Fitting the simulated light curves currently requires most (∼90%) of the computing time but is a necessary step to creating a Hubble diagram. Directly comparing the simulated and observed data could significantly reduce computing time. It would also be a cleaner implementation of the ABC method. The only "training" would be in the generation of the templates that the SNe Ia are derived from in the first place.

SweetSpot We have presented 13 light curves for SNe Ia observed during the pilot program of an approved NOAO Survey to image nearby SNe Ia in the NIR using the WHIRC camera at the WIYN 3.5m Observatory at Kitt Peak. Within this set we have contributed 12 new standard SNe Ia out to $z \sim 0.09$ to the current NIR sample.

We measure a dispersion in peak luminosity for our sample to be 0.164 mag when excluding the over-luminous, 91T-like SN 2011hr. This is impressive considering that our light curves are sparsely sampled and observed at late times as a result of classical scheduling of telescope time and loss of time due to inclement weather. With the completion of the SweetSpot survey, we expect the dispersion to decrease with more comprehensive temporal sampling. The dispersion will also improve as the optical counterparts of these SNe Ia become available and the times of maximum can be more accurately determined.

We are continuing to build off of the presented pilot program with the goal of observing $\sim$ 150 spectroscopically confirmed nearby SNe Ia in the NIR as part of a 3-year 72-night large-scale NOAO Survey. This will increase the currently published sample in this "sweet spot" redshift range by a factor of five. If SNe Ia are standard in the H-band with a dispersion of 0.1 mag then 150 SNe Ia in the nearby Hubble flow will allow us to make an overall relative distance measurement to $z \sim 0.05$ to 1%. Alternatively, we will be able to probe systematics at the few percent level, avoiding significant confusion from host galaxy dust extinction and peculiar velocities.

As we enter the next era of precision cosmology, it becomes increasingly important and beneficial to pursue statistical methods like those outlined in this work.

APPENDIX A

CHAPTER 1 APPENDICES

A.1 BIAS ON WLS COEFFICIENTS

To determine the bias on the estimated coefficients, $\widehat{\beta}_J$, recall that we can model any velocity field with an infinite set of spherical harmonics

$$U = Y\beta + \epsilon \tag{A.1}$$

where β is the column vector given by $\beta = (\beta_0 ... \beta_\infty)$ and

$$Y = \begin{bmatrix} \phi_0(x_1) & \phi_1(x_1) & \cdots & \phi_\infty(x_1) \\ \phi_0(x_2) & \phi_1(x_2) & \cdots & \phi_\infty(x_2) \\ \vdots & \vdots & \cdots & \cdots \\ \phi_0(x_N) & \phi_1(x_N) & \cdots & \phi_\infty(x_N) \end{bmatrix} \tag{A.2}$$

If we substitute U into Equation 2.14 we get

$$\widehat{\beta}_J = (Y_J^T W Y_J)^{-1} Y_J^T W (Y\beta + \epsilon) \tag{A.3}$$

If we decompose $Y\beta$ into

$$Y\beta = Y_J\beta_J + Y_\infty\beta_\infty \tag{A.4}$$

where $\beta_\infty = (\beta_{J+1}...\beta_\infty)^T$ and

$$Y_\infty = \begin{bmatrix} \phi_{J+1}(x_1) & \phi_{J+2}(x_1) & \cdots & \phi_\infty(x_1) \\ \phi_{J+1}(x_2) & \phi_{J+2}(x_2) & \cdots & \phi_\infty(x_2) \\ \vdots & \vdots & \cdots & \cdots \\ \phi_{J+1}(x_N) & \phi_{J+2}(x_N) & \cdots & \phi_\infty(x_N) \end{bmatrix} \tag{A.5}$$

then

$$\begin{aligned} \widehat{\beta}_J &= (Y_J^T W Y_J)^{-1} Y_J^T W (Y_J \beta_J + Y_\infty \beta_\infty + \epsilon) && \text{(A.6)} \\ &= \beta_J + (Y_J^T W Y_J^T)^{-1} Y_J^T W (Y_\infty \beta_\infty + \epsilon) && \text{(A.7)} \end{aligned}$$

The bias on $\widehat{\beta}_J$ is

$$\begin{aligned} \beta_J - \left\langle \widehat{\beta}_J \right\rangle &= \beta_J - \left\langle \beta_J + (Y_J^T W Y_J)^{-1} Y_J^T W (Y_\infty \beta_\infty + \epsilon) \right\rangle && \text{(A.8)} \\ &= \left\langle (Y^T W Y)^{-1} Y^T W (Y_\infty \beta_\infty) \right\rangle . && \text{(A.9)} \end{aligned}$$

A.2 BIAS ON CU COEFFICIENTS

To determine the bias for the weighted coefficients $\widehat{\beta}^*$ we first multiply the top and bottom of Equation 2.21 by $1/N$

$$\begin{aligned} \widehat{\beta}_j^* &= \frac{\frac{1}{N} \sum_{n=1}^{N} \frac{U_n \phi_j(x_n)}{h(x_n)\sigma_n^2}}{\frac{1}{N} \sum_{n=1}^{N} \frac{1}{\sigma_n^2}} && \text{(A.10)} \\ &= \frac{\left\langle \frac{U_n \phi_j(x_n)}{h(x_n)\sigma_n^2} \right\rangle}{\left\langle \frac{1}{\sigma_n^2} \right\rangle} && \text{(A.11)} \end{aligned}$$

If $U(x_n)$, $\phi_j(x_n)$, and $h(x_n)$ are all independent of σ_n, then

$$\left\langle \widehat{\beta}_j^* \right\rangle = \frac{\left\langle \frac{U_n \phi_j(x_n)}{h(x_n)\sigma_n^2} \right\rangle}{\left\langle \frac{1}{\sigma_n^2} \right\rangle} \tag{A.12}$$

$$= \frac{\left\langle \frac{U_n \phi_j(x_n)}{h(x_n)} \right\rangle \left\langle \frac{1}{\sigma_n^2} \right\rangle}{\left\langle \frac{1}{\sigma_n^2} \right\rangle} \tag{A.13}$$

$$= \left\langle \frac{U(x_n)\phi_j(x_n)}{h(x_n)} \right\rangle \tag{A.14}$$

$$= \beta_j \tag{A.15}$$

So our bias is $\beta - \langle \beta_j^* \rangle = 0$.

A.3 RISK ESTIMATION

The risk is a way of determining how many basis functions should be in $f(x)$ and can be written as

$$R = \left\langle (\widehat{\theta} - \theta)^2 \right\rangle \tag{A.16}$$

where $\widehat{\theta}$ is the estimated or measured value of some true parameter, θ. The expectation value of $\widehat{\theta}$ is the mean, $\bar{\theta}$

$$\bar{\theta} \equiv \langle \widehat{\theta} \rangle \tag{A.17}$$

By adding and subtracting the mean from $(\widehat{\theta} - \theta)$ in Equation A.16, the risk can be written in terms of the variance and the bias.

$$R = \left\langle (\widehat{\theta} - \bar{\theta} + \bar{\theta} - \theta)^2 \right\rangle \tag{A.18}$$

$$= \left\langle (\widehat{\theta} - \bar{\theta})^2 \right\rangle + (\bar{\theta} - \theta)^2 + (\bar{\theta} - \theta) \left\langle (\widehat{\theta} - \bar{\theta}) \right\rangle \tag{A.19}$$

$$= \left\langle (\widehat{\theta} - \bar{\theta})^2 \right\rangle + (\bar{\theta} - \theta)^2 \tag{A.20}$$

$$= \mathrm{Var}(\widehat{\theta}) + \mathrm{bias}^2 \tag{A.21}$$

A.4 SMOOTHING MATRIX FOR CU REGRESSION

$$\widehat{f}(x_i) = \sum_{j=0}^{J} \widehat{\beta}_j^* \phi_j(x_i) \tag{A.22}$$

$$= \sum_{j=0}^{J} \phi_j(x_i) \frac{\sum_{n=1}^{N} \frac{U_n \phi_j(x_n)}{h(x_n)\sigma_n^2}}{\sum_{n=1}^{N} \frac{1}{\sigma_n^2}} \tag{A.23}$$

$$= \sum_{n=1}^{N} U_n \frac{\sum_{j=0}^{J} \frac{\phi_j(x_i)\phi_j(x_n)}{h(x_n)\sigma_n^2}}{\sum_{n=1}^{N} \frac{1}{\sigma_n^2}} \tag{A.24}$$

$$= LU \tag{A.25}$$

APPENDIX B

NON-PARAMETRICALLY SMOOTHING THE SIMULATED AND OBSERVED DATA

To perform a non-parametric smooth we use a robust locally weighted regression (Cleveland, 1979). This routine smooths the data by iteratively fitting a local d-order polynomial to the data using a tricube weighting function. We use a quadratic polynomial and, for the observed data, add an additional weight according to the uncertainty in μ given by Equation 3.21.

We choose the size of the window to locally smooth over by minimizing the risk or the sum of the variance and bias squared. We estimate the risk using the leave-one-out cross validation score

$$R(h) = \frac{1}{N}\sum_{i=0}^{I}(f(x_i) - f_{(-x_i)}(x_i))^2 \tag{B.1}$$

where $f(x)$ is the smoothed function using a smoothing window given by h and $f_{(-x_i)}$ is the smooth obtained leaving out the ith data point (see, e.g., Wasserman (2006b)). The smoothing window goes from zero to one with zero being no smooth and one resulting in a line. Using the SDSS data we find the minimum risk to yield a smoothing window of 0.52. As estimating the risk is somewhat computationally intensive, we determine the smoothing window using the observed data and use the same window to smooth the simulated data in the ABC algorithm.

APPENDIX C

BIBLIOGRAPHY

Abate, A., Bridle, S., Teodoro, L. F. A., Warren, M. S., & Hendry, M. 2008, MNRAS, 389, 1739

Abate, A., & Erdoğdu, P. 2009, MNRAS, 400, 1541

Abazajian, K., Adelman-McCarthy, J. K., Agüeros, M. A., et al. 2003, AJ, 126, 2081

—. 2005, AJ, 129, 1755

Albrecht, A., Bernstein, G., Cahn, R., et al. 2006a, ArXiv Astrophysics e-prints, arXiv:astro-ph/0609591

—. 2006b, ArXiv Astrophysics e-prints, arXiv:astro-ph/0609591, arXiv:astro-ph/0609591

Aldering, G., Adam, G., Antilogus, P., et al. 2002, in SPIE Conference Series, Vol. 4836, SPIE Proc., ed. J. A. Tyson & S. Wolff, 61–72

Amanullah, R., Lidman, C., Rubin, D., et al. 2010, ApJ, 716, 712

Astier, P., Guy, J., Regnault, N., et al. 2006, A&A, 447, 31

Badenes, C., Hughes, J. P., Bravo, E., & Langer, N. 2007, ApJ, 662, 472

Badenes, C., Hughes, J. P., Cassam-Chenaï, G., & Bravo, E. 2008, ApJ, 680, 1149

Balam, D. D., Graham, M. L., Hsiao, E. Y., & Green, D. W. E. 2011, Central Bureau Electronic Telegrams, 2825, 2

Balanutsa, P., & Lipunov, V. 2011, Central Bureau Electronic Telegrams, 2931, 1

Baltay, C., Rabinowitz, D., Hadjiyska, E., et al. 2012, The Messenger, 150, 34

Barlow, R. 2003, ArXiv Physics e-prints, arXiv:physics/0306138

Barnes, C., Filippi, S., Stumpf, M. P. H., & Thorne, T. 2011, ArXiv e-prints, arXiv:1106.6281

Barone-Nugent, R. L., Lidman, C., Wyithe, J. S. B., et al. 2012, MNRAS, 425, 1007

Beaumont, M. A., Cornuet, J.-M., Marin, J.-M., & Robert, C. P. 2009, Biometrika, 96, 983

Beaumont, M. A., Zhang, W., & Balding, D. J. 2002, Genetics, 162, 2025

Benz, W., Thielemann, F.-K., & Hills, J. G. 1989, ApJ, 342, 986

Bernardi, M., Alonso, M. V., da Costa, L. N., et al. 2002, AJ, 123, 2990

Blakeslee, J. P., Davis, M., Tonry, J. L., Dressler, A., & Ajhar, E. A. 1999, ApJ, 527, L73

Blondin, S., Kasen, D., Röpke, F. K., Kirshner, R. P., & Mandel, K. S. 2011, MNRAS, 417, 1280

Blondin, S., & Tonry, J. L. 2007, ApJ, 666, 1024

Bloom, J. S., Starr, D. L., Blake, C. H., Skrutskie, M. F., & Falco, E. E. 2006, in Astronomical Society of the Pacific Conference Series, Vol. 351, Astronomical Data Analysis Software and Systems XV, ed. C. Gabriel, C. Arviset, D. Ponz, & S. Enrique, 751

Blum, M. G. B., & Francois, O. 2008, ArXiv e-prints, arXiv:0809.4178

Blum, M. G. B., Nunes, M. A., Prangle, D., & Sisson, S. A. 2012, ArXiv e-prints, 1202.3819, arXiv:1202.3819

Borgani, S., da Costa, L. N., Zehavi, I., et al. 2000, AJ, 119, 102

Bottinelli, L., Durand, N., Fouque, P., et al. 1993, A&AS, 102, 57

Bours, M. C. P., Toonen, S., & Nelemans, G. 2013, A&A, 552, A24

Branchini, E., Teodoro, L., Frenk, C. S., et al. 1999, MNRAS, 308, 1

Branchini, E., Freudling, W., Da Costa, L. N., et al. 2001, MNRAS, 326, 1191

Burns, C. R., Stritzinger, M., Phillips, M. M., et al. 2011, AJ, 141, 19

Cameron, E., & Pettitt, A. N. 2012, ArXiv e-prints, arXiv:1202.1426

Canal, R., Méndez, J., & Ruiz-Lapuente, P. 2001, ApJ, 550, L53

Cardelli, J. A., Clayton, G. C., & Mathis, J. S. 1989, ApJ, 345, 245

Casali, M., Pirard, J.-F., Kissler-Patig, M., et al. 2006, in SPIE Conference Series, Vol. 6269, SPIE Proc.

Childress, M., Aldering, G., Antilogus, P., et al. 2013, ApJ, 770, 108

Chomiuk, L. 2013, PASA, 30, 46

Chotard, N., Gangler, E., Aldering, G., et al. 2011, A&A, 529, L4+

Cleveland, W. S. 1979, Journal of the American Statistical Association, 74, 829

Colin, J., Mohayaee, R., Sarkar, S., & Shafieloo, A. 2010, ArXiv e-prints, arXiv:1011.6292

Colless, M., Saglia, R. P., Burstein, D., et al. 2001, MNRAS, 321, 277

Conley, A., Carlberg, R. G., Guy, J., et al. 2007, ApJ, 664, L13

Conley, A., & Sullivan, M. 2011, SiFTO: An Empirical Method for Fitting SN Ia Light Curves, astrophysics Source Code Library, ascl:1110.023

Conley, A., Guy, J., Sullivan, M., et al. 2011, ApJS, 192, 1

Contreras, C., Hamuy, M., Phillips, M. M., et al. 2010, AJ, 139, 519

Cooray, A., & Caldwell, R. R. 2006, Phys. Rev. D, 73, 103002

Courteau, S., Willick, J. A., Strauss, M. A., Schlegel, D., & Postman, M. 2000, ApJ, 544, 636

Cowles, M. K., & Carlin, B. P. 1996, Journal of the American Statistical Association, 91, pp. 883

Cox, L., Newton, J., Puckett, T., et al. 2011, Central Bureau Electronic Telegrams, 2939, 1

da Costa, L. N., Bernardi, M., Alonso, M. V., et al. 2000a, ApJ, 537, L81

—. 2000b, AJ, 120, 95

da Costa, L. N., Freudling, W., Wegner, G., et al. 1996, ApJ, 468, L5+

da Costa, L. N., Nusser, A., Freudling, W., et al. 1998, MNRAS, 299, 425

Dale, D. A., Giovanelli, R., Haynes, M. P., Campusano, L. E., & Hardy, E. 1999a, AJ, 118, 1489

Dale, D. A., Giovanelli, R., Haynes, M. P., et al. 1999b, ApJ, 510, L11

Dale, D. A., Giovanelli, R., Haynes, M. P., Hardy, E., & Campusano, L. E. 1999c, AJ, 118, 1468

Davis, M., Nusser, A., Masters, K., et al. 2010a, ArXiv e-prints, arXiv:1011.3114

Davis, M., Nusser, A., & Willick, J. A. 1996, ApJ, 473, 22

Davis, T. M., Hui, L., Frieman, J. A., et al. 2010b, ArXiv e-prints, arXiv:1012.2912

de Vaucouleurs, G., de Vaucouleurs, A., Corwin, Jr., H. G., et al. 1991, Third Reference Catalogue of Bright Galaxies. Volume I: Explanations and references. Volume II: Data for galaxies between 0^h and 12^h. Volume III: Data for galaxies between 12^h and 24^h. (Springer, New York, NY (USA))

Dekel, A., Eldar, A., Kolatt, T., et al. 1999, ApJ, 522, 1

della Valle, M., & Livio, M. 1996, ApJ, 473, 240

Dennefeld, M., & Ricquebourg, F. 2005, IAU Circ., 8541, 4

Dewdney, P. E., Hall, P. J., Schilizzi, R. T., & Lazio, T. J. L. W. 2009, IEEE Proceedings, 97, 1482

Dilday, B., Kessler, R., Frieman, J. A., et al. 2008, ApJ, 682, 262

Djorgovski, S., & Davis, M. 1987, ApJ, 313, 59

Drake, A. J., Djorgovski, S. G., Mahabal, A., et al. 2009, ApJ, 696, 870

—. 2011, Central Bureau Electronic Telegrams, 2838, 1

Dressler, A., Faber, S. M., Burstein, D., et al. 1987a, ApJ, 313, L37

Dressler, A., Lynden-Bell, D., Burstein, D., et al. 1987b, ApJ, 313, 42

Efromovich, S. 1999, Nonparametric Curve Estimation (175 Fifth Avenue, New York, NY 10010,USA: Springer-Verlag New York, Inc.)

Eisenstein, D. J., Zehavi, I., Hogg, D. W., et al. 2005, ApJ, 633, 560

Elias-Rosa, N., Benetti, S., Turatto, M., et al. 2008, MNRAS, 384, 107

Falco, E. E., Kurtz, M. J., Geller, M. J., et al. 1999, PASP, 111, 438

Fearnhead, P., & Prangle, D. 2012, Journal Of The Royal Statistical Society Series B, 74

Feldman, H. A., & Watkins, R. 2008, MNRAS, 387, 825

Feldman, H. A., Watkins, R., & Hudson, M. J. 2010, MNRAS, 1092

Filippenko, A. V. 1997, ARA&A, 35, 309

Filippenko, A. V., Li, W. D., Treffers, R. R., & Modjaz, M. 2001, in Astronomical Society of the Pacific Conference Series, Vol. 246, IAU Colloq. 183: Small Telescope Astronomy on Global Scales, ed. B. Paczynski, W.-P. Chen, & C. Lemme, 121

Filippi, S., Barnes, C., & Stumpf, M. P. H. 2011, ArXiv e-prints, arXiv:1106.6280

Fisher, K. B., Huchra, J. P., Strauss, M. A., et al. 1995, ApJS, 100, 69

Fixsen, D. J., Cheng, E. S., Gales, J. M., et al. 1996, ApJ, 473, 576

Folatelli, G., Phillips, M. M., Burns, C. R., et al. 2010, AJ, 139, 120

Foley, R. J., & Kasen, D. 2011, ApJ, 729, 55

Foley, R. J., Narayan, G., Challis, P. J., et al. 2010, ApJ, 708, 1748

Fraser, M., Magill, L., Smartt, S., & Kotak, R. 2011, Central Bureau Electronic Telegrams, 2931, 2

Freudling, W., Zehavi, I., da Costa, L. N., et al. 1999, ApJ, 523, 1

Frieman, J. A., Bassett, B., Becker, A., et al. 2008, AJ, 135, 338

Fu, Y. X., & Li, W. H. 1997, Molecular Biology and Evolution, 14, 195

Fuhrmann, K. 2005, MNRAS, 359, L35

Gal-Yam, A., Yaron, O., Ben-Ami, S., et al. 2011a, The Astronomer's Telegram, 3798, 1

Gal-Yam, A., Ben-Ami, S., Yaron, O., et al. 2011b, The Astronomer's Telegram, 3739, 1

Ganeshalingam, M., Li, W., Filippenko, A. V., et al. 2010, ApJS, 190, 418

Geier, S., Heber, U., Kupfer, T., & Napiwotzki, R. 2010, A&A, 515, A37

Giovanelli, R., Haynes, M. P., Herter, T., et al. 1997a, AJ, 113, 53

—. 1997b, AJ, 113, 22

Giovanelli, R., Haynes, M. P., Salzer, J. J., et al. 1994, AJ, 107, 2036

—. 1995, AJ, 110, 1059

—. 1998, AJ, 116, 2632

Goobar, A. 2008, ApJ, 686, L103

Gordon, C., Land, K., & Slosar, A. 2007, Physical Review Letters, 99, 081301

—. 2008, MNRAS, 387, 371

Graur, O., & Maoz, D. 2012a, The Astronomer's Telegram, 4226, 1

—. 2012b, The Astronomer's Telegram, 4535, 1

Gupta, R. R., D'Andrea, C. B., Sako, M., et al. 2011, ApJ, 740, 92

Guy, J., Astier, P., Baumont, S., et al. 2007, A&A, 466, 11

Guy, J., Sullivan, M., Conley, A., et al. 2010, A&A, 523, A7

Hachisu, I., Kato, M., & Nomoto, K. 1996, ApJ, 470, L97

Hamuy, M., Phillips, M. M., Suntzeff, N. B., et al. 1996, AJ, 112, 2391

Hamuy, M., Folatelli, G., Morrell, N. I., et al. 2006, PASP, 118, 2

Han, Z., & Podsiadlowski, P. 2004, MNRAS, 350, 1301

Hannestad, S., Haugbølle, T., & Thomsen, B. 2008, J. Cosmology Astropart. Phys., 2, 22

Hastie, T., Tibshirani, R., & Friedman, J. 2009, The Elements of Statistical Learning (New York, NY: Springer)

Haugbølle, T., Hannestad, S., Thomsen, B., et al. 2007, ApJ, 661, 650

Haynes, M. P., Giovanelli, R., Chamaraux, P., et al. 1999a, AJ, 117, 2039

Haynes, M. P., Giovanelli, R., Salzer, J. J., et al. 1999b, AJ, 117, 1668

Hernandez, M., Meikle, W. P. S., Aparicio, A., et al. 2000, MNRAS, 319, 223

Hicken, M., Wood-Vasey, W. M., Blondin, S., et al. 2009a, ApJ, 700, 1097

Hicken, M., Challis, P., Jha, S., et al. 2009b, ApJ, 700, 331

Hicken, M., Challis, P., Kirshner, R. P., et al. 2012, ApJS, 200, 12

Hodapp, K.-W., Hora, J., Graves, E., et al. 2000, in SPIE Conference Series, Vol. 4008, SPIE Proc., ed. Iye, M. and Moorwood, A. F., 1334–1341

Hoffman, Y., Eldar, A., Zaroubi, S., & Dekel, A. 2001, ArXiv Astrophysics e-prints, arXiv:astro-ph/0102190

Hoffman, Y., & Zaroubi, S. 2000, ApJ, 535, L5

Holtzman, J. A., Marriner, J., Kessler, R., et al. 2008, AJ, 136, 2306

Howell, D. A. 2011, Nature Communications, 2, arXiv:1011.0441

Howerton, S., Drake, A. J., Djorgovski, S. G., et al. 2011, Central Bureau Electronic Telegrams, 2881, 1

Hsiao, E. Y., Conley, A., Howell, D. A., et al. 2007, ApJ, 663, 1187

Hudson, M. J. 2003, ArXiv Astrophysics e-prints, arXiv:astro-ph/0311072

Hudson, M. J., Lucey, J. R., Smith, R. J., Schlegel, D. J., & Davies, R. L. 2001, MNRAS, 327, 265

Hudson, M. J., Smith, R. J., Lucey, J. R., & Branchini, E. 2004, MNRAS, 352, 61

Hudson, M. J., Smith, R. J., Lucey, J. R., Schlegel, D. J., & Davies, R. L. 1999, ApJ, 512, L79

Hui, L., & Greene, P. B. 2006, Phys. Rev. D, 73, 123526

Iben, Jr., I., & Tutukov, A. V. 1984, ApJS, 54, 335

Ihara, Y., Ozaki, J., Doi, M., et al. 2007, PASJ, 59, 811

Jha, S., Riess, A. G., & Kirshner, R. P. 2007a, ApJ, 659, 122

—. 2007b, ApJ, 659, 122

Jha, S., Garnavich, P. M., Kirshner, R. P., et al. 1999, ApJS, 125, 73

Jin, Z., & Gao, X. 2011, Central Bureau Electronic Telegrams, 2871, 1

Jin, Z., Gao, X., Brimacombe, J., Noguchi, T., & Nakano, S. 2011, Central Bureau Electronic Telegrams, 2825, 1

Jones, D. H., Read, M. A., Saunders, W., et al. 2009, MNRAS, 399, 683

Joyce, D. 2009, WIYN High-Resolution Infrared Camera (WHIRC) Quick Guide to Data Reduction Version 1.03, Tech. rep., National Optical Astronomy Observatory

Karachentsev, I. D., & Makarov, D. A. 1996, AJ, 111, 794

Kasen, D. 2006, ApJ, 649, 939

—. 2010, ApJ, 708, 1025

Kasen, D., Röpke, F. K., & Woosley, S. E. 2009, Nature, 460, 869

Kashlinsky, A., Atrio-Barandela, F., Kocevski, D., & Ebeling, H. 2008, ApJ, 686, L49

Kato, M., & Hachisu, I. 2012, Bulletin of the Astronomical Society of India, 40, 393

Kattner, S., Leonard, D. C., Burns, C. R., et al. 2012, PASP, 124, 114

Kelly, P. L., Hicken, M., Burke, D. L., Mandel, K. S., & Kirshner, R. P. 2010, ApJ, 715, 743

Kerzendorf, W. E., Schmidt, B. P., Asplund, M., et al. 2009, ApJ, 701, 1665

Kessler, R., Becker, A. C., Cinabro, D., et al. 2009a, ApJS, 185, 32

—. 2009b, ApJS, 185, 32

Kessler, R., Bernstein, J. P., Cinabro, D., et al. 2009c, PASP, 121, 1028

Kirshner, R. P., et al. 2012, HST Proposal

Knop, R. A., Aldering, G., Amanullah, R., et al. 2003, ApJ, 598, 102

Komatsu, E., Dunkley, J., Nolta, M. R., et al. 2009, ApJS, 180, 330

Kosenko, D., Blinnikov, S. I., & Vink, J. 2011, A&A, 532, A114

Kowalski, M., Rubin, D., Aldering, G., et al. 2008, ApJ, 686, 749

Krisciunas, K., Hastings, N. C., Loomis, K., et al. 2000, ApJ, 539, 658

Krisciunas, K., Phillips, M. M., & Suntzeff, N. B. 2004a, ApJ, 602, L81

—. 2004b, ApJ, 602, L81

Krisciunas, K., Phillips, M. M., Suntzeff, N. B., et al. 2004c, AJ, 127, 1664

Krisciunas, K., Garnavich, P. M., Stanishev, V., et al. 2007, AJ, 133, 58

Kudrya, Y. N., Karachentseva, V. E., Karachentsev, I. D., Mitronova, S. N., & Huchtmeier, W. K. 2009, Astrophysics, 52, 335

Kudrya, Y. N., Karachentseva, V. E., Karachentsev, I. D., et al. 2003, A&A, 407, 889

Lampeitl, H., Smith, M., Nichol, R. C., et al. 2010, ApJ, 722, 566

Lavaux, G., Tully, R. B., Mohayaee, R., & Colombi, S. 2010, ApJ, 709, 483

Law, N. M., Kulkarni, S. R., Dekany, R. G., et al. 2009, PASP, 121, 1395

Leaman, J., Li, W., Chornock, R., & Filippenko, A. V. 2010, ArXiv e-prints, arXiv:1006.4611

Li, W., Chornock, R., Leaman, J., et al. 2011a, MNRAS, 412, 1473

Li, W., Bloom, J. S., Podsiadlowski, P., et al. 2011b, Nature, 480, 348

Li, X.-D., & van den Heuvel, E. P. J. 1997, A&A, 322, L9

Lipunov, V., & Balanutsa, P. 2011, Central Bureau Electronic Telegrams, 2873, 1

Lira, P. 1996, Master's thesis, MS thesis. Univ. Chile (1996)

Lorén-Aguilar, P., Isern, J., & García-Berro, E. 2009, A&A, 500, 1193

LSST Science Collaborations, Abell, P. A., Allison, J., et al. 2009, ArXiv e-prints, 0912.0201, arXiv:0912.0201

Ma, Y., Gordon, C., & Feldman, H. A. 2010, ArXiv e-prints, arXiv:1010.4276

Macaulay, E., Feldman, H. A., Ferreira, P. G., Hudson, M. J., & Watkins, R. 2010, ArXiv e-prints, arXiv:1010.2651

Madore, B. F., & Freedman, W. L. 1995, AJ, 109, 1645

Maguire, K., Sullivan, M., Ellis, R. S., et al. 2012, MNRAS, 426, 2359

Maguire, K., Sullivan, M., Patat, F., et al. 2013, MNRAS, 436, 222

Mandel, K. S., Narayan, G., & Kirshner, R. P. 2011, ApJ, 731, 120

Mandel, K. S., Wood-Vasey, W. M., Friedman, A. S., & Kirshner, R. P. 2009, ApJ, 704, 629

Maoz, D., & Mannucci, F. 2008, MNRAS, 388, 421

—. 2012, PASA, 29, 447

Maoz, D., Mannucci, F., & Nelemans, G. 2013, ArXiv e-prints, arXiv:1312.0628

Marietta, E., Burrows, A., & Fryxell, B. 2000, ApJS, 128, 615

Marin, J.-M., Pudlo, P., Robert, C. P., & Ryder, R. 2011, ArXiv e-prints, arXiv:1101.0955

Marion, G. H. 2011, Central Bureau Electronic Telegrams, 2838, 3

Marion, G. H., & Berlind, P. 2011a, Central Bureau Electronic Telegrams, 2880, 2

—. 2011b, Central Bureau Electronic Telegrams, 2892, 3

—. 2011c, Central Bureau Electronic Telegrams, 2939, 2

Marjoram, P., Molitor, J., Plagnol, V., & Tavaré, S. 2003, Proceedings of the National Academy of Science, 1001, 15324

Masters, K. L., Springob, C. M., Haynes, M. P., & Giovanelli, R. 2006, ApJ, 653, 861

Masters, K. L., Springob, C. M., & Huchra, J. P. 2008, AJ, 135, 1738

Matheson, T., Joyce, R. R., Allen, L. E., et al. 2012, ApJ, 754, 19

Mattila, S., Lundqvist, P., Sollerman, J., et al. 2005, A&A, 443, 649

Mazzali, P. A., Röpke, F. K., Benetti, S., & Hillebrandt, W. 2007, Science, 315, 825

Meikle, W. P. S. 2000, MNRAS, 314, 782

Meixner, M., Smee, S., Doering, R. L., et al. 2010, PASP, 122, 451

Miknaitis, G., Pignata, G., Rest, A., et al. 2007, ApJ, 666, 674

Moll, R., Raskin, C., Kasen, D., & Woosley, S. 2013, ArXiv e-prints, arXiv:1311.5008

Moral, P. D., Doucet, A., & Jasra, A. 2006, Journal Of The Royal Statistical Society Series B, 68, 411

Mould, J. R., Huchra, J. P., Freedman, W. L., et al. 2000, ApJ, 529, 786

Murphy, S., Keller, S., Schmidt, B., et al. 2009, in Astronomical Society of the Pacific Conference Series, Vol. 404, Astronomical Society of the Pacific Conference Series, ed. S. J. Murphy & M. S. Bessell, 356–+

Nakano, S. 2011, Central Bureau Electronic Telegrams, 2892, 1

Nayak, I., Cenko, S. B., Li, W., et al. 2011, Central Bureau Electronic Telegrams, 2901, 1

Neill, J. D., Hudson, M. J., & Conley, A. 2007, ApJ, 661, L123

Nelemans, G., Voss, R., Roelofs, G., & Bassa, C. 2008, MNRAS, 388, 487

Nelemans, G., Napiwotzki, R., Karl, C., et al. 2005, A&A, 440, 1087

Nishiura, S., Shimada, M., Ohyama, Y., Murayama, T., & Taniguchi, Y. 2000, AJ, 120, 1691

Nomoto, K. 1982, ApJ, 253, 798

Nugent, P. E., Sullivan, M., Cenko, S. B., et al. 2011, Nature, 480, 344

Nusser, A., da Costa, L. N., Branchini, E., et al. 2001, MNRAS, 320, L21

Nusser, A., & Davis, M. 1994, ApJ, 421, L1

—. 1995, MNRAS, 276, 1391

—. 2011, ArXiv e-prints, arXiv:1101.1650

Ochner, P., Valenti, S., Benetti, S., et al. 2011, Central Bureau Electronic Telegrams, 2873, 2

Osip, D. J., Phillips, M. M., Bernstein, R., et al. 2004, in Proceedings of the SPIE, Vol. 5492, Society of Photo-Optical Instrumentation Engineers (SPIE) Conference Series, ed. A. F. M. Moorwood & M. Iye, 49–59

Pan, K.-C., Ricker, P. M., & Taam, R. E. 2013, ApJ, 773, 49

Park, C. 2000, MNRAS, 319, 573

Park, C., & Park, C. 2006, ApJ, 637, 1

Pastorello, A., Mazzali, P. A., Pignata, G., et al. 2007a, MNRAS, 377, 1531

Pastorello, A., Taubenberger, S., Elias-Rosa, N., et al. 2007b, MNRAS, 376, 1301

Patnaude, D. J., Badenes, C., Park, S., & Laming, J. M. 2012, ApJ, 756, 6

Patterson, J., Oksanen, A., Monard, B., et al. 2013, ArXiv e-prints, arXiv:1303.0736

Peebles, P. 1993, Principles of Physical Cosmology (41 William Street, Princeton, New Jersey 08540, USA: Princeton University Press)

Perlmutter, S., Aldering, G., Goldhaber, G., et al. 1999, ApJ, 517, 565

Phillips, M. M. 1993, ApJ, 413, L105

—. 2012, PASA, 29, 434

Phillips, M. M., Lira, P., Suntzeff, N. B., et al. 1999, AJ, 118, 1766

Phillips, M. M., Krisciunas, K., Suntzeff, N. B., et al. 2006, AJ, 131, 2615

Pike, R. W., & Hudson, M. J. 2005, ApJ, 635, 11

Pritchard, J. K., Seielstad, M. T., Perez-Lezaun, A., & Feldman, M. W. 1999, Molecular Biology and Evolution, 16, 1791

Radburn-Smith, D. J., Lucey, J. R., & Hudson, M. J. 2004a, MNRAS, 355, 1378

—. 2004b, MNRAS, 355, 1378

Raskin, C., Timmes, F. X., Scannapieco, E., Diehl, S., & Fryer, C. 2009, MNRAS, 399, L156

Rauzy, S., & Hendry, M. A. 2000, MNRAS, 316, 621

Rest, A., Welch, D. L., Suntzeff, N. B., et al. 2008, ApJ, 681, L81

Richmond, M. W., & Smith, H. A. 2012, Journal of the American Association of Variable Star Observers (JAAVSO), 40, 872

Riess, A. G., Press, W. H., & Kirshner, R. P. 1995, ApJ, 445, L91

—. 1996, ApJ, 473, 88

Riess, A. G., Filippenko, A. V., Challis, P., et al. 1998, AJ, 116, 1009

Riess, A. G., Kirshner, R. P., Schmidt, B. P., et al. 1999, AJ, 117, 707

Riess, A. G., Strolger, L.-G., Tonry, J., et al. 2004, ApJ, 607, 665

Riess, A. G., Strolger, L.-G., Casertano, S., et al. 2007, ApJ, 659, 98

Riess, A. G., Macri, L., Li, W., et al. 2009, ApJS, 183, 109

Rigault, M., Copin, Y., Aldering, G., et al. 2013, ArXiv e-prints, 1309.1182, arXiv:1309.1182

Röpke, F. K., Kromer, M., Seitenzahl, I. R., et al. 2012, ApJ, 750, L19

Rosswog, S., Kasen, D., Guillochon, J., & Ramirez-Ruiz, E. 2009, ApJ, 705, L128

Ruiz-Lapuente, P., Comeron, F., Méndez, J., et al. 2004, Nature, 431, 1069

Sako, M., Bassett, B., Becker, A., et al. 2008, AJ, 135, 348

Sako, M., Bassett, B., Becker, A. C., et al. 2014, ArXiv e-prints, arXiv:1401.3317

Sarkar, D., Feldman, H. A., & Watkins, R. 2007, MNRAS, 375, 691

Schaefer, B. E. 2010, ApJS, 187, 275

Schaefer, B. E., & Pagnotta, A. 2012, Nature, 481, 164

Schlegel, D. J., Finkbeiner, D. P., & Davis, M. 1998, ApJ, 500, 525

Scolnic, D. M., Riess, A. G., Foley, R. J., et al. 2013, ArXiv e-prints, 1306.4050, arXiv:1306.4050

Shappee, B. J., Kochanek, C. S., & Stanek, K. Z. 2013, ApJ, 765, 150

Sisson, S. A., Fan, Y., & Tanaka, M. M. 2007, Proceedings of the National Academy of Science, 104, 1760

Skrutskie, M. F., Cutri, R. M., Stiening, R., et al. 2006, AJ, 131, 1163

Smith, R. J., Lucey, J. R., Hudson, M. J., Schlegel, D. J., & Davies, R. L. 2000, MNRAS, 313, 469

Smith, R. J., Lucey, J. R., Schlegel, D. J., et al. 2001, MNRAS, 327, 249

Smith, R. J., Hudson, M. J., Nelan, J. E., et al. 2004, AJ, 128, 1558

Song, Y., Sabiu, C. G., Kayo, I., & Nichol, R. C. 2010, ArXiv e-prints, arXiv:1006.4630

Springob, C. M., Masters, K. L., Haynes, M. P., Giovanelli, R., & Marinoni, C. 2007, ApJS, 172, 599

Stanishev, V., Goobar, A., Benetti, S., et al. 2007, A&A, 469, 645

Starrfield, S., Truran, J. W., Sparks, W. M., & Kutter, G. S. 1972, ApJ, 176, 169

Stritzinger, M. D., Phillips, M. M., Boldt, L. N., et al. 2011, AJ, 142, 156

Sullivan, M., Conley, A., Howell, D. A., et al. 2010, MNRAS, 406, 782

Tavare, S. A., Balding, D. J., Griffiths, R. C., & Donnelly, P. 1997, Genetics, 145, 505

Theureau, G. 1998, A&A, 331, 1

Tonry, J. L., Blakeslee, J. P., Ajhar, E. A., & Dressler, A. 2000, ApJ, 530, 625

Tonry, J. L., Dressler, A., Blakeslee, J. P., et al. 2001, ApJ, 546, 681

Toonen, S., Nelemans, G., & Portegies Zwart, S. 2012, A&A, 546, A70

Tully, R. B., & Fisher, J. R. 1977, A&A, 54, 661

Tutukov, A., & Yungelson, L. 1996, MNRAS, 280, 1035

van den Heuvel, E. P. J., Bhattacharya, D., Nomoto, K., & Rappaport, S. A. 1992, A&A, 262, 97

Wakamatsu, K., Colless, M., Jarrett, T., et al. 2003, in Astronomical Society of the Pacific Conference Series, Vol. 289, The Proceedings of the IAU 8th Asian-Pacific Regional Meeting, Volume I, ed. S. Ikeuchi, J. Hearnshaw, & T. Hanawa, 97–104

Wang, L., & Wheeler, J. C. 2008, ARA&A, 46, 433

Wang, X., Wang, L., Pain, R., Zhou, X., & Li, Z. 2006, ApJ, 645, 488

Wang, X., Filippenko, A. V., Ganeshalingam, M., et al. 2009, ApJ, 699, L139

Wasserman, L. 2006a, All of Nonparametric Statistics (233 Spring Street, New York, NY 10013,USA: Springer Science+Businesse Media, Inc.)

—. 2006b, All of Nonparametric Statistics (233 Spring Street, New York, NY 10013,USA: Springer Science+Businesse Media, Inc.)

Watkins, R., & Feldman, H. A. 2007, MNRAS, 379, 343

Watkins, R., Feldman, H. A., & Hudson, M. J. 2009, MNRAS, 392, 743

Webbink, R. F. 1984, ApJ, 277, 355

Wegner, G., Colless, M., Baggley, G., et al. 1996, ApJS, 106, 1

Weiss, G., & von Haeseler, A. 1998, Genetics, 149, 1539

Whelan, J., & Iben, Jr., I. 1973, ApJ, 186, 1007

Willick, J. A., Courteau, S., Faber, S. M., Burstein, D., & Dekel, A. 1995, ApJ, 446, 12

Willick, J. A., Courteau, S., Faber, S. M., et al. 1996, ApJ, 457, 460

—. 1997, ApJS, 109, 333

Willick, J. A., & Strauss, M. A. 1998, ApJ, 507, 64

Wood-Vasey, W. M., Miknaitis, G., Stubbs, C. W., et al. 2007, ApJ, 666, 694

Wood-Vasey, W. M., Friedman, A. S., Bloom, J. S., et al. 2008a, ApJ, 689, 377

—. 2008b, ApJ, 689, 377

Yaron, O., Prialnik, D., Shara, M. M., & Kovetz, A. 2005, ApJ, 623, 398

Zaroubi, S. 2002, ArXiv Astrophysics e-prints, arXiv:astro-ph/0206052

Zaroubi, S., Bernardi, M., da Costa, L. N., et al. 2001, MNRAS, 326, 375

Zaroubi, S., Hoffman, Y., & Dekel, A. 1999, ApJ, 520, 413

Zaroubi, S., Zehavi, I., Dekel, A., Hoffman, Y., & Kolatt, T. 1997, ApJ, 486, 21

Zehavi, I., Riess, A. G., Kirshner, R. P., & Dekel, A. 1998, ApJ, 503, 483

Zhang, T., Chen, J., Wang, X., Lin, L., & Kong, X. 2011a, Central Bureau Electronic Telegrams, 2871, 4

Zhang, T.-M., Zhang, J.-J., & Wang, X.-F. 2011b, Central Bureau Electronic Telegrams, 2901, 2